CONTROL OF FLOW STRUCTURE ON NON-SLENDER DELTA WING USING BIO INSPIRED EDGE MODIFICATIONS

A THESIS SUBMITTED TO
THE GRADUATE SCHOOL OF NATURAL AND APPLIED SCIENCES
OF
MIDDLE EAST TECHNICAL UNIVERSITY

BY

DİREN DİKBAŞ

IN PARTIAL FULFILLMENT OF THE REQUIREMENTS
FOR
THE DEGREE OF MASTER OF SCIENCE
IN
MECHANICAL ENGINEERING

AUGUST 2025

Approval of the thesis:

CONTROL OF FLOW STRUCTURE ON NON-SLENDER DELTA WING USING BIO INSPIRED EDGE MODIFICATIONS

submitted by **DİREN DİKBAŞ** in partial fulfillment of the requirements for the degree of **Master of Science in Mechanical Engineering, Middle East Technical University** by,

Prof. Dr. Naci Emre Altun
Dean, **Graduate School of Natural and Applied Sciences**

Prof. Dr. Serkan Dağ
Head of the Department, **Mechanical Engineering**

Prof. Dr. Mehmet Metin Yavuz
Supervisor, **Mechanical Engineering, METU**

Dr. Göktuğ Koçak
Co-Supervisor, **Mechanical Engineering, Turkish Aerospace Industries**

Examining Committee Members:

Prof. Dr. Cüneyt Sert
Mechanical Eng., METU

Prof. Dr. Mehmet Metin Yavuz
Mechanical Eng., METU

Assoc. Prof. Dr. Özgür Uğraş Baran
Mechanical Eng., METU.

Prof. Dr. Murat Köksal
Mechanical Eng., Hacettepe Uni.

Assist. Prof. Dr. Onur Baş
Mechanical Eng., TEDU

Date: 27.08.2025

I hereby declare that all information in this document has been obtained and presented in accordance with academic rules and ethical conduct. I also declare that, as required by these rules and conduct, I have fully cited and referenced all material and results that are not original to this work.

Name Last name: Diren Dikbaş

Signature:

ABSTRACT

CONTROL OF FLOW STRUCTURE ON NON-SLENDER DELTA WING USING BIO INSPIRED EDGE MODIFICATIONS

Dikbaş, Diren
Master of Science, Mechanical Engineering
Supervisor: Prof. Dr. Mehmet Metin Yavuz
Co-Supervisor: Dr. Göktuğ Koçak

August 2025, 134 pages

Non-slender delta wings are commonly used in fighter jets, unmanned aerial vehicles, and micro air vehicles due to their low structural weight-to-takeoff-weight ratio and high maneuverability. However, compared to slender delta wings, they typically produce lower maximum lift and tend to stall at lower angles of attack. The implementation of flow control methods can help improve their aerodynamic performance.

In the present study, the effects of the bio-inspired leading-edge modifications on the aerodynamic performance and flow structure of non-slender delta wing models, both in and out of ground effect, were investigated using force, surface pressure, and near-surface PIV measurements. Seven different sharp-edged delta wing models with a 45-degree sweep angle were used to study the effect of sinusoidal and saw-tooth leading-edge modifications. Sinusoidal leading-edge wing designs were inspired by the leading-edge tubercles of the humpback whales, and the saw-tooth wing designs were inspired by the leading-edge serrations of owl feathers.

The results of the aerodynamic coefficients indicate that the bio-inspired wing modifications delay the stall angle, produce smoother stall characteristics, and enhance post-stall lift. Near-surface PIV measurements show that at high angles of attack, large-scale three-dimensional surface separation appears on the planform for the base wing, whereas the modified wings reduce or delay this separation. A distinct flow pattern is observed for the saw-tooth wing at low angles of attack, indicating the footprint of multiple leading-edge vortices. Ground effect measurements show increased maximum lift for all the wings as the ground clearance decreased, while the stall angle remained nearly constant.

Keywords: Non-slender Delta Wing, Passive Flow Control, Experimental Aerodynamics, Ground Effect, Bio-Inspired Wing Modifications

ÖZ

İNCE OLMAYAN DELTA KANATLARDA DOĞADAN ESİNLENİLMİŞ HÜCUM KENARI MODİFİKASYONLARI İLE AKIŞ KONTROLÜ

Dikbaş, Diren
Yüksek Lisans, Makina Mühendisliği
Tez Yöneticisi: Prof. Dr. Mehmet Metin Yavuz
Ortak Tez Yöneticisi: Dr. Göktuğ Koçak

Ağustos 2025, 134 sayfa

Düşük ok açılı, ya da ince olmayan, delta kanatlar, düşük yapısal ağırlık oranı ve yüksek manevra yetkisi nedeniyle genel olarak savaş uçaklarında, insansız hava araçlarında ve mikro hava araçlarında kullanılmaktadır. Ancak, yüksek ok açılı delta kanatlara kıyasla, bu kanatların daha düşük taşıma kuvvetleri ve erken perdövites eğilimi gösterirler. Akış kontrol metotlarının kullanılmasıyla bu kanatlardaki aerodinamik performans iyileştirilebilir.

Bu çalışmada, doğadan esinlenilmiş hücum kenarı modifikasyonlarının düşük ok açılı delta kanatlar üzerindeki aerodinamik performansa etkisi ve bu kanatlar üzerindeki yer etkisi, kuvvet ölçümleri, yüzey basınç ölçümleri ve yüzeye yakın PIV yöntemleri ile incelenmiştir. Sinusoidal ve testere diş hücum kenarı modifikasyonların etkisini incelemek için toplamda yedi tane keskin kenarlı, 45-derece ok açısına sahip delta kanat kullanılmıştır. Sinusoidal hücum kenarı modifikasyonları kambur balinaların göğüs yüzgecinde bulunan yumrulardan, testere diş kanatlar ise baykuş tüylerinin hücum kenarında bulunan çıkıntılardan esinlenilerek tasarlanmıştır.

Aerodinamik katsayıları sonuçları, doğadan esinlenilmiş kanat modifikasyonlarının perdövitesi ertelediği, daha yumuşak bir perdövites karakteristiği gösterdiği ve perdövites sonrasında taşıma kuvvetinde artış sağladığı gözlemlenmiştir. Yüzeye yakın PIV ölçümleri, yüksek hücum açılarında referans kanat modeli için büyük ölçekli üç boyutlu akış ayrılması gerçekleştiğine işaret etmektedir. Diğer yandan, modifiye kanatların bu ayrılmayı ertelediği görülmüştür. Testere diş kanat modelinin düşük hücum açılarında özgün bir akış yapısına sahip olduğu ve birden fazla ayrılma çizgilerinin olduğu gözlemlenmiştir. Bu durum çoklu anafor oluşumuna işaret etmektedir. Yer etkisi sonuçları yere yakınlık arttıkça maksimum taşıma kuvvetinin bütün kanat modelleri için arttığını, fakat perdövites açısının yer etkisinden bağımsız olduğunu göstermiştir.

Anahtar Kelimeler: İnce Olmayan Delta Kanat, Pasif Akış Kontrol, Deneysel Aerodinamik, Yer Etkisi, Doğadan Esinlenilmiş Kanat Modifikasyonları

To my family

ACKNOWLEDGMENTS

I want to express my deepest gratitude to all those who have supported me throughout this journey. First and foremost, I sincerely thank my advisor, Prof. Dr. Metin Yavuz, and my co-advisor, Dr. Göktuğ Koçak, for their invaluable time, guidance, encouragement, and support.

This study would not have been possible without the support of my mother, Leyla Dikbaş, and my sister, İdil Dikbaş. Their unwavering belief in me kept me motivated, which is why I have come this far in life. Even when I doubted myself, your belief in me has been a great source of strength.

I want to thank all my lab mates for sharing their knowledge. In particular, I am indebted to Cenk Çetin for sharing his invaluable insights, patience, and utmost wisdom. Your insights were crucial to my progress. I want to thank Erdoğan Güneş for his assistance in conducting my experiments. I want to thank Habib Can Tunç for helping print the wing models.

I want to thank Ahmet Emin Sürücü for brainstorming with me about problems every single time. I thank my friends Nimet Yanık, Gizem Karaca, Berat Geçgel, and Emircan Sevinç for their moral support and for always listening to my concerns.

Finally, I want to thank Mr. Mehmet Özçiftçi, Mr. Asım Tan, and Erhan Çağlar for their technical assistance and patience.

TABLE OF CONTENTS

LIST OF TABLES

TABLES

LIST OF FIGURES

FIGURES

LIST OF ABBREVIATIONS

ABBREVIATIONS

DW: Delta Wing

GE: Ground Effect

IGE: In-Ground Effect

LE: Leading Edge

LES: Large Eddy Simulation

LEV: Leading Edge Vortex

MAV: Micro Air Vehicle

MPS: Model Positioning System

NACA: National Advisory Committee for Aeronautics

OGE: Out-of-Ground Effect

PIV: Particle Image Velocimetry

SLE: Sinusoidal Leading-Edge

TE: Trailing Edge

UAV: Unmanned Aerial Vehicle

UCAV: Unmanned Combat Air Vehicles

LIST OF SYMBOLS

SYMBOLS

A	Reference Area
C	Chord Length
C_D	Drag Coefficient
C_L/C_D	Lift-to-Drag Ratio
C_L	Lift Coefficient
C_{max}	Maximum Lift Coefficient
C_M	Pitching Moment Coefficient
$C_{M\ at\ TE}$	Pitching Moment Coefficient at the Trailing Edge
C_P	Pressure Coefficient
F_D	Drag Force
F_L	Lift Force
F_{xb}	Body Frame Drag Force
F_{yb}	Body Frame Side Force
F_{zb}	Body Frame Lift Force
F_{xw}	Wind Frame Drag Force
F_{yw}	Wind Frame Side Force
F_{zw}	Wind Frame Lift Force
L	Reference Length
M_{xb}	Body Frame Roll Moment

M_{yb}	Body Frame Pitch Moment
M_{zb}	Body Frame Yaw Moment
M_{xw}	Wind Frame Roll Moment
M_{yw}	Wind Frame Pitch Moment
M_{zw}	Wind Frame Yaw Moment
P_{dyn}	Dynamic Pressure of the Flow
P_m	Measured Static Pressure
P_∞	Static Pressure of the Flow
Re	Reynolds Number
t	Thickness
U_∞	Free stream velocity
X_p	Pressure Center
X_a	Aerodynamic Center in Pitch
Λ	Sweep Angle
ν	Fluid Kinematic Viscosity

CHAPTER 1

INTRODUCTION

Delta wings are commonly used on Unmanned Aerial Vehicles (UAV), Micro Air Vehicles (MAV), and Unmanned Combat Air Vehicles (UCAV) because of their ability to maintain flow attached to the wing surface at high angles of attack, which, as a result, enhances the lift coefficient and delays stall [1, 2]. In recent years, there has been an increased demand for these aerial vehicles in the civilian and military sectors. This heightened interest increased the popularity of research on the flow control of delta wings. Extensive studies have been conducted to improve the aerodynamic performance of these wings with passive and active flow control methods, some of which include bio-inspired modifications.
Delta wings are classified into two categories according to their sweep angles (Λ): slender (Λ>55°) and non-slender (Λ<55°) delta wings [3]. The flow structure of slender delta wings is well understood; on the other hand, non-slender delta wings are still being researched [4]. Although there are some disadvantages to non-slender delta wings, such as decreased maximum lift and stall angle compared to slender delta wings, non-slender delta wings have high maneuverability and a low structural-weight-to-takeoff-weight ratio [5, 6].

Flow control methods were developed to manipulate flow phenomena such as flow separation, shear layer separation, vortex formation, flow reattachment, and vortex breakdown. Flow control methods are categorized into passive and active flow control, in their requirement for external energy. Active flow control methods require additional energy from an external source, while passive flow control methods do not.

Researchers study bio-inspired structures, such as leading-edge serrations, riblets, grooves, vortex generators, needle-shaped vortex generators, and leading-edge tubercles, as passive flow control methods [7-9]. A significant amount of biomimicry research aims to improve aerodynamic performance, including biomimicking structures from insects, plants, avians, and aquatic animals. Although the research on plants and insects is very limited, investigating avian and aquatic animal structures is a popular topic.

Examples of some bio-inspired structures are shown in Figure 1.1. Structures such as the bluff body grooves observed in the Saguaro Cactus and common shellfish reduce flow separation on the body, causing decreased drag [7, 10]. A similar effect is observed for dragonfly species [7]. Some bird species possess a structure called "Alula" this structure which consists of extra feathers and a digit bone, located at the hand-wing and arm-wing of birds [7, 11]. This structure generates tip vortices, causing a lift enhancement and a delay of stall [7, 11, 12]. The structures called hind wings are possessed by some butterfly species and contribute to the lift at a critical Reynolds range [7].

Researchers have studied the feathers of different owl species to improve the aerodynamic performance of wings. In these studies, the leading-edge serrations of owl feathers were mimicked. Leading-edge serrations serve as needle-shaped vortex generators, creating more stable vortex structures with decreased diameters and delayed vortex breakdown [8].

Recently, structures from marine animals, such as the tubercles of humpback whales, have received a significant amount of interest from researchers, since these structures improve the whale's maneuverability in the water, serving as vortex generators [13-16]. Most of the research on the effects of the sinusoidal leading edge (SLE) is conducted on airfoils, while a few studies investigate the effects of SLE on delta wings. The effect of amplitude and wavelength on the aerodynamic or hydrodynamic performance of SLE models was the main focus of these investigations.

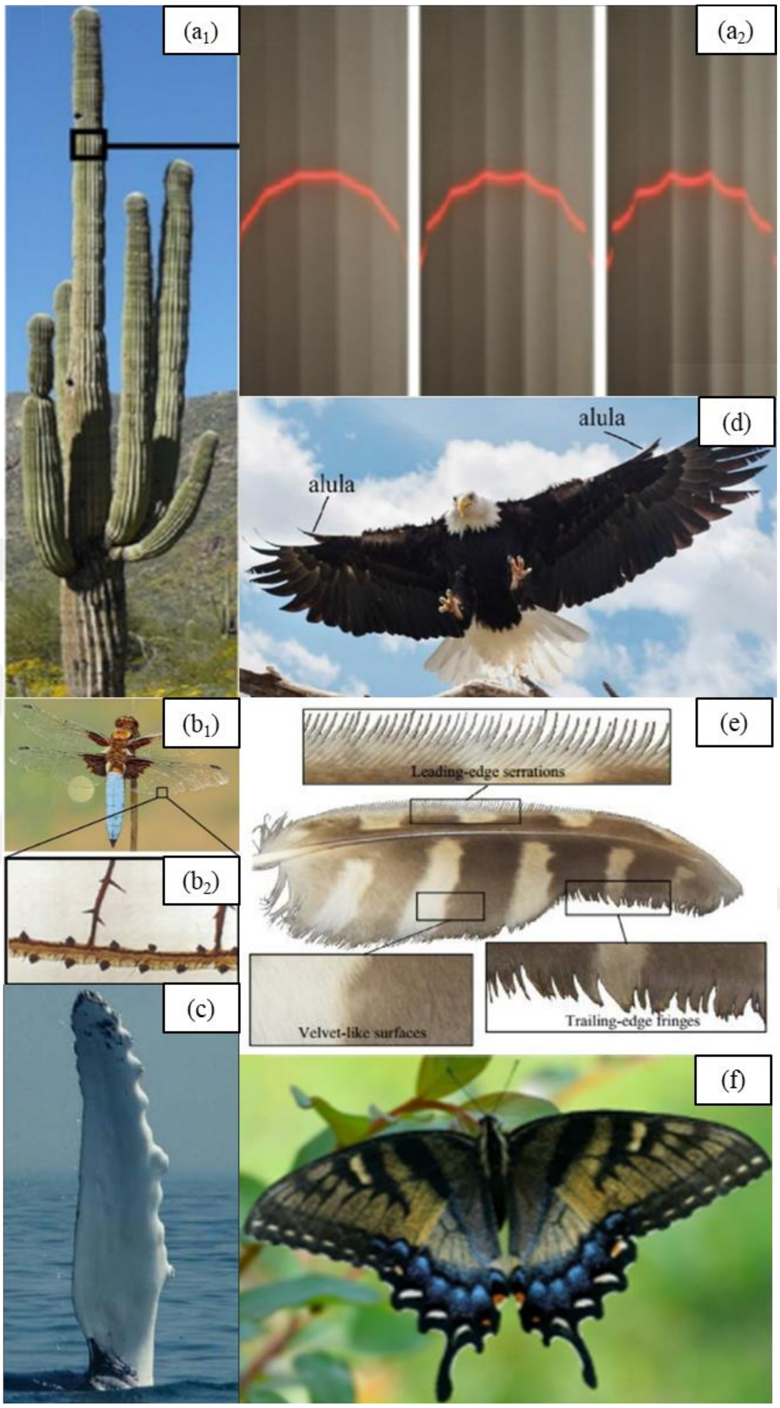

Figure 1.1 Examples of bio-inspired structures in nature. (a_1 - a_2) Grooved surface structure of a Saguaro Cactus. (b_1 - b_2) Wing protrusions of Odonaya Dragonfly. (c) Tubercled structure of the pectoral fins of a humpback whale. (d) Alula structure. (e) Leading-edge serrations of owl feathers. (f) Hind-wing tail of a butterfly [7, 8, 17].

When an aircraft or animal flies near the ground, a phenomenon known as the "ground effect" is produced. Span-dominated ground effect significantly affects the wing when the ground clearance approaches approximately one wingspan. Span-dominated ground effect results in decreased drag and increased lift [18]. In the chord-dominated ground effect cases, the ground clearance is significantly lower than in the span-dominated cases [18], [19], [20]. The proximity of the wing to the ground results in an air cushion forming between the wing and the ground, which increases the lift-to-drag ratio [18]. Wingtip vortices form, and the pressure beneath the wing increases as an alteration in the flow between the wing surface and the ground plane [21]. The effect of the ground is especially significant on in-flight performance during take-off and landing [22]. Special aircraft called wing-in-ground (WIG) are designed to take advantage of the ground effect.

Some bird and bat species, including petrels, pelicans, skimmers, ospreys, fish eagles, fishing owls, and fishing bats, take advantage of the ground effect by flying over water to lower the cost of flying [21, 22]. Many researchers have investigated the effect of the ground on the aerodynamics of animal flight, but only a few have investigated the effect of the ground on bio-inspired wing modifications.

1.1 Motivation of the Study

Modern aerial vehicles, such as Unmanned Aerial Vehicles (UAV), Micro Air Vehicles (MAV), and Unmanned Combat Air Vehicles (UCAV), experience complex flow structures during steady and unsteady flight. Certain aspects of the flow structures, such as vortex structures, vortex breakdown, and three-dimensional flow separation of these vehicles, must be well understood to enhance flight performance.

Implementing flow control methods, such as passive flow control, can help improve some disadvantages of non-slender delta wings, notably their stall characteristics. Since passive flow control methods do not require additional energy, they are relatively easier to study and implement than active flow control methods. Moreover, the effect of the ground on these modified wing models is crucial for understanding their performance during lift-off and landing. The primary motivation of this study is to enhance the aerodynamic performance of non-slender delta wings with nature-inspired designs and investigate the effect of the ground on these wing models.

1.2 Aim of the Study

This study aims to investigate the effects of bio-inspired leading-edge modifications on a $\Lambda = 45°$ swept delta wing in out-of-ground and static ground effects, using force and pressure measurements. The bio-inspired leading-edge modifications used in the present study are shown in Figure 1.2. The effects of wavelength and amplitude on the aerodynamics of bio-inspired non-slender delta wings with a sweep angle of 45 degrees were investigated in a low-speed wind tunnel using force, pressure, and particle image velocimetry measurements. The force and pressure measurements were conducted at a Reynolds number of $Re = 100{,}000$, while the particle image velocimetry measurements were conducted at a Reynolds number of $Re = 75{,}000$. Three different amplitude-to-chord ratios, from 0.03 to 0.01, and three different wavelength-to-chord ratios from 0.1 to 0.3, were investigated. Four different wings with sinusoidal-leading-edge modifications and two different wings with saw-tooth leading-edge modifications were used in this study. The effect of ground on these bio-inspired and saw-tooth wings was investigated at various height-to-chord ($h/C(\%)$) ratios of 16%, 27%, 50%, and 116%.

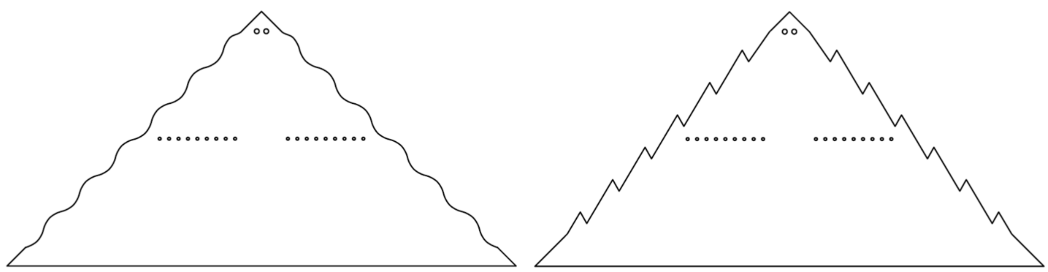

Figure 1.2 Leading-edge modifications utilized in this study.

1.3 Structure of the Thesis

This thesis consists of five main chapters. Chapter 1 provides introductory information about flow over non-slender delta wings, biomimicry, ground effect, the motivation of the study, and the aim of the study.

Chapter 2 provides a detailed literature review of studies on the flow structures around delta wings, flow control methods, bio-inspired modifications, and the effect of ground.

Technical details about the experimental setup and measurement techniques, such as force measurements, pressure, and particle image velocimetry measurements, are provided in Chapter 3.

The results of the study are provided in Chapter 4. First, the force measurement results for out-of-ground and in-ground effects are reported. Then, pressure measurement results are reported for the out-of-ground effect and the static-ground effect results. Finally, near-surface PIV results are reported in the out-of-ground effect.

The conclusions throughout this study are provided in Chapter 5, including recommendations for possible future work.

CHAPTER 2

LITERATURE SURVEY

This chapter provides a literature review regarding the essential delta wing flow structures and studies regarding flow control techniques used in this study.

2.1 Flow Past Delta Wings

A vast amount of information is available regarding the flow structures around slender delta wings. However, the flow structures around non-slender delta wings are still being researched since the wing's sweep angle significantly affects flow phenomena such as flow separation, shear layer separation, vortex formation, flow reattachment, and vortex breakdown [4].

The typical flow structure over a delta wing is shown in Figure 2.1. Flow over a delta wing typically features vortex sheets that separate from the leading edge of the delta wing and roll up into stable vortices, generating a coherent primary vortex structure [23-25]. The primary vortex structure was experimentally visualized even for very low angles of attack [24]. Leading-edge vortices provide additional lift due to the suction force generated by this structure; this additional lift is called the vortex lift [26]. A non-slender delta wing demonstrates a secondary vortex structure outboard of the primary vortex over low angles of attack. This structure is identified as a dual-vortex structure [24, 27].

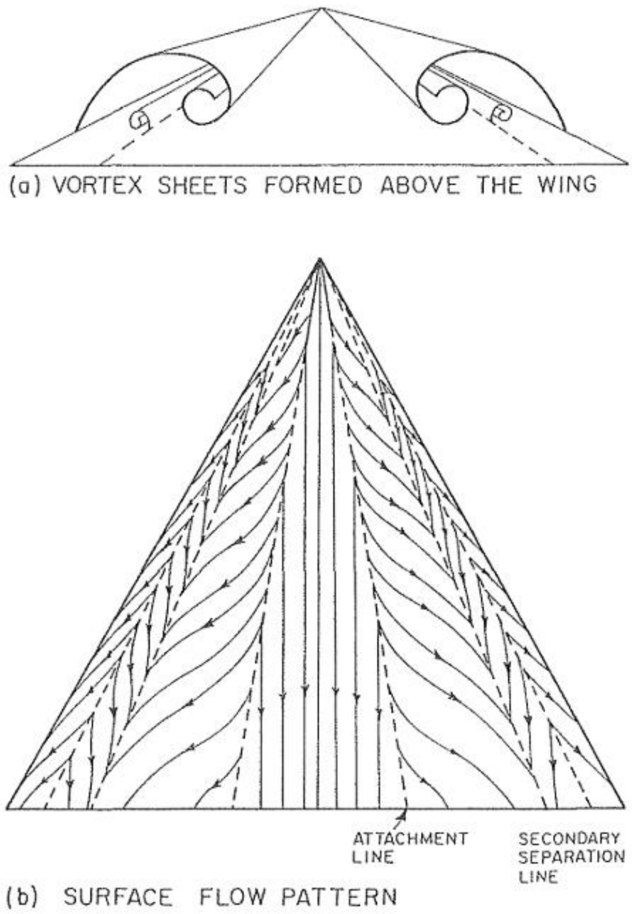

Figure 2.1 Typical flow over delta wings: a) leading-edge vortices, b) surface flow pattern [23].

Vortex breakdown is a phenomenon observed at high angles of attack, where the size of the leading-edge vortices and the dynamic pressure increase suddenly [26]. This phenomenon is characterized by an internal stagnation point formation on the vortex axis, followed by a reversed flow [28]. Vortex breakdown is undesirable as it can significantly increase drag and decrease lift. Sarpkaya et al. [29] experimentally investigated swirling flows inside a diverging cylindrical tube and classified vortex breakdown into three types: double helix (mild), spiral, and near-axisymmetric or bubble breakdown, as shown in Figure 2.3. However, some researchers and reviewers suggest that there are six or seven types of vortex breakdown [28, 30]. Mainly two vortex breakdown types, bubble and spiral forms, were reported above delta wings [31-34]. The vortex breakdown is similar for slender and non-slender delta wings, yet the breakdown is less abrupt for non-slender delta wings [27]. The location of the vortex breakdown varies in delta wings with angle of attack and sweep angle. As the angle of attack increases, the vortex breakdown moves towards the apex, and as the sweep angle increases, it moves towards the trailing edge [35].

The stall is a sudden loss of lift experienced by the wing when it exceeds a critical angle of attack. As the critical angle is exceeded, flow separation occurs, disrupting the smooth flow over the wing's surface. The stall can be categorized as a static or dynamic stall. McCroskey et al. [36] characterized the dynamic stall by vortex shedding and a viscous disturbance over the lifting surface, which provokes the pressure field to fluctuate.

Stall onset occurs when the attachment line reaches the wing's centerline, and shear layer reattachment is no longer possible [23, 27]. When this happens, the streamline pattern takes the form of a 'whorl' or 'swirl', as shown in Figure 2.2 [23, 24, 27]. The stall causes safety concerns because of a sudden loss of lift. Therefore, there are numerous studies to delay the stall angle with active and passive flow control methods.

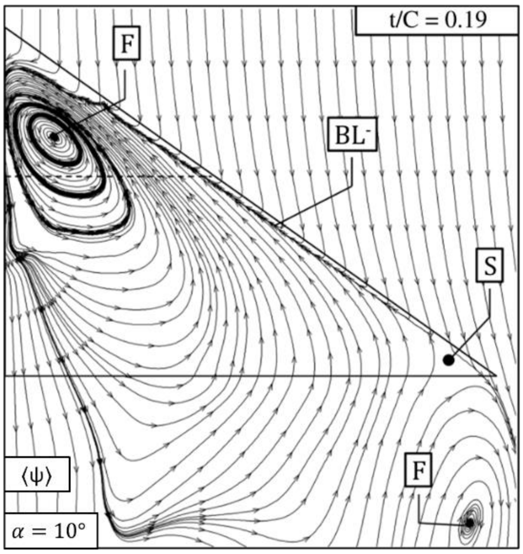

Figure 2.2 Time-averaged surface streamline patterns demonstrating three-dimensional separation [37].

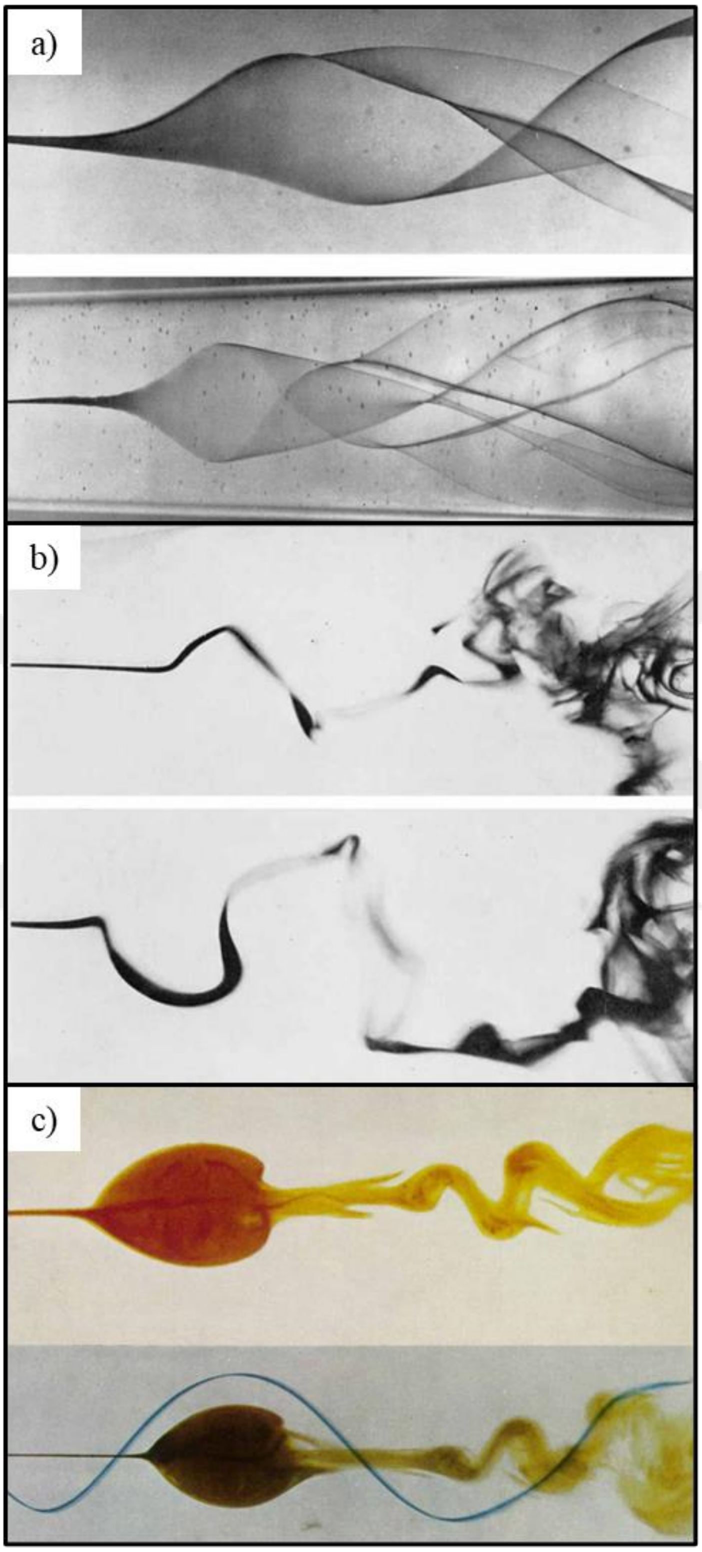

Figure 2.3 Three types of vortex breakdown: a) double-helix breakdown, b) spiral breakdown, c) near-axisymmetric breakdown [29].

2.2 Flow Control Methods on Delta Wings

Flow control methods include the manipulation of some flow phenomena, including flow separation, shear layer separation, vortex formation, flow reattachment, and vortex breakdown. These methods are used to optimize the aerodynamic performance by increasing lift, decreasing drag, delaying stall, postponing flow separation, suppressing noise, generating forces and moments for flight control, and decreasing buffeting [38, 39, 40].

Flow control methods can be classified into two methods: passive and active flow control. The distinction between these flow methods is made by the requirement of external energy. Active flow control methods require additional energy from an external source, including techniques such as control surfaces, steady and unsteady excitation, pneumatic devices, and plasma actuators [1]. Meanwhile, passive flow control methods do not require any additional energy. This method includes techniques such as alterations to the leading-edge shape and the development of multiple vortex arrangements [1].

2.2.1 Active Flow Control

Active flow control methods work with the principle of controlling the speed, direction, and stability of the fluid flow by changing the velocity, temperature, and pressure of the fluid [41]. Active flow control strategies can be classified as predetermined and reactive methods. Predetermined methods utilize both uniform and non-uniform energy consumption, while reactive flow control methods utilize in situ sensors to regularly tune the power consumption of the controllers [42].

Gursul et al. [43] created a feedback control system using the pressure fluctuations caused by vortex breakdown as the control signal to actively control vortex breakdown. Wood et al. [44] utilized tangential leading-edge mass injection to increase the maximum normal force coefficient by approximately 30 percent, resulting in an increased lift at high angles of attack via stabilization of the vortical flow. Williams et al. [45] investigated the effect of oscillatory blowing at the leading edge on a delta wing with a sweep angle of $\Lambda = 50°$. They observed a substantial increase in surface suction force and a delay of the stall angle. Sidorenko et al. [46] used a dielectric barrier discharge plasma located at the surface of the wing model to control vortex flow. Çetin et al. [47] investigated the effect of unsteady and steady blowing on the flow structure of a delta wing utilizing surface pressure, PIV measurements, and smoke visualization [36].

2.2.2 Passive Flow Control

Passive flow control methods are cost-effective and reliable due to their simplicity. However, this method is less effective than active flow control methods and is less adaptive to changes in flight conditions. Structures such as leading-edge serrations, riblets, surface topography, grooves, vortex generators, such as needle-shaped vortex generators, and leading-edge tubercles are studied by many researchers as passive flow control methods [7, 8, 9].

Klute et al. [48] proposed using an apex flap to delay vortex breakdown and observed that the apex flap effectively delayed the vortex breakdown. Çelik et al. [38] characterized the flow structure of non-slender delta wing models with leading and trailing edge modifications inspired by white-sided dolphins using smoke visualization methods. The surface-flow smoke visualizations from this study are given in Figure 2.4. Kayacan et al. [49] utilized a passive flow control method called passive bleeding to study the effects of this method on the flow characteristics of a non-slender delta wing and revealed that this method delayed the stall and increased the lift coefficients at all angles of attack. Other researchers studied nature, looking for inspiration for a new design. Johari et al. [50] were prominent examples of bio-inspired wing modification studies.

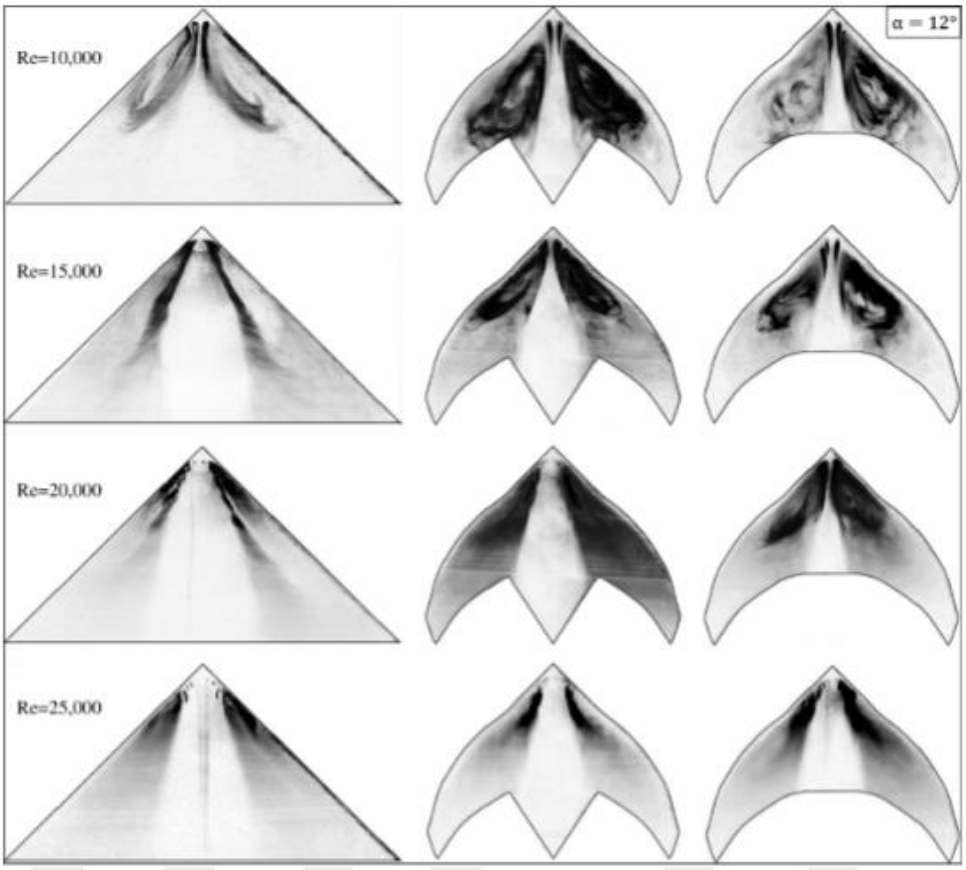

Figure 2.4 Flow visualization of bio-inspired wing modifications [38].

2.2.2.1 Bio-Inspired Modifications

Ever since the first cell developed, it has evolved with every challenge it encountered. Over long time periods, all organisms have adapted to perform optimally. Humanity has long been inspired by nature and the practice of observing and mimicking structures from nature. This practice, known as biomimicry, can be traced back to Leonardo DaVinci's works. Biomimicry is beneficial in bypassing time-consuming design processes by leveraging Charles Darwin's natural selection theory [7].

Otto Lilienthal [51] conducted one of aviation's earliest and most influential studies on biomimicry. In his research, he mimicked various wing shapes and movements of different bird species to make human flight possible. Many researchers [8, 9, 11, 52] and engineers followed the same path and researched avians to design or improve aerial vehicles. One of the most well-known examples of these studies of biomimicry in the aviation sector is the Northrop B-2 Spirit, inspired by the peregrine falcon [53]. A comparison of the B-2 Spirit and a peregrine falcon is shown in Figure 2.5.

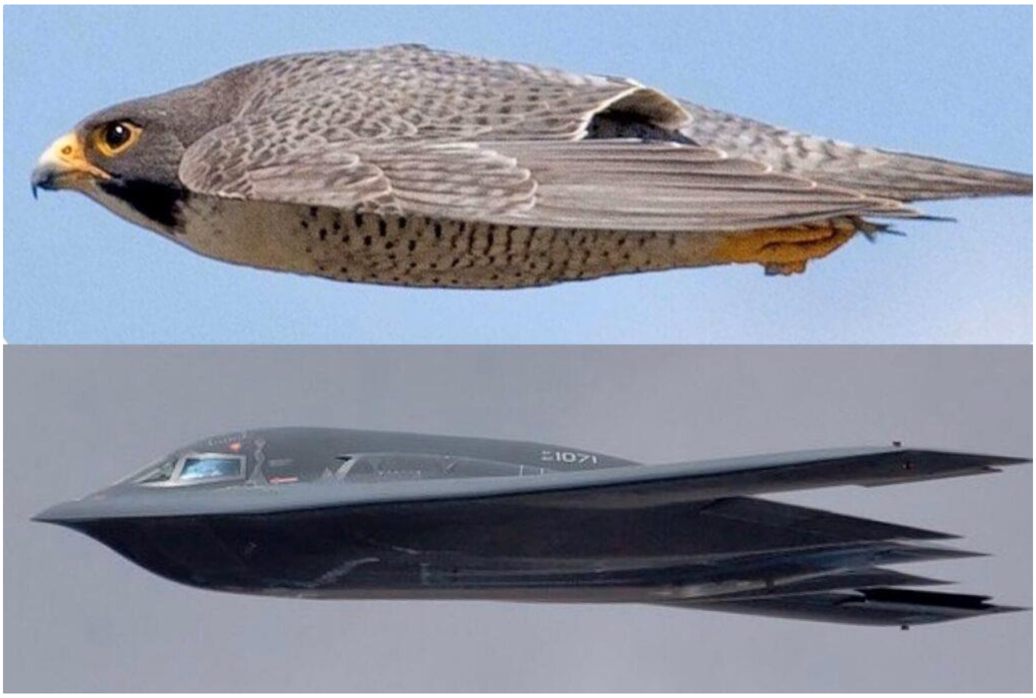

Figure 2.5 The inspiration behind B-2 Spirit [53].

However, avians are just one source of inspiration for aerodynamics research. Structures from aquatic animals, insects, and even plants can be utilized to improve aerodynamic performance [7]. Recently, marine animals have received attention from researchers since the Reynolds numbers for aquatic animals are similar to those of modern aerial vehicles, unlike avians [16]. These researchers have investigated the effects of various marine animal structures, such as fish scales, skin topography, and leading-edge tubercles, to decrease drag, delay transition, and improve aerodynamic efficiency [10, 54, 55]. Some of these structures are shown in Figure 2.6.

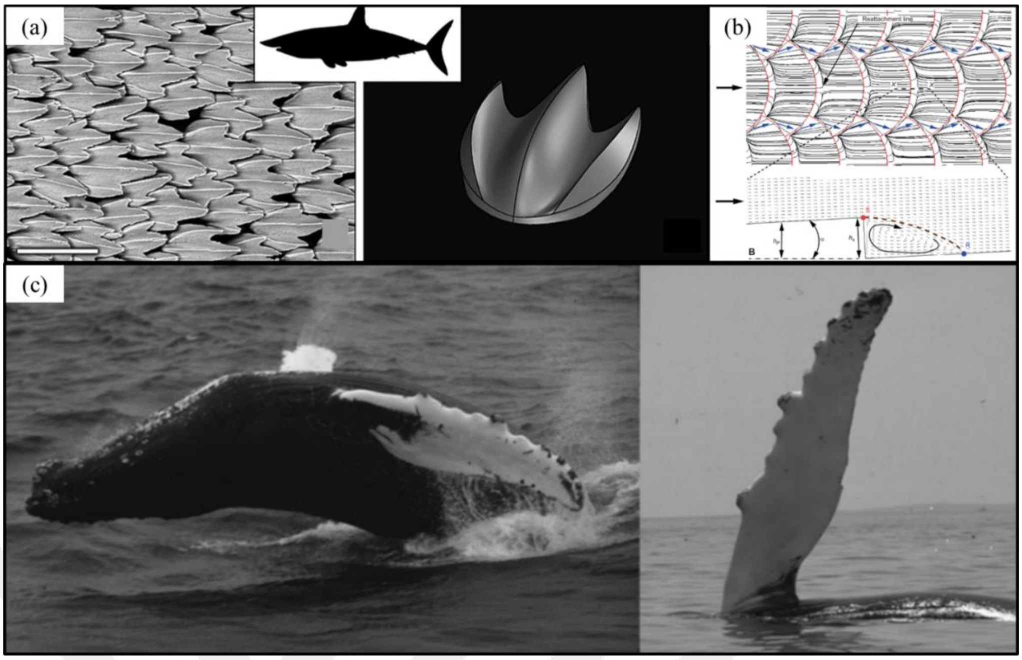

Figure 2.6 Marine animal structures: (a) shark skin topography [54], (b) fish scales [55], and (c) humpback whale tubercles [13].

Among these structures, the tubercles of humpback whales draw a significant amount of attention. These structures serve as vortex generators and improve the whale's maneuverability in the water [13-16]. Most of the studies investigating the effects of these structures study the effect of SLE on airfoils, while a few investigate the effects of SLE on delta wings. These studies mainly focused on the effect of amplitude and wavelength on the aerodynamic or hydrodynamic performance of SLE models. Some of the models used in these studies are given in Figure 2.7. Other researchers studied the effect of sinusoidal leading-edge modifications with visualization methods such as particle image velocimetry (PIV) [56, 57], tuft flow visualization [50], hydrogen-bubble visualization [58], and surface oil-flow visualization [14, 58, 59].

Johari et al. [50] were among the first research groups to focus on airfoils with sinusoidal leading-edge (SLE) modifications inspired by humpback whale tubercles. They conducted force measurements and the tuft flow visualization method to investigate the effects of SLE on aerodynamic performance and flow characteristics.

The results of this study showed that the airfoils with SLE modifications did not stall in the same characteristics as the baseline airfoil. Moreover, the results showed that the poststall lift coefficients were higher when SLE modifications were utilized. Guerreiro et al. [60] investigated the aerodynamic performance of the NASA LS(I)-0417 profile with SLE modifications at Reynolds numbers of $Re = 7 \times 10^4$ and $Re = 1.4 \times 10^5$. The results of this study indicated that the wings with SLE modifications are affected less by the change in the Reynolds number than wings with no modifications [60]. Hansen et al. [61] studied the effect of SLE on a NACA 0021 airfoil and compared two-dimensional and three-dimensional models of this airfoil at $Re = 1.2 \times 10^5$. This study indicated that the smallest amplitude and smallest wavelength configuration of tubercles performed the best for both two-dimensional and three-dimensional cases. Van Nierop et al. [62] experimentally studied the SLE modifications on a swept wing. The lift coefficient of the SLE wing models was observed to be higher than the base wing at the post-stall regime.

Yoon et al. [16] numerically studied the hydrodynamic characteristics of SLE modifications on the NACA 0020 airfoil with various waviness ratios at $Re = 2{,}000{,}000$. The results of this study showed that as the waviness increases, the stall occurs earlier than that of the base model. However, the wings with SLE modifications had a higher lift coefficient in the post-stall region [16]. Kim et al. [63] conducted similar research with Yoon et al. and reached the same verdict. Zhao et al. [64] conducted a large eddy simulation (LES) on a NACA 0021 airfoil with and without SLE modifications and studied the effect of amplitude on the flow structure. The results of this study indicated that the flow separation was delayed and the aerodynamic performance was improved for large amplitudes. Ntantis et al. [65] studied the effect of SLE modifications on NACA 2421 airfoil with four different taper ratios at $Re = 10^6$. The effect of the length of the tubercles, amplitude, and wavelength was investigated. This study showed that the maximum lift coefficient was increased in a certain wing model with full-span SLE modifications. Moscato et al. [17] conducted a numerical study to investigate the effects of SLE modifications on force coefficients, flow fields, turbulence production, and flow reattachment. This study showed that using SLE modifications increased the maximum lift coefficient, delayed the stall angle, reduced the level of turbulence production, and prevented separation and backflow on the wing's upper surface. Moreover, the post-stall behavior was smoother than the unmodified wing [17]. Ramakrishna et al. [2] compared the effects of leading-edge design on a delta wing having a sweep angle of $\Lambda = 65°$. Three different leading-edge designs were used: Plane delta wing, with no modifications, saw-tooth delta wing, and sinusoidal delta wing. The results showed that the saw-tooth wing model delayed stall more than other models [2]. Moreover, the lift-to-drag ratio of the saw-tooth model was higher than other models. The sinusoidal wing model performed better than the plane wing regarding the lift-to-drag ratio but did not exceed the saw-tooth wing model [2]. Bolzon et al. [66] conducted a wake survey on two swept wings with NACA 0021 airfoil profiles at a Reynolds number of $Re = 2.25 \times 10^5$. The wake survey showed that sweeping a wing with SLE modifications resulted in an asymmetry in the vortex strength. The wingtip vortices of different wing models were similar below the angle of attack of 3°. When the angle of attack exceeds 6°, the wing without modifications produces a stronger wingtip vortex [66].

Chen et al. [57, 58] investigated the effects of SLE modifications on a delta wing with a sweep angle of $\Lambda = 52°$. Nine different wing configurations were used to investigate multiple amplitudes and wavelengths. The force measurements showed results similar to those of Johari et al. [50]. The results indicated that when the amplitude was increased above a critical value, the maximum lift coefficient decreased significantly, and the stall was delayed when SLE modifications were utilized [57, 58]. Moreover, cross-PIV measurements of the 4M wing model revealed that the vortex structure of the SLE wing was much different from that of the baseline case. Multiple leading-edge vortices (LEV) existed on the leeward side of the SLE delta wing, but these LEVs were observed to decay faster than the base model [57]. Goruney et al. [56] investigated the near-surface flow patterns of an SLE delta wing with a sweep angle of $\Lambda = 50°$ at a Reynolds number of $Re = 1.5 \times 10^4$. The findings of this study showed that the focus of three-dimensional separation moved toward the leading edge as the amplitude of the SLE was increased. When the amplitude surpasses a critical point, the focus of three-dimensional separation is eliminated and replaced by a focus of attachment [56].

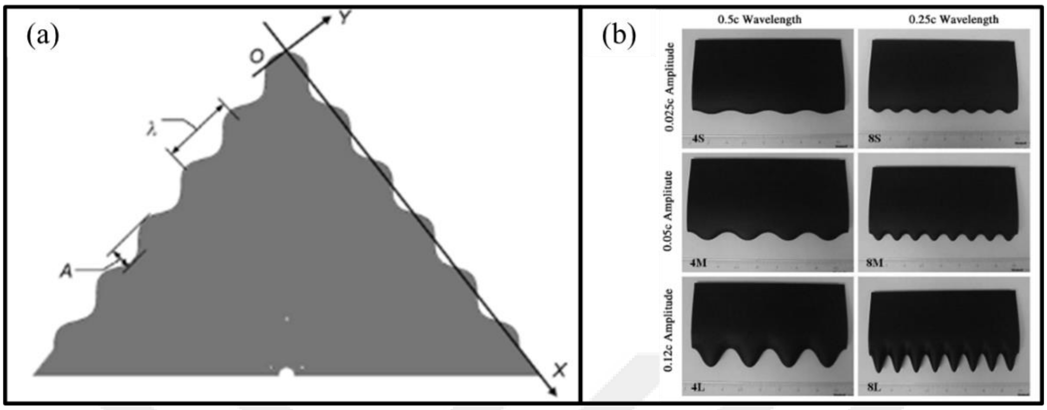

Figure 2.7 SLE wing models used in the studies of (a) Chen et al. [58] and (b) Johari et al. [50].

2.3 Ground Effect

Recent studies and engineering advancements have focused on exploiting the effect of the ground, an aerodynamic phenomenon that occurs when an animal or an aircraft flies close to the ground. The flow between the wing surface and the ground plane is altered, which results in increased pressure underneath the wing, decreased energy cost of flying, and the development of wingtip vortices [21]. Ground effect is especially significant in flight performance during take-off and landing [22]. Some vehicles are designed to take advantage of the ground effect, called the wing-in-ground effect (WIG) vehicles. These vehicles create an air cushion under their wings to carry higher loads and increase the service speed for transportation and military purposes [67]. Some wing-in-ground effect (WIG) vehicles are given in Figure 2.8.

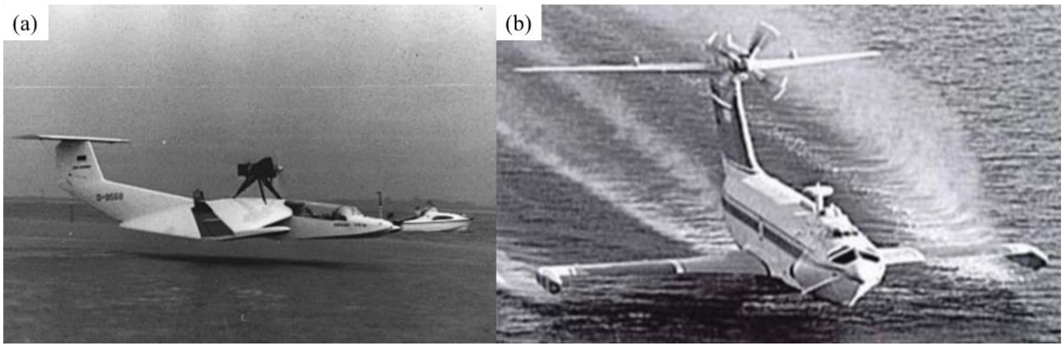

Figure 2.8 WIG vehicles (a) Lippisch X-113 (b) Orlyonok [67].

Some bird and bat species, including petrels, pelicans, skimmers, ospreys, fish eagles, fishing owls, and fishing bats, take advantage of the ground effect by flying over water to lower the cost of flying [21, 22]. Many researchers have investigated the ground effect on the aerodynamic performance of animal flight, but only a few have investigated the effect of the ground on bio-inspired wing modifications.

Koçak et al. [68] investigated the effect of ground on aerodynamic performance and stability of a non-slender delta wing at a Reynolds number of $Re = 9 \times 10^4$. The results of this study indicated that when the ground effect intensity is increased, the aerodynamic performance at all angles of attack is improved, and the stall onset was observed to be delayed for wings closer to the ground [68]. Moreover, as a result of the ground effect, an increase in the slopes of lift coefficient (C_L) and pitch moment coefficient (C_M) is observed resulting in movement of pressure center (X_p) and aerodynamic center in pitch (X_a) towards the aft side of the wing. However, the movement of the aerodynamic center moves ever so slightly. Therefore, the movement is insufficient to ensure stability [68]. Koçak et al. [69] conducted another study on the effect of both static ground effect and dynamic ground effect on a non-slender delta wing at $Re = 9 \times 10^4$. A moving belt mechanism was utilized to simulate the dynamic ground effect. The comparison of the static ground effect with the dynamic ground effect showed that the lift coefficient was higher for the dynamic ground effect, which was mainly due to the highly turbulent aerodynamic interactions for IGE cases compared to OGE cases. Additionally, the slopes for drag coefficient, lift coefficient, and pitch moment coefficients were generally reduced for the dynamic ground effect [69]. The lift-to-drag ratios are similar for static and dynamic ground effects for both OGE and IGE cases below a certain angle of attack. However, when this angle of attack is exceeded, there is a more distinguished decrease in the lift-to-drag ratio in the dynamic ground effect than in the static ground effect [69].

Tumse et al. [6] investigated the ground effect on the aerodynamic performance and flow characteristics of a delta wing with a sweep angle of $\Lambda = 40°$ by utilizing Particle Image Velocimetry (PIV), force measurements, and dye flow visualization technique. This study showed that the lift-to-drag ratio (C_L/C_D) was increased as the distance between the ground and the wing decreased, especially at lower angles of attack [6]. Moreover, the breakdown of leading-edge vortices occurred earlier when the wing was under the effect of the ground [6]. Tasci et al. [70] investigated the effect of ground on the flow characteristics of a slender delta wing with a sweep angle of $\Lambda = 70°$ at a Reynolds number of $Re = 2.5 \times 10^4$. Techniques such as PIV and flow visualizations were utilized in this study. This study revealed that GE induces an earlier leading-edge vortex breakdown compared to OGE [70]. As the height between the wing and the ground plane decreases, the size and the extent of the primary and secondary vortices increase, and the aerodynamic coefficients increase. Moreover, the drag and lift coefficients increase [70].

Qu et al. [71] studied the ground effect on a swept-back delta wing at 20° angle of attack numerically. The results of this study showed that as the height of the wing and the ground plane decreases, the drag, lift, and nose-down moment increase. The vortex breakdown is observed earlier when the wing is in GE [71].

Ahmed et al. [72] studied the effect of ground on the aerodynamic performance over an NACA 0015 airfoil. This study showed that the lift force increased when the ground clearances were low due to the higher pressure on the lower surface of the airfoil [72]. At higher angles of attack, a thick wake region was observed on the airfoil's upper surface due to a decrease in pressure on the suction side, and the flow separation occurred earlier when the airfoil was under the effect of the ground [72]. Zhang et al. [73] investigated the off-surface aerodynamic characteristics of an airfoil in ground effect with Laser Doppler Anemometry and Particle Image Velocimetry methods. The results of this study showed that as the ground clearance is reduced, the flow is accelerated, thereby increasing the pressure recovery demand. As the height between the wing and the ground is decreased further, a critical value of the wing generates more downforce, which results in stall [73].

2.3.1 Ground Effect on Bio-Inspired Wings

Some bird and bat groups utilize the ground effect by flying over water. Such groups include petrels, pelicans, skimmers, ospreys, fish eagles, fishing owls, and fishing bats [22]. Some species of these animals are given in Figure 2.9. These animals use the ground effect to lower the cost of flying [21].

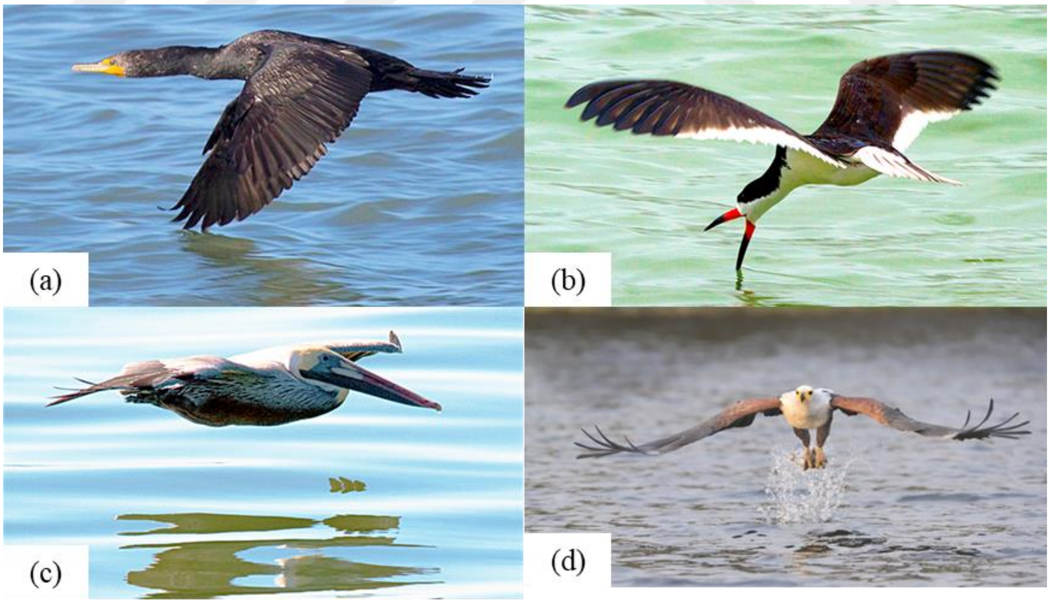

Figure 2.9 Birds that use ground effect: (a) Cormorant, (b) Black Skimmer, (c) Eastern Brown Pelican [74], (d) African Fish Eagle [75].

Many researchers study the effect of the ground on the aerodynamics of animal flight. However, only a few researchers have studied the effect of the ground on bio-inspired wing modifications. Mehraban et al. [76] studied the effect of ground on NACA 63_4-021 airfoil profile wings. In an experimental setup, they compared a baseline wing with six different sinusoidal leading-edge wings with different amplitudes and wavelengths. The wings were tested in three different ground clearances. Results of this study indicated that an increase in the amplitude of the tubercles when in ground effect could prevent stalling, particularly for shorter wavelengths [76]. Lu et al. [77] studied the effect of ground on a three-dimensional flapping wing. The effect of several parameters, such as different wing shapes, wing kinematics, and Reynolds numbers, was studied. This study used three different wing shapes: elliptic wing, hawkmoth wing, and fruit fly wing, as shown in Figure 2.10 (a), along with the flapping mechanism shown in Figure 2.10 (b). Three different wing kinematics were used to mimic insect flight: sweeping, elevating, and twisting. The bio-inspired wings performed the wing kinematics of their respective insects, while the elliptic wing performed simple harmonic motions. In this study, the leading-edge vortices (LEV) were observed to be still attached to the wing even when the wing was closest to the ground, causing a significant lift enhancement. Moreover, a decrease in drag was observed when the wing was closest to the ground due to a decreased downwash strength. There was a similar reaction to the ground effect for all wing kinematics and wing shapes.

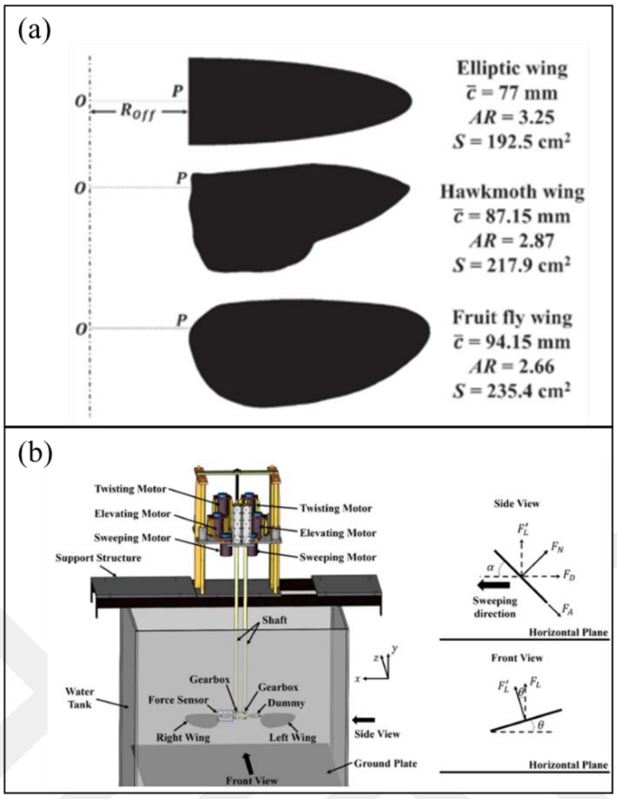

Figure 2.10 (a) Bio-inspired wing shapes, (b) flapping mechanism used in the study of Lu et al. [77].

Abdizadeh et al. [78] conducted research similar to that of Wu et al., investigating the ground effect on a flapping airfoil inspired by the wing structures of dragonflies. The dragonfly airfoil was compared with an NACA4412 airfoil. They observed that as the distance between the ground and the airfoil decreases, there is a significant increase in the lift coefficient. Wu et al. [79] studied an oscillatory "flapping wing" in ground effect. This study investigated the effects of the distance between the airfoil pitching axis and the ground and the flapping motion's amplitude and frequency. The lift force was increased when the wing was in the presence of ground effect.

CHAPTER 3

EXPERIMENTAL SET-UP AND MEASUREMENT TECHNIQUES

This chapter provides details about the wind tunnel used for conducting the experiments, wing models, and measurement techniques such as force, pressure, and particle image velocimetry measurements.

3.1 Wind Tunnel

Experiments were conducted in a low-speed, suction-type, open-circuit wind tunnel in the Fluid Mechanics Laboratory of the Mechanical Engineering Department at Middle East Technical University. The wind tunnel has five main parts: a settling chamber, a contraction cone, a test section, a diffuser, and a fan. The wind tunnel is shown in Figure 3.1.

Figure 3.1 Wind tunnel facility.

The wind tunnel has two symmetrical inlet sections at the sides, with fine mesh screens to prevent foreign objects from entering the system and increase air uniformity. The settling chamber helps keep the turbulence intensity low and uniformity of the air high with a honeycomb structure and three additional fine mesh screens; this section has a 2700 mm length. The contraction cone has a 2000 mm length and a contraction ratio of 8:1. The test section, which has transparent walls, has 750 mm width, 510 mm height, and 2000 mm length. The test section of the wind tunnel is shown in Figure 3.2. The diffuser, located at the end of the test section, decelerates the high-speed airflow to increase the static pressure, hence decreasing the power requisition of the wind tunnel. This section is 7300 mm in length. An axial fan with a 10kW AC motor is assembled at the exit of the wind tunnel with a remote-control unit to control the velocity of the test section. The test section has a maximum freestream velocity of 20 m/s.

The experiments were conducted at various free stream velocities with corresponding Reynolds numbers, calculated with Eqn. 3-1.

$$Re = \frac{U_\infty C}{\nu} \tag{3-1}$$

Figure 3.2 Test section of the wind tunnel.

3.2 Wing Models

Seven different sharp-edged delta wing models were used with a 45-degree sweep angle (Λ) and a single-sided bevel on the windward side at a 45-degree angle. The chord (C), the span (S), and the thickness (t) of the delta wing models are 135 mm, 270 mm, and 80 mm, respectively. The suction side area of each modified wing model is approximately the same as the base wing's area, as shown in Table 1. The delta wing models were designed to access the pressure and smoke visualization channels from the trailing edge. There are nine pressure channels in each half of the wing, eighteen pressure channels in total at a chordwise distance of $x/C = 0.5$ for each wing model. The diameter of the pressure tabs is 1.5 mm. The maximum blockage ratio is lower than 3% at the highest angle of attack of $\alpha = 30°$.

Table 1 Suction side areas of each wing model and area changes compared to the base wing model.

Model	**Area (mm^2)**	**ΔA (mm^2)**
Base	18225	0
S-λ1ϕ02	18224.47	0.53
S-λ2ϕ03	18220.95	4.05
S-λ2ϕ05	18220.57	4.43
S-λ3ϕ05	18216.13	8.87
ST-λ2ϕ03	17741.17	483.83
ST-λ2ϕ05	18205.19	19.81

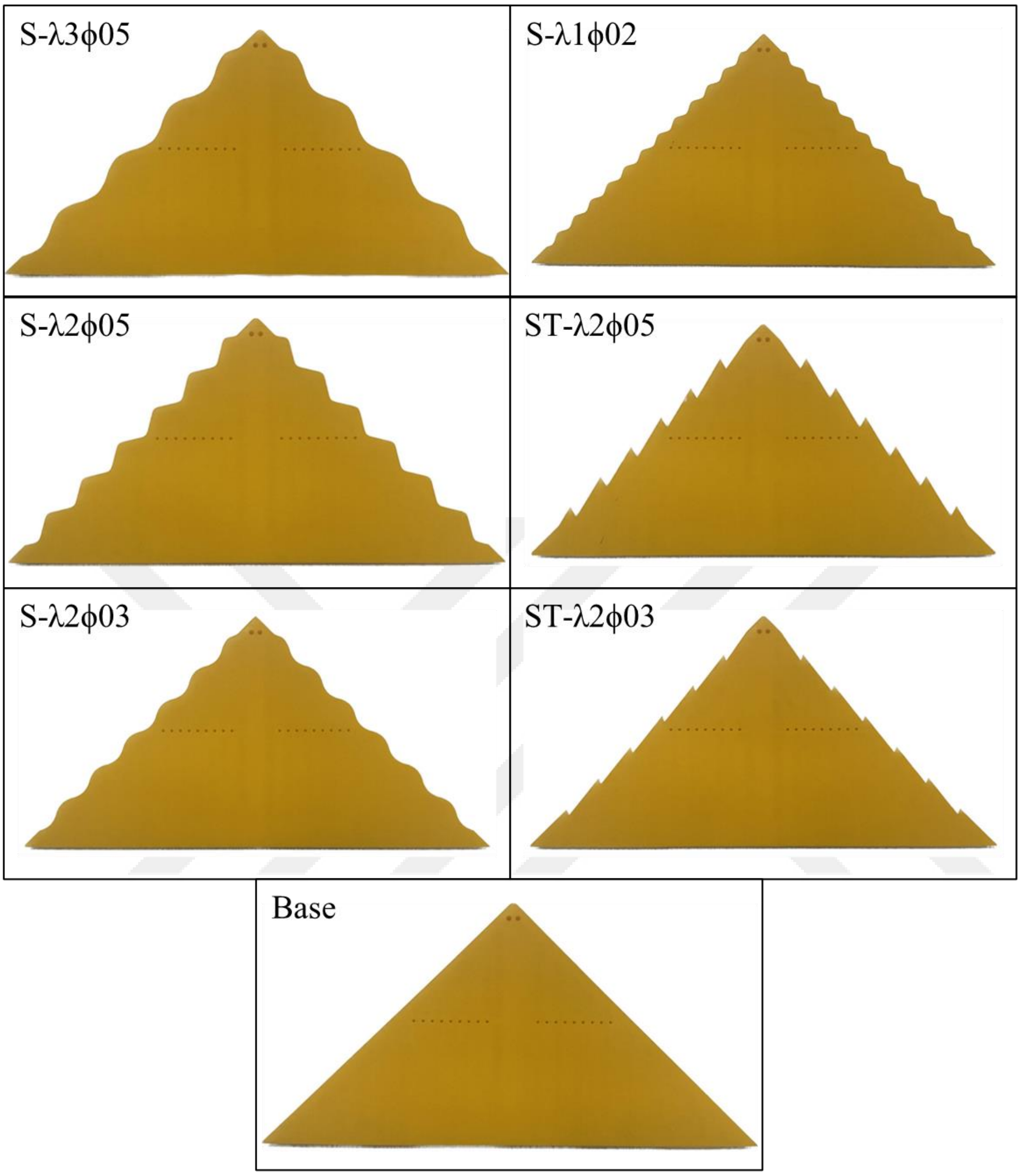

Figure 3.3 Delta wing models.

This study uses two different model groups: the sinusoidal and the saw-tooth leading-edge groups. The sinusoidal-leading-edge wing models used in this study were inspired by the tubercle structure of humpback whales and were compared with a reference wing and two different saw-tooth leading-edge models inspired by the leading-edge serrations of owl feathers and the studies of Ramakrishna et al. [2]. The wing models used during this study are given in Figure 3.3. Configurations for the base, sinusoidal leading edge wings, and saw-tooth leading edge wings are shown in Figure 3.4, Figure 3.5, and Figure 3.6, respectively. The 'S' and 'ST' notations in the names of the wing models present sinusoidal and saw-tooth leading edges, respectively. The 'λ' symbol denotes the wavelength ratio, while the 'ϕ' symbol represents the amplitude ratio, and the numbers following these symbols indicate decimal values of ratios. The geometrical properties of wing models are given in Table 2.

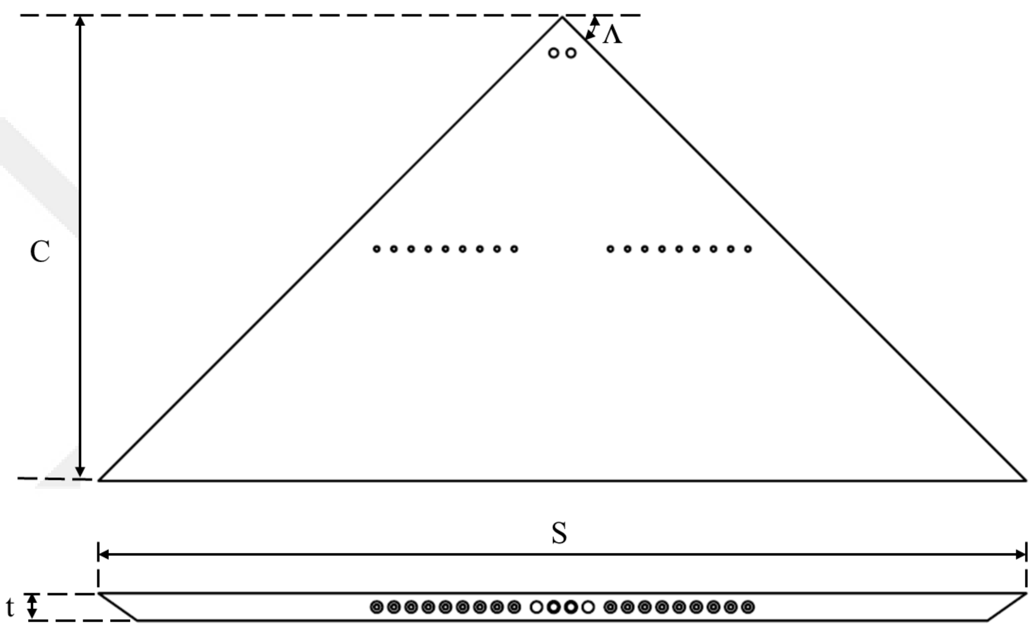

Figure 3.4 Schematic representation of the base wing.

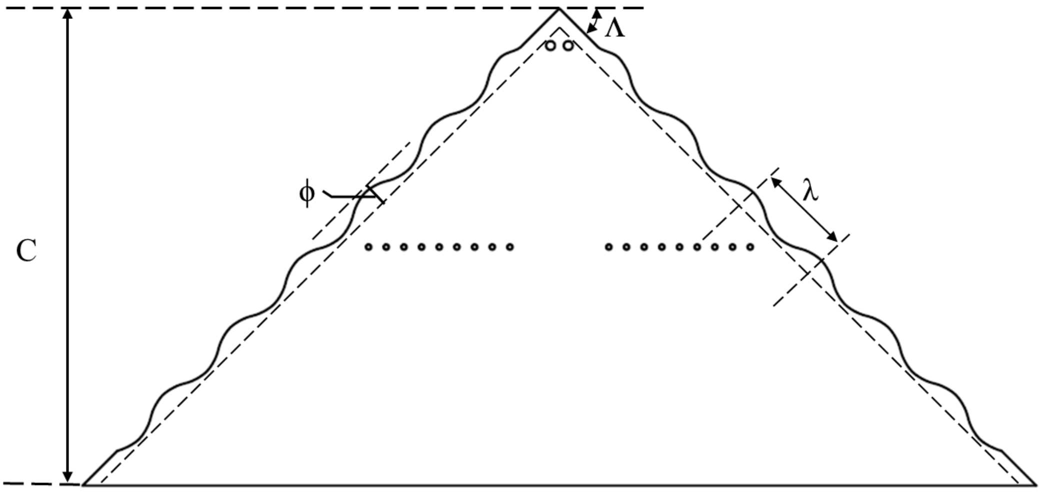

Figure 3.5 Sinusoidal leading-edge wing configurations.

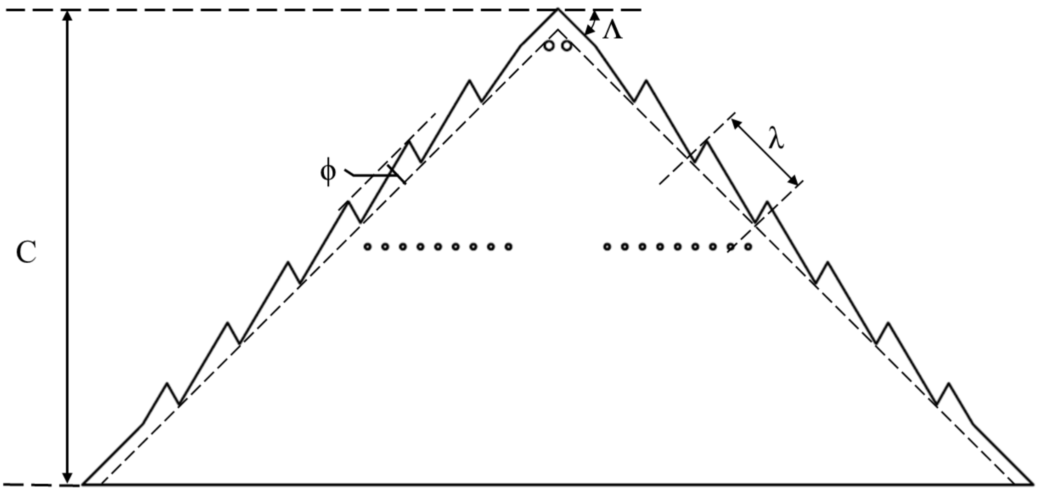

Figure 3.6 Saw-tooth leading-edge wing configurations.

Table 2 Wing properties for sinusoidal and saw-tooth leading-edge models.

Model	**λ/C**	**ϕ/C**
S-λ1ϕ02	0.1	0.02
S-λ2ϕ03	0.2	0.03
S-λ2ϕ05	0.2	0.05
S-λ3ϕ05	0.3	0.05
ST-λ2ϕ03	0.2	0.03
ST-λ2ϕ05	0.2	0.05

3.3 Ground Effect Setup

The static ground effect can be simulated by a ground plane placed beneath the wing model. This ground plane is elevated or lowered with a traverse to mimic different ground clearances. The ability to change the ground clearance by moving the plane rather than the wing model allows the model to be free of the wind tunnel wall boundary layer distortion. To ensure the invariability of the model's height from the ground plane, this height was measured from the bottom of the trailing edge of the wing models for the ground effect.

The ground plane used in the ground effect simulation is made from plexiglass and has dimensions of 540 mm in length, 475 mm in width, and 9 mm in thickness. The leading edge of the ground plate is beveled at 26.25°. The height of the ground plate is manually adjusted via a volant wheel located at the height adjustment part of the rig. The ground plate is connected to the height adjustment part with three push rods. Once the height of the ground plate is adjusted, it remains fixed at its position until further adjustments are made. The schematic representations of the ground effect rig are given in Figure 3.7. The position of the wing relative to the ground plate is shown here.

The effect of the ground plate on the out-of-ground cases was investigated to verify that, at a distance corresponding to $h/C = 116\%$, the configuration with the ground plate exhibits similar aerodynamic coefficients to those of the out-of-ground cases without the ground plate, without changing the position of the wing model. Force and pressure measurements were performed with the ground plate, and the height-to-chord ratio of $h/C = 116\%$ was designated as the out-of-ground effect case. The near-surface PIV measurements were performed in the out-of-ground effect (OGE) condition without the ground plate.

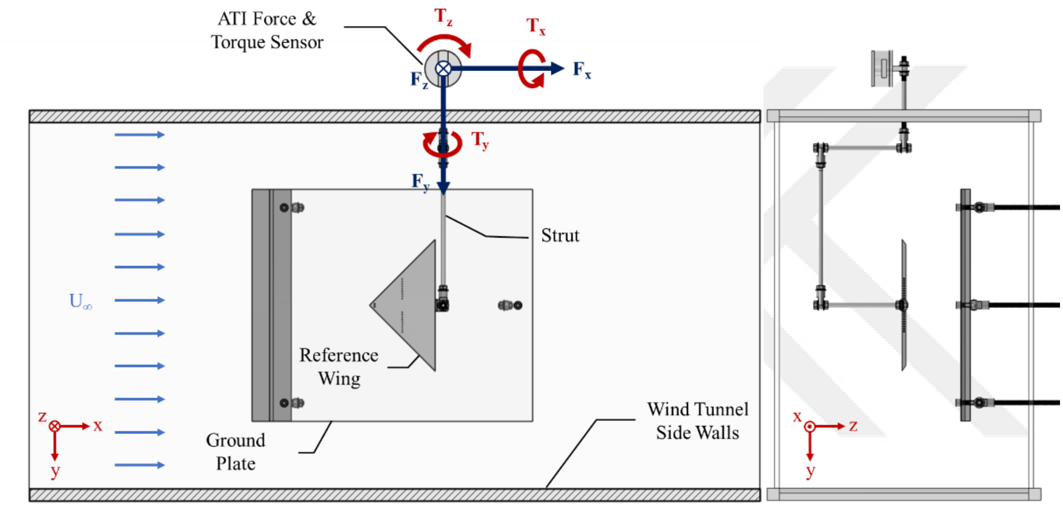

Figure 3.7 Schematic representations of the top and side views of the force measurement setup with the ground effect rig.

3.4 Measurement Techniques

This section describes the measurement techniques used in this study for force, pressure, and near-surface PIV measurements.

3.4.1 Force Measurements

The aerodynamic force measurements were performed using an ATI Gamma Series Force/Torque sensor calibrated according to the SI-32-2.5 scheme. The wind model is attached to the sensor with a strut system. The forces and moments applied to the wing model are transferred by this strut system. The strut is connected to the sensor adaptor, and the sensor is rigidly connected to the model positioning system. The model positioning system is a traverse system that allows users to change the angle of attack and the height of the wind model from the ground plane without affecting the accuracy of the experiments. This system is designed to be used in ground effect experiments without any limitations. A schematic view of the wind tunnel from the top view with the force measurement setup is given in Figure 3.7.

Force measurements are conducted in four steps using the superpositioning technique. These steps are given in Table 3. The first and fourth steps, conducted without wind, measure the gravitational forces. The second and third steps, conducted with wind, measure both the gravitational and the aerodynamic forces. The out-of-ground effect force/moment coefficients calculations source code is presented in Appendix A

Table 3 Configuration and wind status for force measurements and the respective measured forces and moments.

Step	**Configuration**	**Wind Status**	**Forces and Moments Measured**
1	Wing and Strut	Off	Gravitational Forces and Moments of Wing and Strut
2	Wing and Strut	On	Gravitational and Aerodynamic Forces and Moments of Wing and Strut
3	Strut	On	Gravitational and Aerodynamic Forces and Moments of Strut
4	Strut	Off	Gravitational Forces and Moments of Strut

The aerodynamic and gravitational forces and moments of the bare strut are measured for each angle of attack to disregard the effects of the strut system. The gravitational forces and moments of the wing model are also measured using the experimental steps below. The aerodynamic forces and moments applied only to the wind model can be obtained by conducting the following operations.

$$Wing(Gravitational + Aerodynamic) = Step\ 2 - Step\ 3$$

$$Wing\ Gravitational = Step\ 1 - Step\ 4$$

$$Wing\ Aerodynamics = (Step\ 2 - Step\ 3) - (Step\ 1 - Step\ 4)$$

The force measurements are presented in four different plots. In the first plot, the lift coefficient (C_L) is expressed with respect to the angle of attack (α). In the second plot, the drag coefficient (C_D) is expressed with respect to the angle of attack. In the third plot, the pitch moment coefficient (C_M) is expressed with respect to the angle of attack, and in the fourth plot, lift-to-drag ratio (C_L/C_D) is expressed with respect to the angle of attack. These coefficients can be found using the Eqn. 3-3 to 3-6.

$$P_{dyn} = \frac{\rho U_\infty^2}{2} \tag{3-2}$$

$$C_L = \frac{F_L}{P_{dyn}A} \tag{3-3}$$

$$C_D = \frac{F_D}{P_{dyn}A} \tag{3-4}$$

$$C_L/C_D = \frac{F_L}{F_D} \tag{3-5}$$

$$C_M = \frac{M_y}{P_{dyn}AL} \tag{3-6}$$

3.4.1.1 Axis Frames

The force measurement setup has two axis frames: the wind and the body frame. The wind frame is a stationary frame that does not vary with the angle of attack. In contrast, the body frame is positioned on the sensor and rotated with the sensor when the attack angle changes. These axis frames are shown in Figure 3.8. The wind frame is represented in red, the body frame is represented in dark blue, and the angle of attack is represented in green.

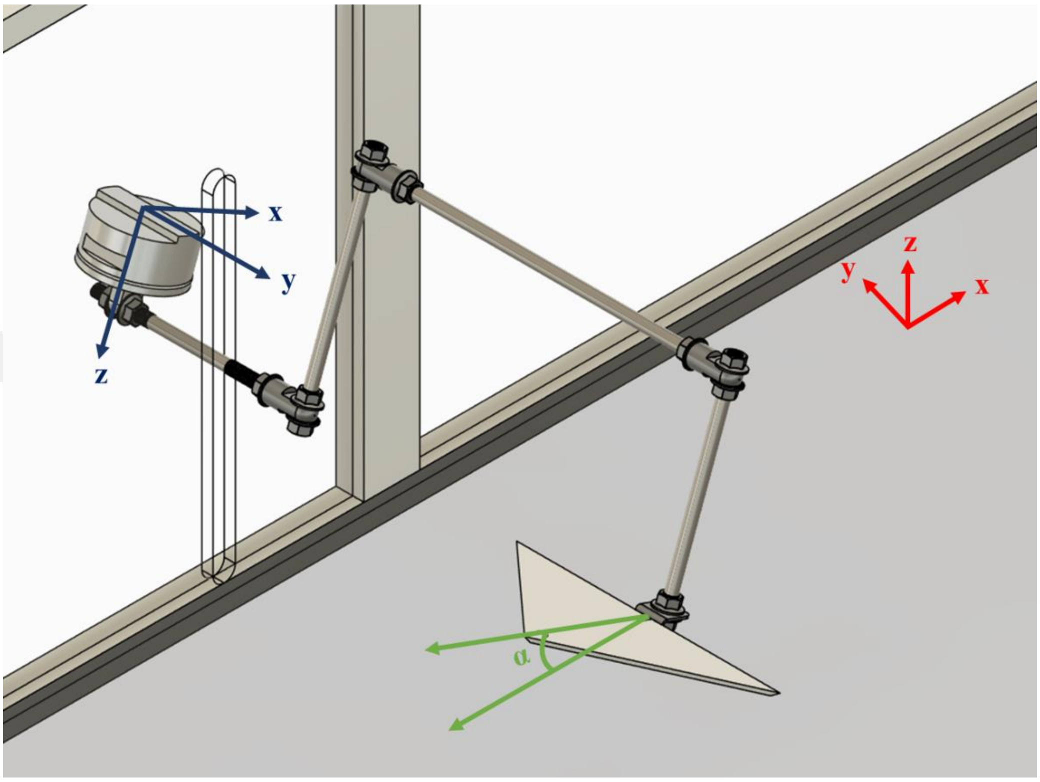

Figure 3.8 Wind frame (red), body frame (dark blue), and angle of attack (green).

The measured loads are measured in the body frame and should be transformed into the wind frame.

$$F_{xw} = +(F_{xb}.\cos(\alpha) - F_{zb}.sin(\alpha)) \quad (3\text{-}7)$$

$$F_{yw} = -(F_{yb}) \quad (3\text{-}8)$$

$$F_{zw} = -(F_{xb}.\sin(\alpha) + F_{zb}.cos(\alpha)) \quad (3\text{-}9)$$

$$M_{xw} = +(M_{xb}.\cos(\alpha) - M_{zb}.\sin(\alpha)) \quad (3\text{-}10)$$

$$M_{yw} = -(M_{yb}) \quad (3\text{-}11)$$

$$M_{zw} = -(M_{xb}.\sin(\alpha) + M_{zb}.cos(\alpha)) \quad (3\text{-}12)$$

In the abovementioned equations, the subscripts b and w represent body and wind frame, respectively. F_{xw}, F_{yw}, F_{zw} represents drag forces, side forces, and lift forces, while M_{xw}, M_{yw}, M_{zw} represents roll, pitch, and yaw moments, respectively.

3.4.2 Surface Pressure Measurements

The surface pressure measurements were conducted on the suction side of all the wing models with a 16-channel Netscanner 9116 Intelligent Pressure Scanner. This scanner is capable of measuring pressures in the range of 0 – 2.5 kPa with 16 piezo-resistive transducers. The manufacturer of the pressure scanner pre-calibrated the device over a predetermined pressure and temperature span. Although the device is pre-calibrated before every experimental run, the scanner is calibrated with the help of a manometer. The resolution of the pressure scanner is $\pm 0.003\%$ FS (full scale), and the scanner's accuracy is $\pm 0.05\%$ FS. The resolution of the pressure scanner is ensured with the microprocessor and temperature sensors, which are integrated into the pressure scanner to compensate for the thermal effects, nonlinearity, sensitivity, and transducer outputs for offset.

Each wing model has 18 pressure channels in total. The pressure data were collected for 10 seconds at a sampling rate of 500 Hz. Before each set of experiments, noise data were collected, which were subtracted from the measured pressure data to obtain refined data. Non-dimensional pressure coefficient C_P was calculated using Eqn. 3-13.

$$C_P = \frac{P - P_{static}}{P_{dyn}} \quad (3\text{-}13)$$

The surface pressure measurement at $h/C = 116\%$ for the base delta wing is shown in Figure 3.9. The out-of-ground effect pressure coefficient calculations source code is presented in Appendix B

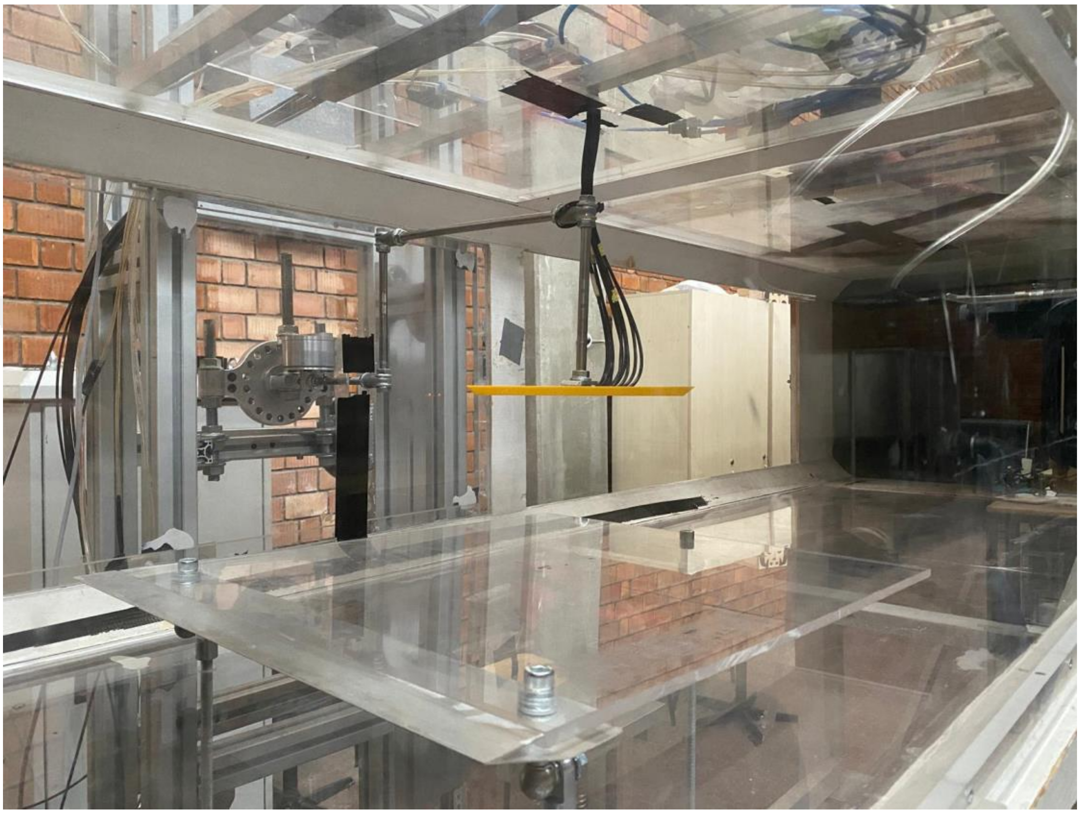

Figure 3.9 Surface pressure measurement at $h/C = 116\%$, for base delta wing.

3.4.3 Particle Image Velocimetry (PIV) Measurements

The principle of particle image velocity (PIV) measurements is to track the movement of particles within a defined area using a laser sheet. PIV is an advanced experimental method that is crucial in comprehending the flow structure. Therefore, in this study, a TSI 2D PIV system was used to study the flow field comprehensively near the surface plane of the delta wing with a near-surface PIV method. Measurements were conducted in out-of-ground effect without the ground effect plate. The schematic representation of the near-surface PIV method Figure 3.10.

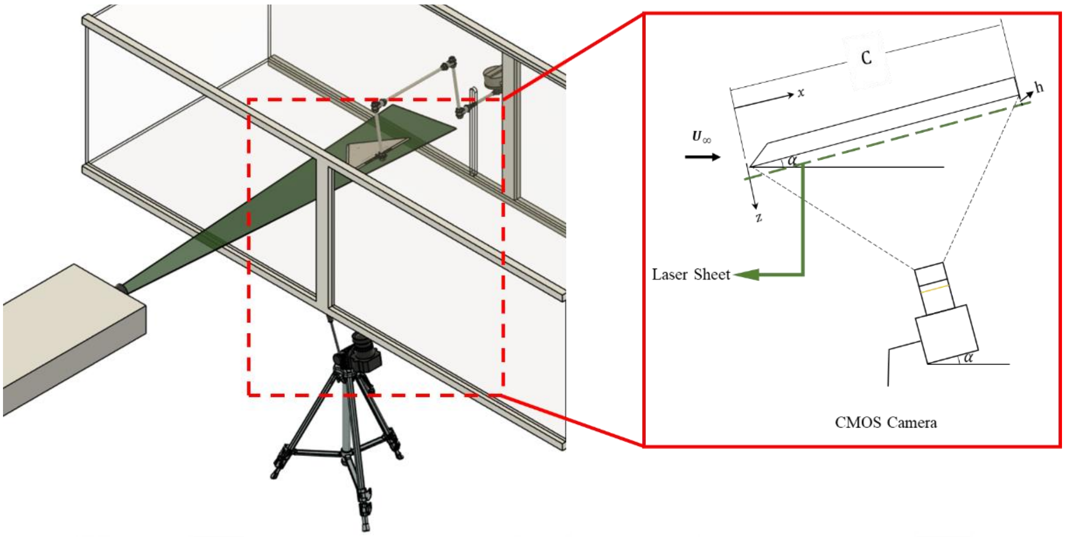

Figure 3.10 Schematic representation of near-surface PIV.

The PIV setup used in this study consists of a Litron Nd: YAG laser, which can generate laser pulses up to 200 mJ with a repetition rate of 15 Hz. The laser sheet for illuminating the flow field is formed with a -25 mm cylindrical lens and a $1000\ mm$ spherical lens. A Powerview Plus 8-bit, digital, CMOS camera with a resolution of $2048\ \times 2048$ pixels, equipped with a Nikon 50mm F/1.8D lens, was utilized for capturing images. Seeding particles were provided to the system by a commercial smoke generator using a glycol-based smoke fluid. Synchronization of the laser and camera was obtained with a TSI LaserPulse 610036 synchronizer.

The Insight 4G software was used to acquire the raw data and process these data. The near–surface PIV measurements were conducted for all the wing models at three different attack angles: $\alpha = 10°, 17°, 22°$. The laser was parallel to the wing at all the angles of attack and was approximately 3 mm from the suction side of the wing models. Near-surface PIV measurements were conducted at a Reynolds number of $Re = 7.5 \times 10^4$ with a pulse separation time of $dT = 50\ \mu s$, 200 image pairs were collected at 15 Hz for each case.

The interrogation area was selected as 32×32 pixels. For each wing model and at each angle of attack, pixels were calibrated accordingly. An accurate calibration of the pixels is necessary for an accurate PIV measurement. In this study, calibration for each angle of attack was performed separately to account for the minor changes in the reference length caused by the necessary variations in the camera position for each angle of attack.

The region of interest was set to 1600×1750 pixels for all wing models at $\alpha = 22°$, and for base, S-λ2ϕ03, and ST-λ2ϕ05 wing models at $\alpha = 17°$. At $\alpha = 10°$, the region of interest was selected as 1700×1820 pixels for all the wing models.

Background subtraction was applied to all the cases to reduce noise and improve the particle visibility. During this preprocessing, an average intensity image generator was used to generate the background image. The generated background image was subtracted from the raw data using an image calculator. The Recursive Nyquist Grid engine was selected as the engine grid with a starting spot dimension of 64×64 pixels to a final spot dimension of 32×32 pixels.

Local validation of vectors was ensured with a median test method having a spatial neighborhood of 5×5, and bad vectors were replaced by the local median. Vector field conditioning was performed using recursive filling with the local mean method and a spatial neighborhood of 5×5, and smoothing was applied after filling holes. Streamlines, velocity contours, and vorticity fields were calculated with the time average of 200 image pairs using Tecplot Focus 2013R1 software.

3.5 Experimental Matrix

In this study, force, pressure, and PIV measurements were conducted, investigating both the out-of-ground effect and the ground effect at various angles of attack and heights. The force, the pressure, and the PIV experiments, IGE, and OGE conditions were conducted with all wing models. The experimental matrix for this study is shown in Figure 3.11.

Figure 3.11 Experimental matrix.

3.6 Uncertainty Estimates

Uncertainties arise in any experimental research due to the inaccuracies of measuring devices such as protractors and sensors. The uncertainty estimates encountered during this experimental study are addressed in this chapter.

$$\omega_R = \left[\left(\omega_{x_1}\frac{\partial R}{\partial x_1}\right)^2 + \left(\omega_{x_2}\frac{\partial R}{\partial x_2}\right)^2 + \cdots + \left(\omega_{x_n}\frac{\partial R}{\partial x_n}\right)^2\right]^{1/2} \tag{3-14}$$

In Eqn. 3-14, ω_{x_i} represents the uncertainty estimate of each measured variable. The relative uncertainty is represented with u_R and is found using Eqn. 3-15.

$$u_R = \frac{\omega_R}{R} \tag{3-15}$$

The relative uncertainty estimates of lift, drag, pitch moment, pressure, and lift-to-drag ratio are calculated individually. These calculations are shown in equations 3-16 to 3-32. The measured absolute uncertainty values of the aerodynamic coefficients measured during experiments are provided in Appendix C

Table 4. The absolute uncertainty levels of force measurements are presented in Appendix C

Table 4 Uncertainty results of force and pressure measurements.

	Wing Models						
	Base	**S-λ1ϕ02**	**S-λ2ϕ03**	**S-λ2ϕ05**	**S-λ3ϕ05**	**ST-λ2ϕ03**	**ST-λ2ϕ05**
$\pm\omega_{C_L}$	0.046	0.050	0.051	0.052	0.052	0.048	0.054
$\pm\omega_{C_D}$	0.073	0.074	0.077	0.076	0.077	0.073	0.078
$\pm\omega_{C_L/C_D}$	1.635	1.915	1.547	1.628	1.689	1.941	1.700
$\pm\omega_{C_M}$	0.028	0.029	0.028	0.029	0.029	0.028	0.028
$\pm\omega_{C_P}$	0.030	0.030	0.030	0.031	0.032	0.031	0.032

3.6.1 Lift Coefficient Uncertainty Calculation

$$F_x = \frac{M_z}{dy} \tag{3-16}$$

$$F_z = \frac{-M_x}{dy} \tag{3-17}$$

$$\omega_{F_x} = \pm\left(\frac{\omega_{M_z}}{dy}\right)^2 \tag{3-18}$$

$$\omega_{F_z} = \pm\left(\frac{\omega_{M_x}}{dy}\right)^2 \tag{3-19}$$

$$C_L = \frac{-(F_x \sin(\alpha) + F_z \cos(\alpha))}{P_{dyn}A} \tag{3-20}$$

$$C_L = C_L(F_x, F_z, \alpha, P_{dyn}, A) \tag{3-21}$$

$$\begin{aligned}\omega_{C_L} = \pm\Bigg[&\left(\omega_{F_x}\left(-\frac{\sin(\alpha)}{P_{dyn}A}\right)\right)^2 + \left(\omega_{F_z}\left(-\frac{\cos(\alpha)}{P_{dyn}A}\right)\right)^2 \\ &+ \left(\omega_\alpha\left(-\frac{\mathrm{F_x}\cos(\alpha) - F_z\sin(\alpha)}{P_{dyn}A}\right)\right)^2 \\ &+ \left(\omega_{P_{dyn}}\left(\frac{\mathrm{F}_z\cos(\alpha) + F_x\sin(\alpha)}{\left(P_{dyn}\right)^2 A}\right)\right)^2 \\ &+ \left(\omega_A\left(\frac{\mathrm{F}_z\cos(\alpha) + F_x\sin(\alpha)}{P_{dyn}A^2}\right)\right)^2\Bigg]^{1/2}\end{aligned} \tag{3-22}$$

3.6.2 Drag Coefficient Uncertainty Calculation

$$C_D = \frac{(F_x \cos(\alpha) - F_z \sin(\alpha))}{P_{dyn} A} \tag{3-23}$$

$$C_D = C_D(M_x, M_z, dy, \alpha, P_{dyn}, A) \tag{3-24}$$

$$\begin{aligned}\omega_{C_D} = \pm \Bigg[& \left(\omega_{F_x}\left(\frac{\cos(\alpha)}{P_{dyn}A}\right)\right)^2 + \left(\omega_{F_z}\left(-\frac{\sin(\alpha)}{P_{dyn}A}\right)\right)^2 \\ & + \left(\omega_{\alpha}\left(-\frac{\mathrm{F_x}\sin(\alpha) + F_z\cos(\alpha)}{P_{dyn}A}\right)\right)^2 \\ & + \left(\omega_{P_{dyn}}\left(-\frac{\mathrm{F}_x\cos(\alpha) - F_z\sin(\alpha)}{\left(P_{dyn}\right)^2 A}\right)\right)^2 \\ & + \left(\omega_{A}\left(-\frac{\mathrm{F}_x\cos(\alpha) + F_z\sin(\alpha)}{P_{dyn}A^2}\right)\right)^2 \Bigg]^{1/2}\end{aligned} \tag{3-25}$$

3.6.3 Lift-to-drag Ratio Uncertainty Calculation

$$C_L/C_D = \frac{-(F_x \sin(\alpha) + F_z \cos(\alpha))}{(F_x \cos(\alpha) - F_z \sin(\alpha))} \tag{3-26}$$

$$\omega_{C_L/C_D} = \pm\left[\left(\omega_{F_x}\left(\frac{F_Z}{(F_X\cos(\alpha) - F_z\sin(\alpha))^2}\right)\right)^2 + \left(\omega_{F_z}\left(-\frac{F_x}{(F_X\cos(\alpha) - F_z\sin(\alpha))^2}\right)\right)^2 + \left(\omega_{\alpha}\left(-\frac{F_x^2 + F_z^2}{(F_X\cos(\alpha) - F_z\sin(\alpha))^2}\right)\right)^2\right]^{1/2} \tag{3-27}$$

3.6.4 Pitch Moment Coefficient Uncertainty Calculation

$$C_M = \frac{M_y}{P_{dyn}AL} \tag{3-28}$$

$$C_M = C_M(M_y, P_{dyn}, A) \tag{3-29}$$

$$\omega_{C_M} = \pm\left[\left(\omega_{M_y}\left(\frac{1}{P_{dyn}AL}\right)\right)^2 + \left(\omega_{P_{dyn}}\left(-\frac{M_y}{\left(P_{dyn}\right)^2 AL}\right)\right)^2 + \left(\omega_{A}\left(-\frac{M_y}{P_{dyn}A^2L}\right)\right)^2 + \left(\omega_{L}\left(-\frac{M_y}{P_{dyn}AL^2}\right)\right)^2\right]^{1/2} \tag{3-30}$$

3.6.5 Pressure Coefficient Uncertainty Calculation

$$C_P = \frac{P - P_{static}}{P_{total} - P_{static}} \tag{3-31}$$

$$C_P = C_P(P, P_{static}, P_{total}) \tag{3-32}$$

$$\omega_{C_p} = \pm\left[\left(\omega_P\left(-\frac{1}{P_{static} - P_{total}}\right)\right)^2 + \left(\omega_{P_{static}}\left(\frac{P - P_{total}}{(P_{static} - P_{total})^2}\right)\right)^2 + \left(\omega_{P_{total}}\left(-\frac{P - P_{static}}{(P_{static} - P_{total})^2}\right)\right)^2\right]^{1/2} \tag{3-33}$$

CHAPTER 4

RESULTS AND DISCUSSIONS

This chapter provides the results of the study in three parts. First, the force measurement results for the out-of-ground effect and the in-ground effect results are reported. Then, pressure measurement results are reportedFinally, near-surface PIV results for out-of-ground effect results are presented.

4.1 Force Measurement Results

Force measurements were conducted in four different height-to-chord ($h/C(\%)$) ratios: 16%, 27%, 50%, and 116%. The results of force measurements are shown in this chapter.

4.1.1 Out-of-Ground Effect

The results of force measurements conducted in out-of-ground effect, at $h/C = 116\%$, are provided in this chapter. The results of the force measurements are presented as distributions of dimensionless coefficients with respect to the angle of attack. In Figure 4.1, the drag coefficient (C_D), lift coefficient (C_L), moment coefficient at the trailing edge ($C_{M\ at\ TE}$), and the lift-to-drag ratio (C_L/C_D) at various angles of attack for the base wing, S-λ2ϕ03, S-λ2ϕ05, and ST-λ2ϕ05 wing models are shown. The moment coefficient was drawn from the trailing edge in order to amplify the effects of the leading-edge modifications.

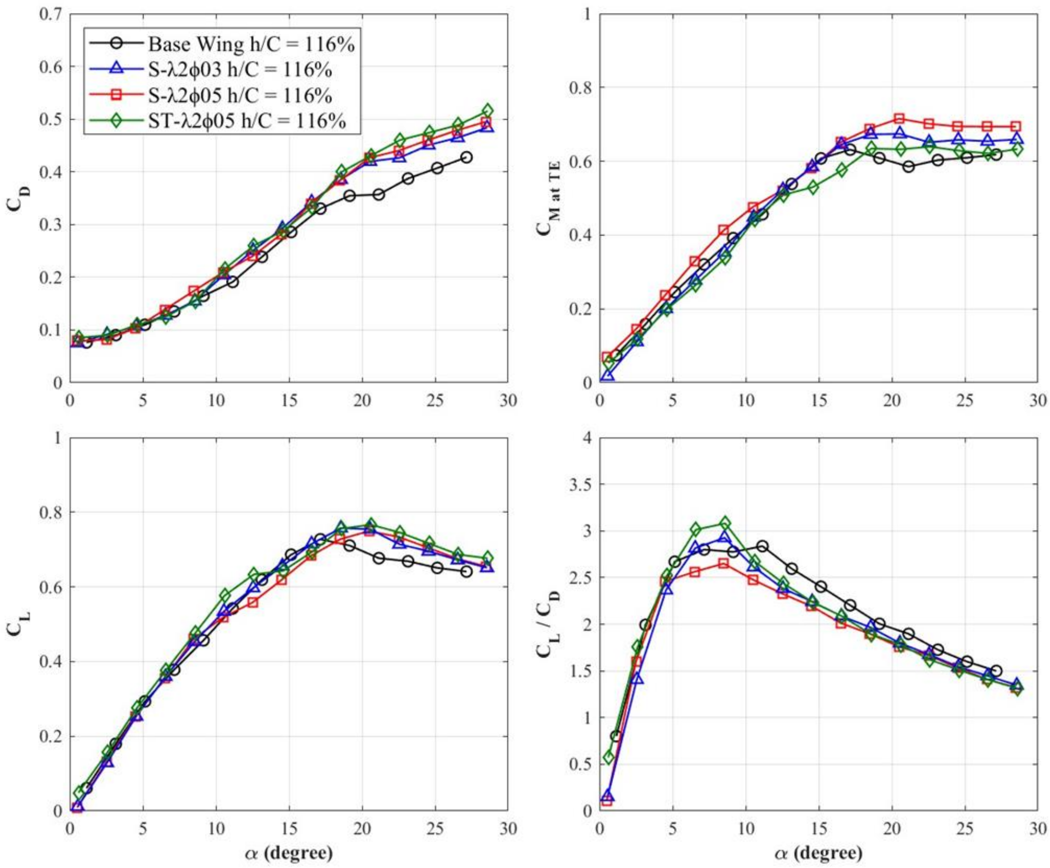

Figure 4.1 Drag coefficient (C_D), lift coefficient (C_L), moment coefficient (C_M), and the lift-to-drag ratio (C_L/C_D) at $h/C = 116\%$ with various angles of attack for different wing models.

The drag coefficient in the upper left plot of Figure 4.1 shows only a slight difference among the wing models at the lower angles of attack. The rate of change of drag coefficient is similar for all the wing models until the angle of attack reaches $\alpha = 17°$. As the angle of attack exceeds $\alpha = 17°$, the rate of change of drag coefficient decreases for all the wing models. However, the corresponding rate of change for the base wing model decreases more significantly than that of the modified wing models. Among the modified wing models, the S-λ2ϕ03 model indicates the greatest decrease, while the ST-λ2ϕ05 model shows the least decrease in the rate of change.

Considering the lift coefficient distribution, as shown in the lower left plot of Figure 4.1, increases in the stall angle and the maximum lift coefficient ($C_{L\,max}$) value for the modified wings are evident. The base wing model shows stall characteristics around $\alpha = 17°$ with a $C_{L\,max} = 0.73$. Among the modified wings, the S-λ2ϕ05 and ST-λ2ϕ05 models demonstrated the best stall-delaying abilities, both stalling around $\alpha = 21°$. S-λ2ϕ05 model had a $C_{L\,max} = 0.75$ and the ST-λ2ϕ05 model had a $C_{L\,max} = 0.77$. The S-λ2ϕ03 model stalled around $\alpha = 19°$ with a $C_{L\,max} = 0.76$. The decrease in the lift coefficient post-stall of the modified wing models was not as drastic as the base wing model, showing smoother stall characteristics. A smoother stall behavior and higher stall angles increase the range of angle of attack at which maneuverability is enhanced [62]. Moreover, there is an increase in the lift coefficient of the modified wing models compared to the base wing post-stall. The rate of change of the lift coefficient is similar for all the wing models until $\alpha = 9°$. The ST-λ2ϕ05 wing model shows a higher rate of change of lift coefficient between the angles of attack of 9° and 13°. In contrast, the rate of change decreases for the S-λ2ϕ05 wing model between the angles of attack of 9° and 13°. As the angle of attack exceeds $\alpha = 13°$ the rate of change is similar for all the wing models until their corresponding stall angle. The stall angles and maximum lift coefficient values of each wing model are given in Table 5.

For further discussion of the drag and lift coefficients for modified wings, it is important to note that the S-λ3ϕ05 and S-λ2ϕ05 wing models share the same amplitude ratio of $\phi/\mathrm{C} = 0.05$ and have wavelength ratios of $\lambda/\mathrm{C} = 0.3$ and $\lambda/\mathrm{C} = 0.2$, respectively. As the angle of attack exceeds $\alpha = 21°$ an increase in the drag coefficient is present in the wing model with the lower wavelength ratio. The wing model with a higher wavelength ratio showed higher lift coefficient values when the angle of attack is between $\alpha = 11°$ and $\alpha = 21°$. No significant effect of the wavelength ratio was observed at other angles of attack. In addition, S-λ2ϕ03 and S-λ2ϕ05 wing models share the same wavelength ratio of $\lambda/\mathrm{C} = 0.2$ and have amplitude ratios of $\phi/\mathrm{C} = 0.03$ and $\phi/\mathrm{C} = 0.05$ respectively. As the angle of attack surpasses $\alpha = 21°$ an increase in the drag coefficient is present in the wing model with the higher amplitude ratio. The wing model with a higher amplitude ratio showed lower lift coefficient values when the angle of attack is between $\alpha = 11°$ and $\alpha = 21°$. No significant effect of the amplitude ratio was observed in other angles of attack.

Table 5 Maximum lift coefficient and stall angle at $h/C = 116\%$ for all wing models.

Model	λ/C	ϕ/C	$C_{L\ max\ 116\%}$	α_{stall}
Base	∞	0	0.73	17°
S-λ1ϕ02	0.1	0.02	0.74	18°
S-λ2ϕ03	0.2	0.03	0.76	19°
S-λ2ϕ05	0.2	0.05	0.75	21°
S-λ3ϕ05	0.3	0.05	0.76	20°
ST-λ2ϕ03	0.2	0.03	0.72	19°
ST-λ2ϕ05	0.2	0.05	0.77	21°

Considering the moment coefficient at the trailing edge, as shown in the upper right plot of Figure 4.1, a similar positive slope for wing models at the lower angles of attack is witnessed. The S-λ2ϕ05 wing model shows higher slope values between the angles of attack of $5°$ and $11°$ compared to the other wing models. As the angle of attack exceeds $\alpha = 13°$ the slope of the ST-λ2ϕ05 model decreases while the slopes of other wing models remain unchanged until $\alpha = 17°$. The slope of the base wing model becomes negative when the angle of attack past $\alpha = 17°$. In contrast, the slopes of the modified wing models remained positive until approximately $\alpha = 21°$. Even when the slope of the modified wing models becomes negative, the slope does not decrease drastically compared to the base wing. Modified wing models showed near neutral stability past $\alpha = 21°$ while the base wing model demonstrated interchanging stability around $\alpha = 21°$. Considering post-stall characteristics of the drag and lift coefficients, higher linearity is observed for both coefficients for modified wings compared to the base wing, in return contributing smoother stability characteristics, whereas the base wing exhibits interchanging stability characteristics after stall. The angle range aforementioned in lift coefficient results, where maneuverability is enhanced, coincides with the moment coefficient results.

The lift-to-drag ratio, (C_L/C_D) is a key indicator of the aerodynamic performance of a wing model. This ratio is displayed in the lower right plot of Figure 4.1. The lift-to-drag ratio remains similar for all the wing models until the angles of attack of $\alpha =$ 5°. Between $\alpha = 5°$ and $\alpha = 9°$, the ST-λ2ϕ05 and S-λ2ϕ03 models demonstrate better aerodynamic performance, making them more suitable for cruise conditions. Moreover, all modified wing models reach their maximum lift-to-drag ratio at lower angles of attack compared to the base wing, further enhancing their desirability for cruise conditions. However, the base wing model outperforms the modified wing models for angles of attack greater than $\alpha = 9°$. The peak value of the lift-to-drag ratio was observed at lower angles of attack for modified wing models, showing more desired conditions for cruise conditions.

These observations regarding the stall-delaying capabilities of the bio-inspired wing models were in line with those in the works of Chen et al. [58] and Ramakrishna et al. [2]. Moreover, the sinusoidal leading-edge on airfoils by Miklosovic et al. [15], Post et al. [14], Câmara et al. [80], and Moscato et al. [17] showed similar stall-delaying capabilities. The increase in the drag and lift coefficients witnessed in this study for the bio-inspired wing modifications at post-stall of the base wing aligns with the findings of the delta wing studies by Chen et al. [58] and airfoil studies by Post et al. [14], Moscato et al. [17], Ntantis et al. [65] and Liu et al. [81]. Post et al. [14], Johari et al. [50], Hansen et al. [61], Miklosovic et al. [15, 82].

However, some airfoil studies conducted by Johari et al. [50] and Guerreiro et al. [60] indicated a lower lift prior to the base wing’s stall angle, which might be due to the differences in wavelengths and Reynolds numbers used in these studies.

4.1.2 In-Ground Effect

Results of force measurements conducted in out-of-ground effect, at $h/C = 50\%, 27\%, 16\%$ within an angle of attack range of $-4°$ to $30°$ are provided in this chapter. The results of the force measurements are presented with distributions of dimensionless coefficients with respect to the angle of attack. In Figure 4.2, the drag coefficient (C_D), lift coefficient (C_L), moment coefficient at the trailing edge ($C_{M\ at\ TE}$), and the lift-to-drag ratio (C_L/C_D) at various angles of attack for the base wing, S-λ2ϕ03, S-λ2ϕ05, and ST-λ2ϕ05 wing models at $h/C = 16\%$ are shown.

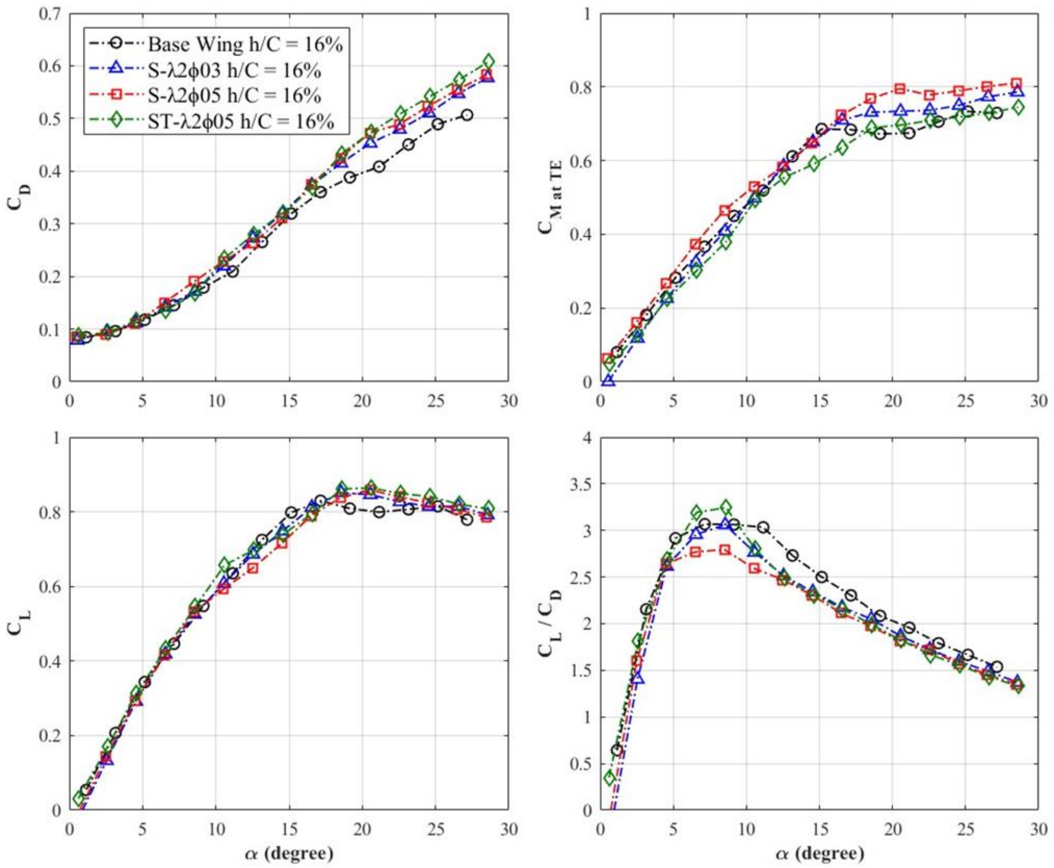

Figure 4.2 Drag coefficient (C_D), lift coefficient (C_L), moment coefficient (C_M), and the lift-to-drag ratio (C_L/C_D) at $h/C = 16\%$ with various angles of attack for different wing models.

The drag coefficient in the upper left plot of Figure 4.2 shows a similar trend to the drag coefficient results at the $h/C = 116\%$. Here, the drag coefficient is similar at the lower angles of attack. As the angle of attack surpasses $\alpha = 17°$, the rate of change of drag coefficient decreases for all the wing models, similar to out-of-ground effect. In higher angles of attack, modified wings show higher drag than the base wing. The lift coefficient of the modified wing models shows similar trends compared to the base wing model throughout the angle of attack range. Between $\alpha = 17°$ and $\alpha = 25°$, the base wing shows a slight decrease in the lift coefficient compared to the modified wings. However, the decrease is not as drastic as the $h/C = 116\%$ results.

By comparing the lift-to-drag ratios values displayed in the lower right plot of Figure 4.1 and Figure 4.2, a difference in the rate of increase in the lift-to-drag ratio between the wing models can be witnessed. The maximum lift-to-drag ratio values for all the wing models, and the angles for the maximum lift-to-drag ratio points at $h/C = 116\%$ and $h/C = 16\%$ are given in Table 6. The maximum lift-to-drag ratio increased from $C_L/C_{D_{max\,116\%}} = 2.84$ to $C_L/C_{D_{max\,16\%}} = 3.07$ for the base wing model with an increase rate of ~8%. While the highest increase rate among the modified wings was observed in the S-λ3ϕ05 wing model, with an increase rate of ~10%. Moreover, the angle of attack at which the maximum lift-to-drag ratio $(C_L/C_{D_{max}})$ value was observed, this angle only varied with different ground clearances for the base and S-λ1ϕ02 wing models. The base wing model showed the maximum lift-to-drag ratio at $\alpha_{116\%} = 11°$ at $h/C = 116\%$, and at $\alpha_{16\%} = 7°$ at $h/C = 16\%$, while the λ1ϕ02 wing model showed it at $\alpha_{116\%} = 8°$ at $h/C = 116\%$, and at $\alpha_{16\%} = 6°$ at $h/C = 16\%$.

Table 6 Maximum lift-to-drag ratio values, and their corresponding angles of attack at $h/C = 116\%$ and $h/C = 16\%$ for various wing models.

Model	λ/C	ϕ/C	$C_L/C_{D\ max\ 116\%}$	$C_L/C_{D\ max\ 16\%}$	$\alpha_{116\%}$	$\alpha_{16\%}$	Increase Rate (%)
Base	∞	0	2.84	3.07	11°	7°	~8%
S-λ1ϕ02	0.1	0.02	2.58	2.73	8°	6°	~6%
S-λ2ϕ03	0.2	0.03	2.93	3.06	9°	9°	~5%
S-λ2ϕ05	0.2	0.05	2.65	2.79	9°	9°	~5%
S-λ3ϕ05	0.3	0.05	2.60	2.87	8°	8°	~10%
ST-λ2ϕ03	0.2	0.03	3.02	3.23	7°	7°	~7%
ST-λ2ϕ05	0.2	0.05	3.01	3.24	9°	9°	~8%

The force measurement results of the base wing model at various ground clearances are given in Figure 4.3. The drag coefficient in the upper left plot shows that the rate of change of drag coefficient is similar for angles of attack below $\alpha = 11°$. However, when the angle of attack exceeds $\alpha = 11°$, the rate of change increases as the ground clearance decreases, resulting in higher drag coefficients at higher angles of attack for wings positioned closer to the ground.

The lift coefficient, shown in the lower left plot of Figure 4.3, indicates that the stall angle stayed the same as the ground clearances varied. As the ground clearance decreased the maximum lift coefficient ($C_{L\,max}$) increased from $C_{L\,\max 116\%} = 0.73$ to $C_{L\,\max 16\%} = 0.83$ increasing around 14%. The base wing model showed smoother post-stall characteristics when the ground clearance was minimum, having less decrease in lift as the angle of attack exceeded $\alpha = 17°$. Base wing's lift coefficient at $h/C = 116\%$ decreased $\Delta C_{L\,116\%} = 0.086$ between angles of attack $\alpha = 17°$ and $\alpha = 25°$, whereas at $h/C = 16\%$, the decrease in the lift coefficient was only $\Delta C_{L\,16\%} = 0.051$.

Considering the moment coefficient at the trailing edge, as shown in the upper right plot of Figure 4.3, for all the ground clearances, the slope remains positive up to $\alpha = 15°$, and the base wing model shows lower stability as the ground clearance decreases. However, beyond this attack angle, the base wing exhibits interchanging stability characteristics at different ground clearances. At $h/C = 116\%$ and $h/C = 50\%$ the slope of the base wing remains positive up to $\alpha = 17°$, whereas at $h/C = 27\%$ and $h/C = 16\%$ the base wing shows near neutral stability. As the angle of attack exceeds $\alpha = 21°$, the base wing model exhibits a positive slope at $h/C = 116\%$ and $h/C = 50\%$, and interchanging stability characteristics for $h/C = 27\%$ and $h/C = 16\%$.

The lift-to-drag ratio, shows similar values for $h/C = 116\%$ and $h/C = 50\%$ cases. The in-ground effect cases, $h/C = 50\%$, $h/C = 27\%$, and $h/C = 16\%$, shows slightly deteriorated aerodynamic performance below $\alpha = 3°$. Between $\alpha = 3°$ and $\alpha = 11°$, the cases with height-to-chord ratios $h/C = 27\%$ and $h/C = 16\%$ shows better aerodynamic performance. The aerodynamic performance of different ground clearances is similar for angles of attack past $\alpha = 11°$.

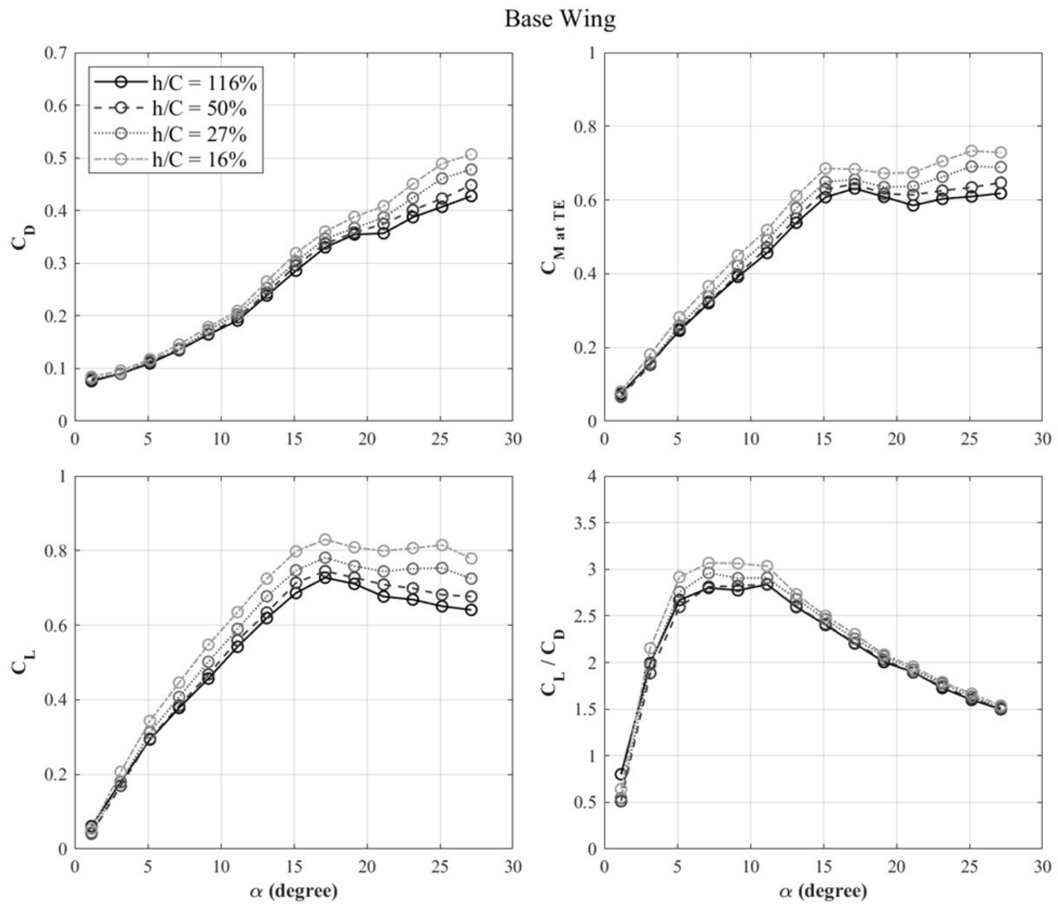

Figure 4.3 Drag coefficient (C_D), lift coefficient (C_L), moment coefficient (C_M), and the lift-to-drag ratio (C_L/C_D) at various ground clearances and angles of attack for base wing model.

The force measurement results of the S-λ2ϕ03, S-λ2ϕ05, and ST-λ2ϕ05 wing models at various ground clearances are given in Figure 4.4, Figure 4.5, and Figure 4.6. The modified wing models exhibit a drag, lift, and moment coefficient trend like that of the base wing model. When the angles of attack exceed $\alpha = 11°$, the minimum ground clearance shows greater drag magnitudes for all wing models. As the ground clearance decreases, the maximum lift coefficient ($C_{L\,max}$) increases for all the modified wing models. However, the increase rate was not the same for all the wing models; the maximum lift coefficient values and the percentage increase are given in Table 7.

The highest increase rate in the maximum lift coefficient was observed in S-λ1ϕ02 and ST-λ2ϕ03 wing models, with a 16% increase rate each. However, the S-λ3ϕ05 wing model performed with the maximum lift coefficient at $\mathrm{h/C} = 16\%$ with a value of $C_{L\,\max 16\%} = 0.87$. Even though the rate of increase in the maximum lift coefficient of the S-λ3ϕ05 wing model was not the highest, about 14%, this wing model exhibited the highest maximum lift coefficient among all wing models at $\mathrm{h/C} = 16\%$.

Table 7 Maximum lift coefficient ($C_{L\,max}$) of base and modified wing models at $h/C = 116\%$ and $h/C = 16\%$.

Model	**λ/C**	**ϕ/C**	**$C_{L\ max\ 116\%}$**	**$C_{L\ max\ 16\%}$**	**Increase Rate (%)**
Base	∞	0	0.73	0.83	~14%
S-λ1ϕ02	0.1	0.02	0.74	0.85	~16%
S-λ2ϕ03	0.2	0.03	0.76	0.85	~12%
S-λ2ϕ05	0.2	0.05	0.75	0.86	~15%
S-λ3ϕ05	0.3	0.05	0.76	0.87	~14%
ST-λ2ϕ03	0.2	0.03	0.72	0.83	~16%
ST-λ2ϕ05	0.2	0.05	0.77	0.86	~13%

The remaining ground effect force measurement results are presented in Appendix D

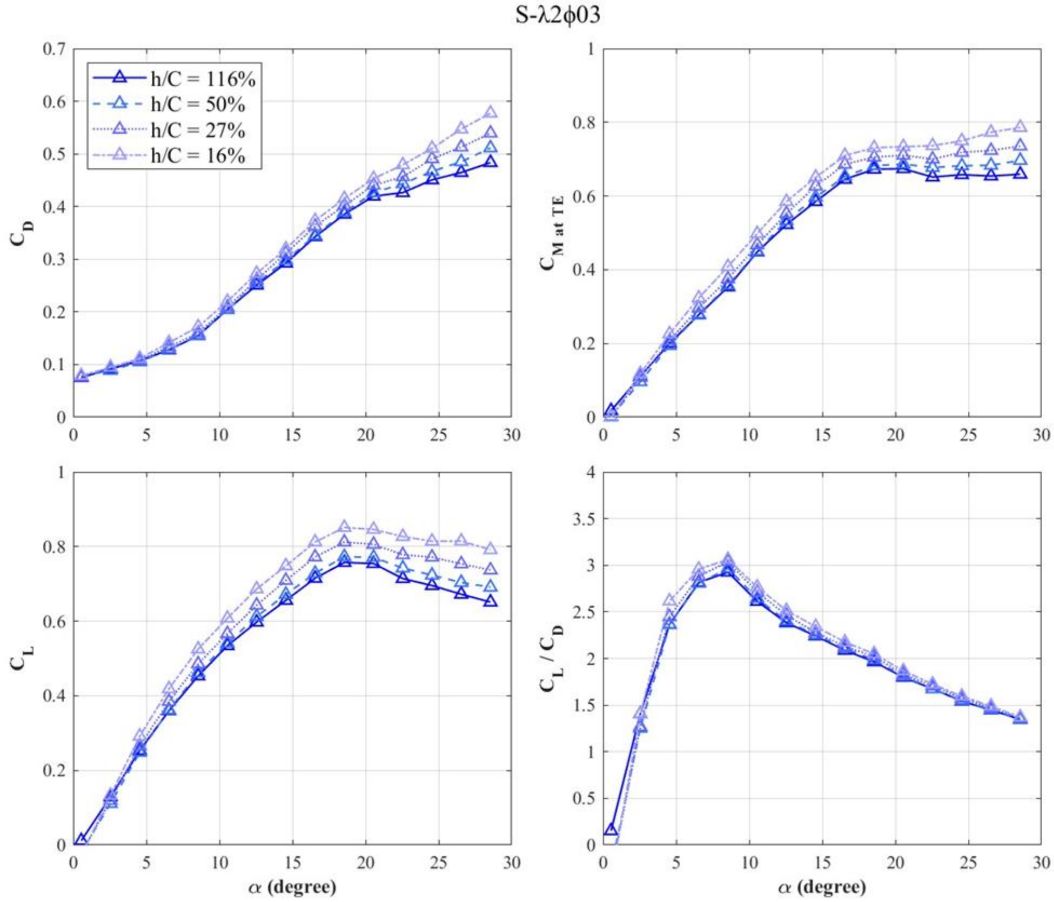

Figure 4.4 Drag coefficient (C_D), lift coefficient (C_L), moment coefficient (C_M), and the lift-to-drag ratio (C_L/C_D) at various ground clearances and angles of attack for S-λ2ϕ03 wing model.

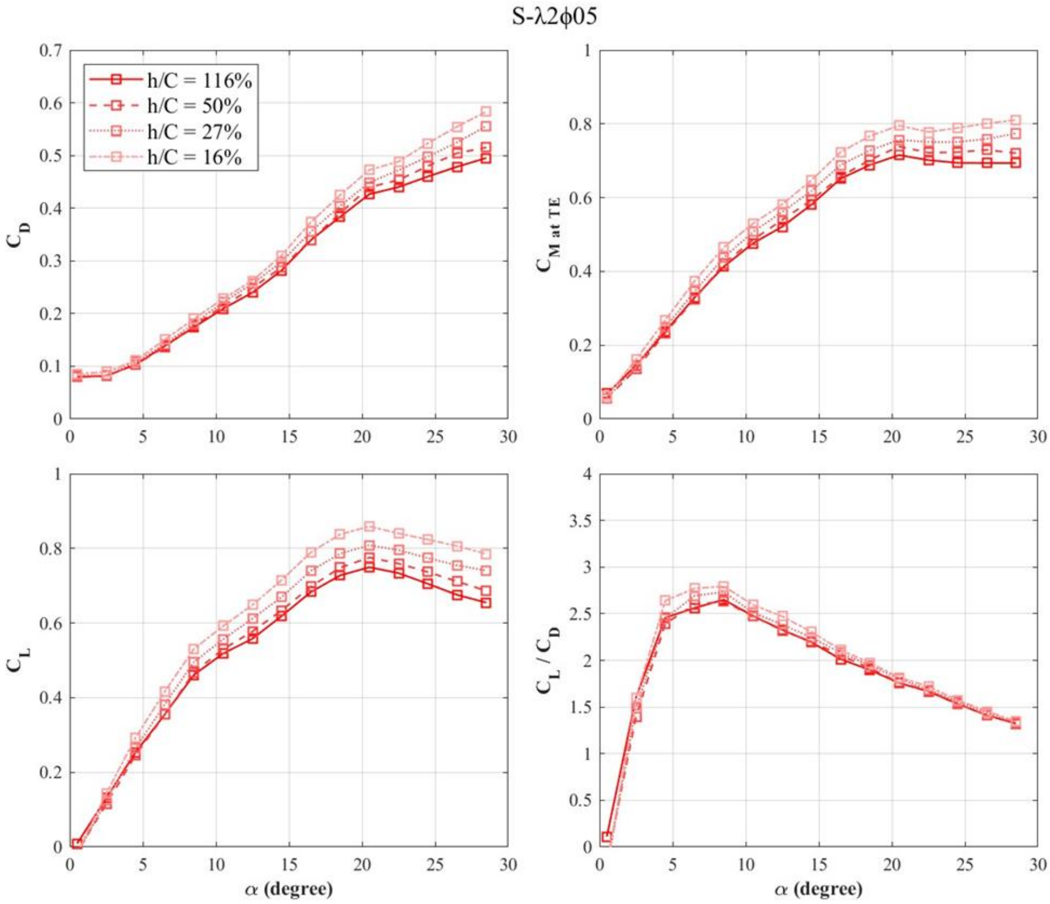

Figure 4.5 Drag coefficient (C_D), lift coefficient (C_L), moment coefficient (C_M), and the lift-to-drag ratio (C_L/C_D) at various ground clearances and angles of attack for S-λ2ϕ05 wing model.

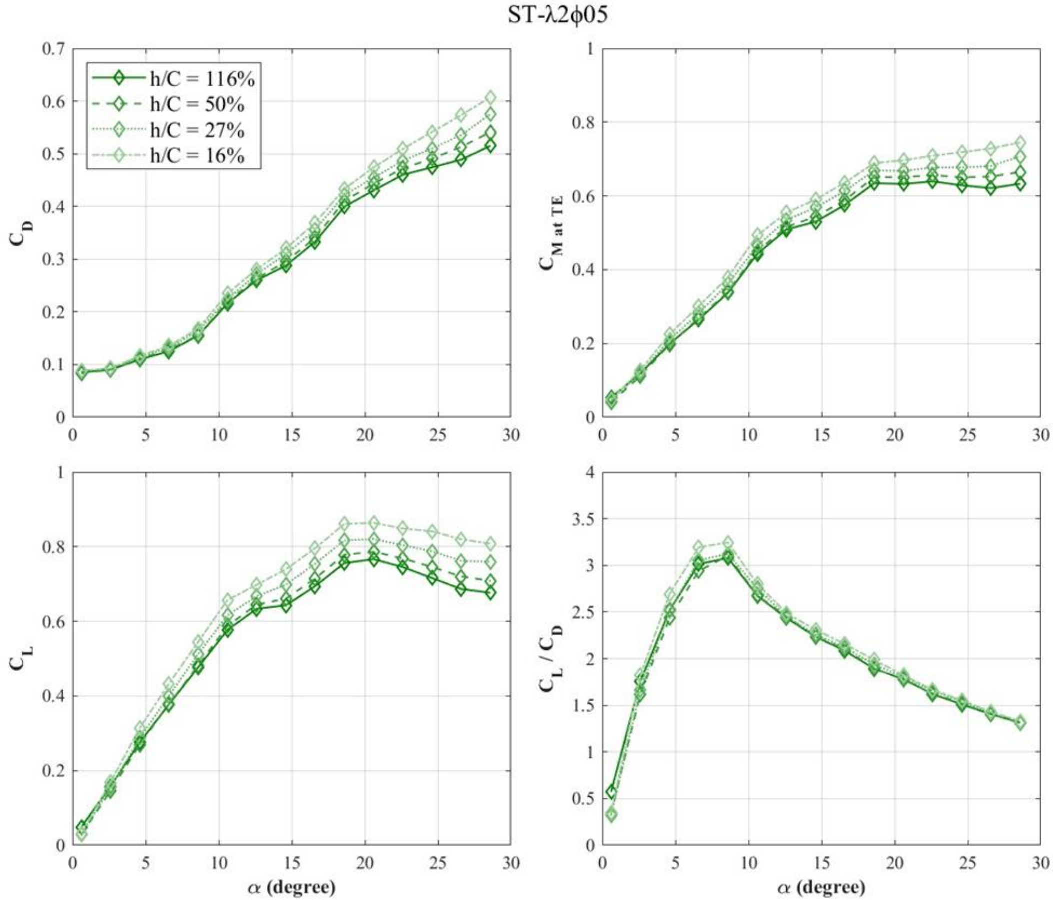

Figure 4.6 Drag coefficient (C_D), lift coefficient (C_L), moment coefficient (C_M), and the lift-to-drag ratio (C_L/C_D) at various ground clearances and angles of attack for ST-λ2ϕ05 wing model.

4.2 Surface Pressure Measurement Results

Pressure measurements were conducted in four different height-to-chord ($h/C(\%)$) ratios: 16%, 27%, 50%, and 116%. The results of pressure measurements are shown in this chapter.

4.2.1 Out-of-Ground Effect

The results of the surface pressure measurements conducted in out-of-ground effect, at $h/C = 116\%$, are presented in Figure 4.7 with distributions of negative pressure coefficient ($-C_p$) for the base wing, S-λ2ϕ03, S-λ2ϕ05, and ST-λ2ϕ05 wing models at various angles of attack with respect to the spanwise distance (y/s), where s is the half-span at the chordwise location $x/C = 0.5$. The magnitude of the $-C_p$ values indicates the strength of the suction; as the $-C_p$ value increases, the strength of the suction increases. A higher suction strength contributes to the lift force.

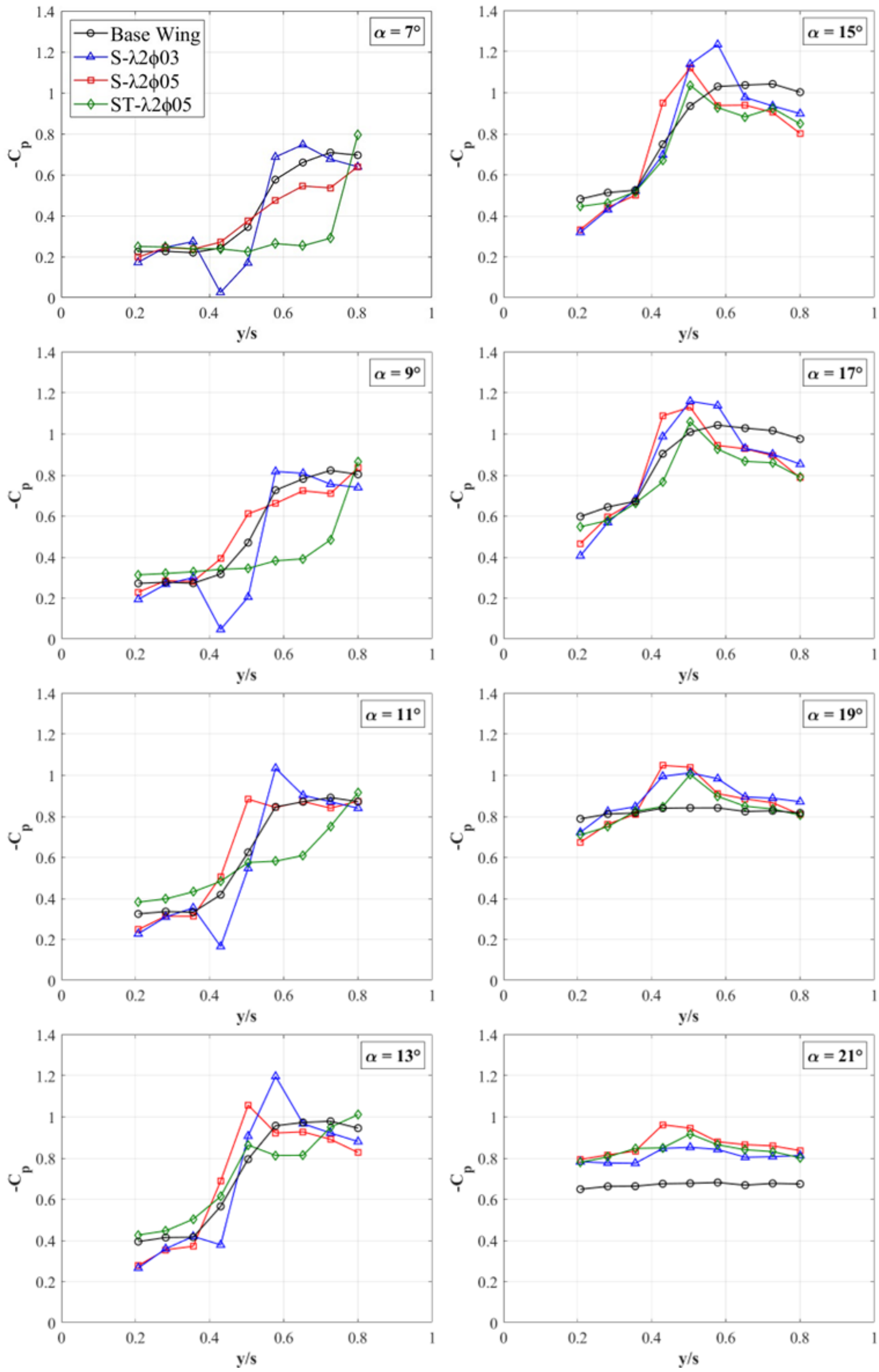

Figure 4.7 Distribution of pressure coefficient at various angles of attack for different wing models on half span at $x/C = 0.5$.

At low angles of attack, there is a typical s-shaped $-C_p$ distribution for the base wing, S-λ2ϕ03, and S-λ2ϕ05 models, indicating the presence of a leading-edge vortex and its footprint on the wing surface. However, the ST-λ2ϕ05 wing model exhibits a different behavior, such that the pressure coefficient is generally constant except for the regions very close to the leading edge. The lift coefficient results of this wing were higher than other wing models at $\alpha = 11°$, while it shows the worst $-C_p$ distribution at this angle of attack. This might indicate a strong leading-edge vortex present inward of the delta wing, providing higher lift compared to other wing models.

As the angle of attack increases from $\alpha = 7°$ to $\alpha = 9°$ the suction pressure peak shifts slightly inboard for the S-λ2ϕ03 wing model. For the S-λ2ϕ05 wing model, the suction peak moves more noticeably as the angle of attack increases from $\alpha = 7°$ to $\alpha = 11°$. In contrast, the suction peak of the ST-λ2ϕ05 wing model remains largely stationary until just before $\alpha = 15°$. For the base wing model, the suction peak does not experience significant movements until approximately $\alpha = 19°$.

The maximum suction pressure of the modified wing models increases up to approximately $\alpha = 17°$. Further increases in the angle of attack result in a decrease in suction pressure. Around $\alpha = 19°$ the pressure distribution for the base wing model levels off, indicating the onset of stall, due to the three-dimensional surface separation. In contrast, the modified wing models do not completely flatten out the pressure distribution even at $\alpha = 21°$, indicating that the flow has not fully separated from the wing surface. The magnitudes of the $-C_p$ values are significantly higher for modified wing models, indicating stronger suction pressure and, consequently, higher lift.

Figure 4.8 presents the distribution of pressure coefficients for the base, S-λ2ϕ03, S-λ2ϕ05, and ST-λ2ϕ05 wing models at the three angles of attack closest to the stall angles identified from the force measurements of each respective wing model, along with the comparison of their lift coefficients. The indications of delayed stall onset from the force measurements are consistent with those observed from the surface pressure measurements.

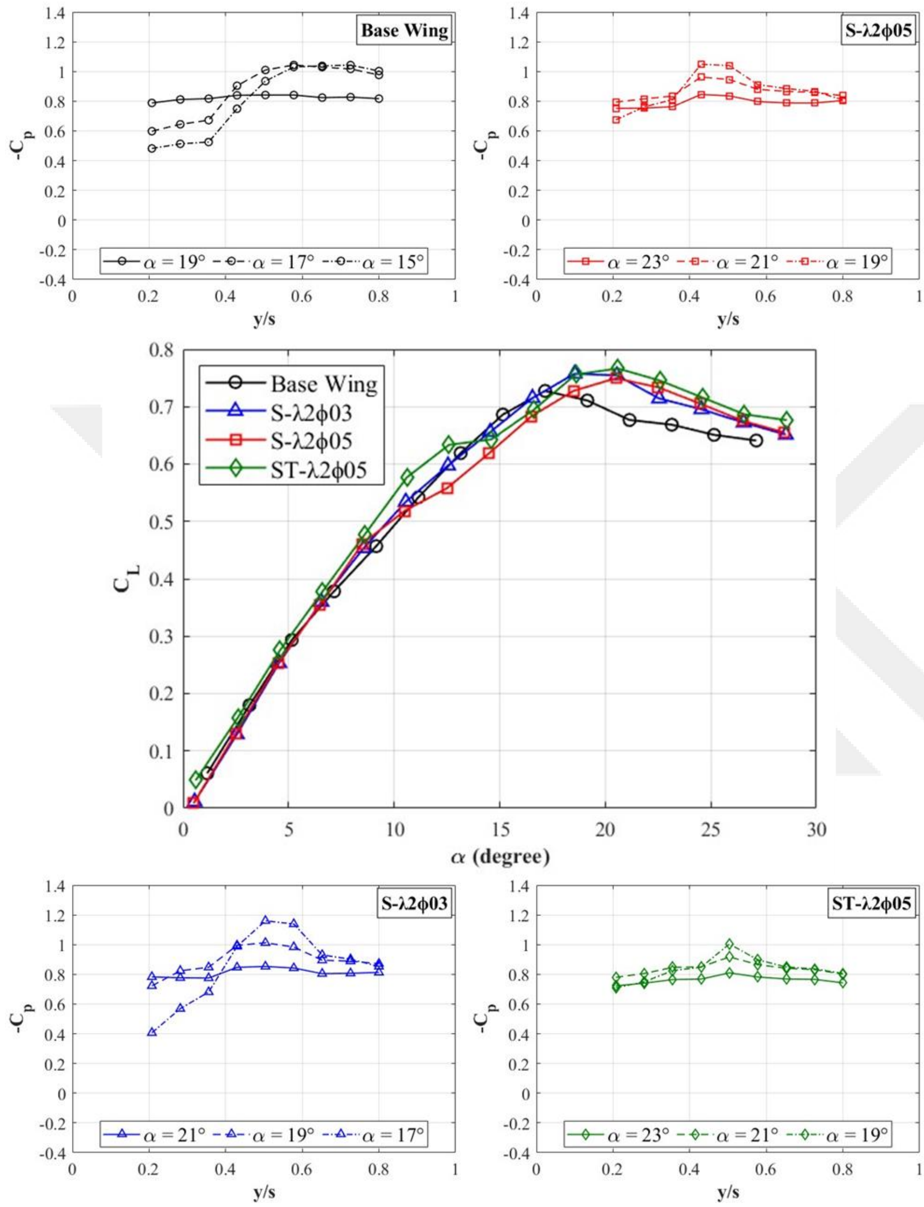

Figure 4.8 Distribution of pressure coefficient at various angles of attack, along with the lift coefficient comparison for different wing configurations.

4.2.2 In-Ground Effect

The results of the surface pressure measurements conducted in ground effect, at $h/C = 16\%$, $h/C = 27\%$, $h/C = 50\%$ and $h/C = 116\%$, are presented in Figure 4.7 with distributions of negative pressure coefficient ($-C_p$) for the base wing, S-λ2ϕ03, S-λ2ϕ05, and ST-λ2ϕ05 wing models at various angles of attack at the chordwise location $x/C = 0.5$.

While there is an increase in the maximum suction pressure of the wing models in some cases as the ground clearance decreases, no significant effect of the ground on the maximum suction pressure was observed. No significant shift was observed in the location of the suction pressure peak as the ground clearance changed. The remaining ground effect pressure measurement results are presented in Appendix D

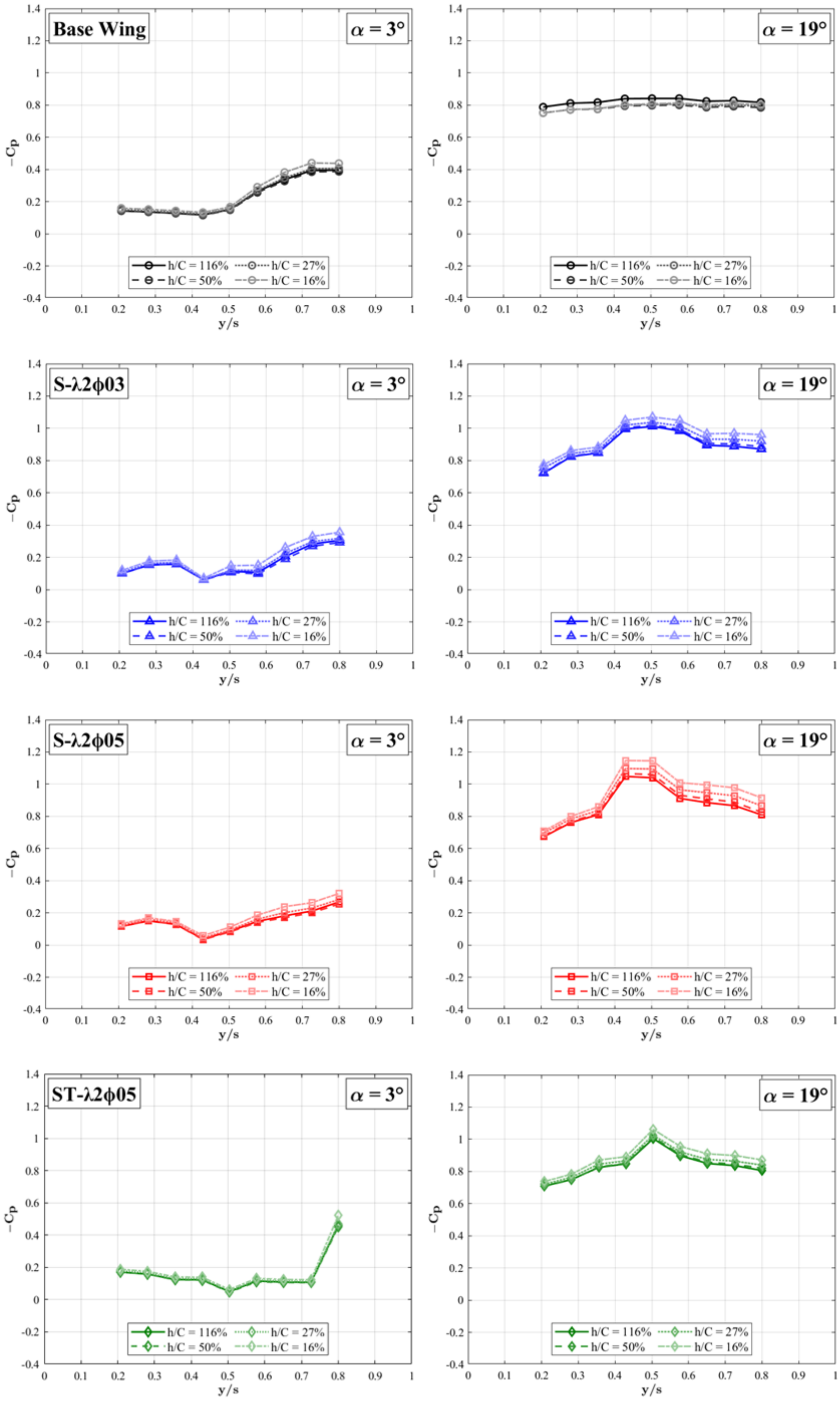

Figure 4.9 Distribution of pressure coefficient at various angles of attack and height-to-chord ratios for base, S-λ2ϕ03, S-λ2ϕ05, and ST-λ2ϕ05 wing models on half span at $x/C = 0.5$.

4.3 Near-Surface PIV Results

The results of near-surface PIV measurements conducted for the base, S-λ2ϕ03, S-λ2ϕ05, and ST-λ2ϕ05 wing models in the out-of-ground effect (OGE) are presented in this chapter. Symmetry tests were conducted to check the symmetry of the flow field. Since the symmetry of the flow field was confirmed, the half wing was studied to increase spatial resolution. Time-averaged streamline patterns ⟨ψ⟩ for the base, S-λ2ϕ03, S-λ2ϕ05, and ST-λ2ϕ05 wing models are given in Figure 4.10, Figure 4.11, and Figure 4.12 at angles of attack of $\alpha = 10°$, $\alpha = 17°$, and $\alpha = 22°$, respectively. Vector fields and velocity contours for the base, S-λ2ϕ03, S-λ2ϕ05, and ST-λ2ϕ05 wing models are presented in Appendix F

At angles of attack of $\alpha = 10°$ and $\alpha = 17°$, a distinct positive bifurcation line is present for all the wing models, indicating the flow attachment to the surface. The base wing model, presented in the top left image of Figure 4.10, shows positive and negative bifurcation lines at $\alpha = 10°$. Besides these flow structures, there are no distinct structures in the base wing model at $\alpha = 10°$. The S-λ2ϕ05 wing model, presented in the upper right image of Figure 4.10, shows three distinct foci with different strengths. The first focus forms behind the fourth tubercle, exhibiting the weakest magnitude. The second focus is formed behind the fifth tubercle, while the third, and the largest, focus is formed behind the sixth tubercle. The S-λ2ϕ03 wing model, presented in the lower left image of Figure 4.10, shows a similar flow structure to the S-λ2ϕ05 wing model. However, this wing shows two distinct foci of separation, the first forming behind the fifth tubercle and the second behind the sixth tubercle. Comparing the S-λ2ϕ05 and S-λ2ϕ03 wing models at $\alpha = 10°$ shows the effect of the amplitude ratio on the flow structure. The SLE wing model with a higher amplitude ratio shows an additional focus point in its flow field. The streamline pattern of the ST-λ2ϕ05 wing model shows distinct behavior at $\alpha = 10°$, compared to other wing models. A distinct negative bifurcation line was not observed for this wing model near the leading edge. However, combinations of bifurcation lines were observed over the ST-λ2ϕ05 wing model at this angle of attack.

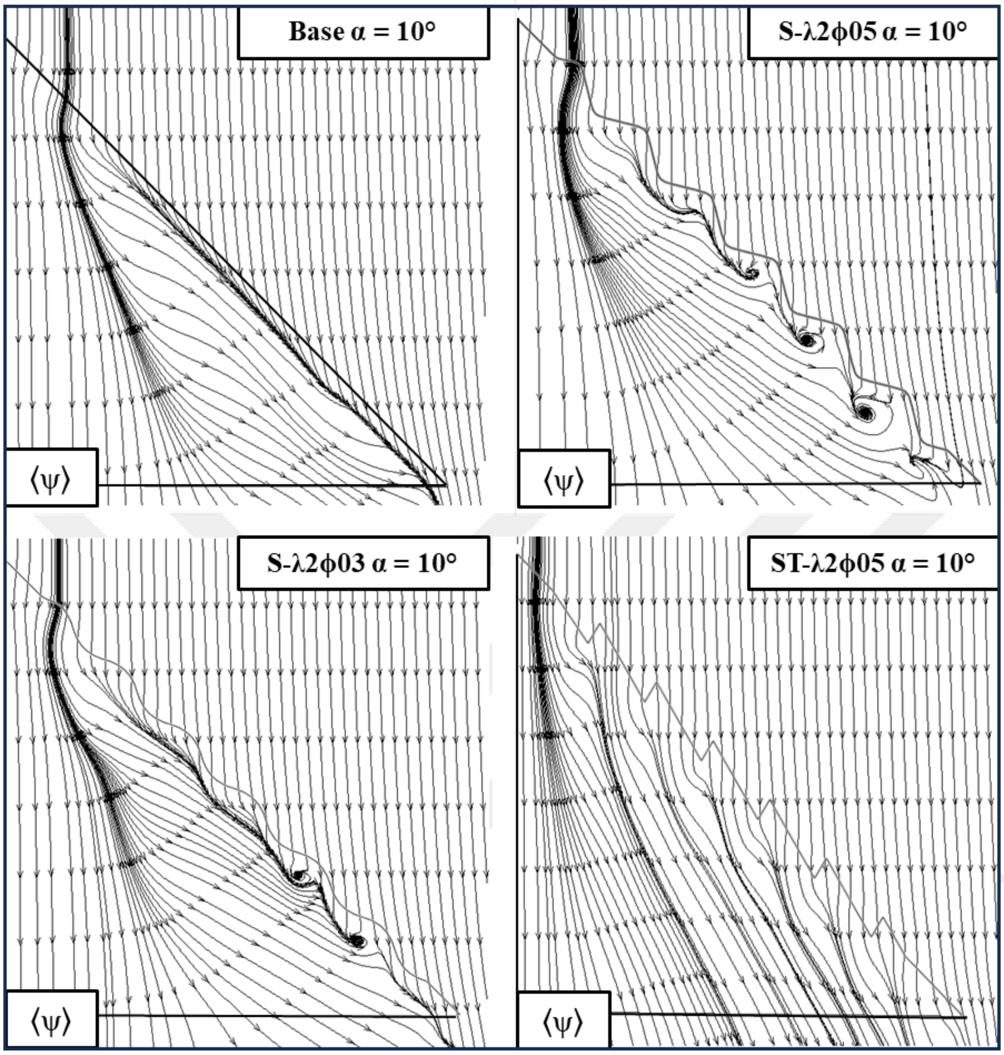

Figure 4.10 Time-averaged streamline patterns ⟨ψ⟩ of base, S-λ2ϕ03, S-λ2ϕ05, and ST-λ2ϕ05 wing models at $\alpha = 10°$.

As the angle of attack increases from $\alpha = 10°$ to $\alpha = 17°$, the attachment line of all the wing models approaches the centerline of the wing, as shown in Figure 4.11. Indications of backflow were observed near the tip of the trailing edge for the base, S-λ2ϕ03, and S-λ2ϕ05 wing models. Chordwise and spanwise locations of these backflow regions are very similar. In contrast, the flow structure of the ST-λ2ϕ05 wing model at $\alpha = 17°$ is like that of other wing models at $\alpha = 10°$, showing no backflow. Moreover, this wing model exhibits a bifurcation line near the leading edge at this angle of attack compared to its streamline pattern at $\alpha = 10°$.

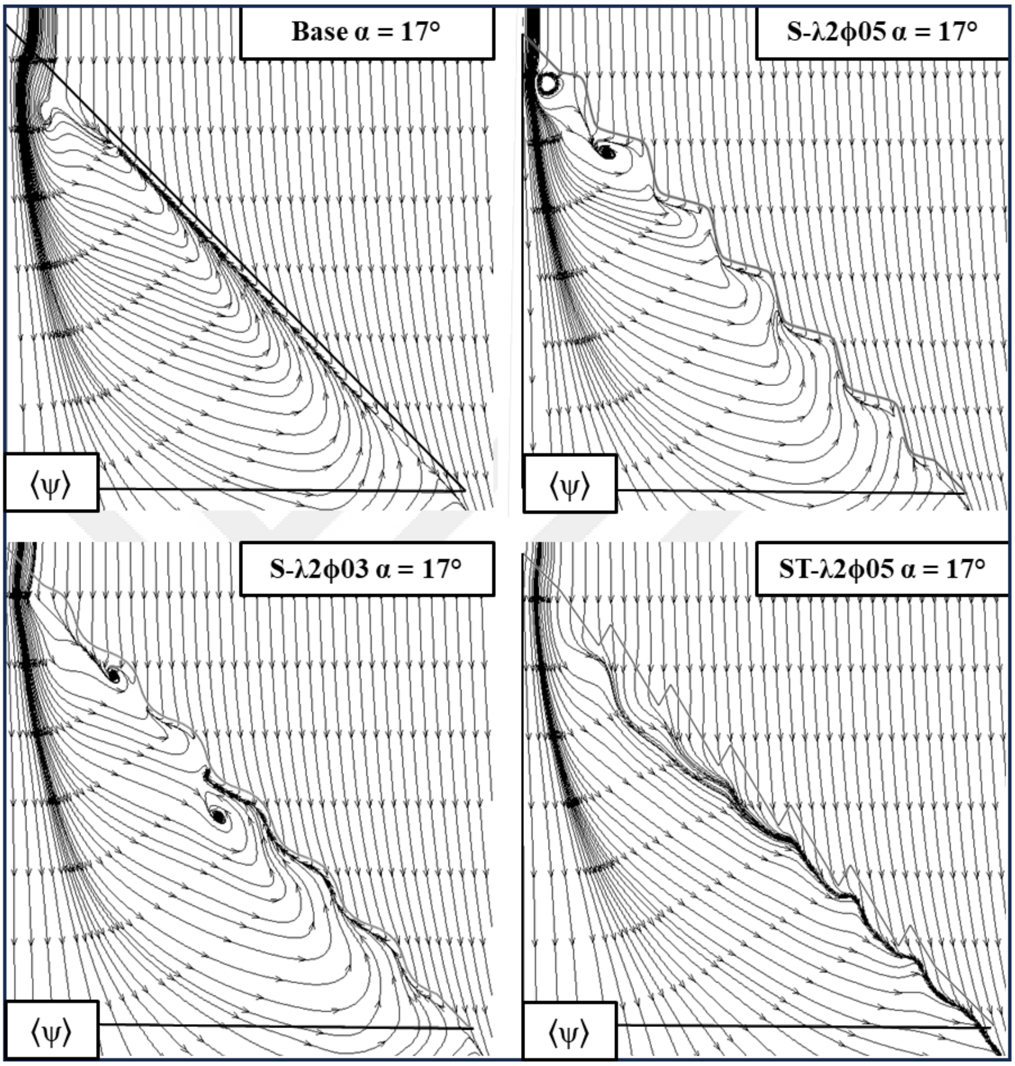

Figure 4.11 Time-averaged streamline patterns ⟨ψ⟩ of base, S-λ2ϕ03, S-λ2ϕ05, and ST-λ2ϕ05 wing models at $\alpha = 17°$.

Figure 4.12 presents the time-averaged streamline patterns of all the wing models at $\alpha = 22°$. A backflow region is observed for the ST-λ2ϕ05 wing model at this angle of attack. Moreover, the backflow regions increased in size and are observed more inward for all the wing models at this angle of attack compared to the backflow regions at $\alpha = 17°$. The base wing model has a distinct flow structure at this angle of attack compared to the modified wing models. This structure indicates the large-scale three-dimensional surface separation at this angle of attack. However, the modified wing models do not show such a structure. Foci of modified wing models are located closer to the apex compared to the base wing model, indicating three-dimensional separation on a smaller scale compared to the base wing model. This results in a delayed three-dimensional separation, supporting the stall-delaying claims of aerodynamic coefficient results.

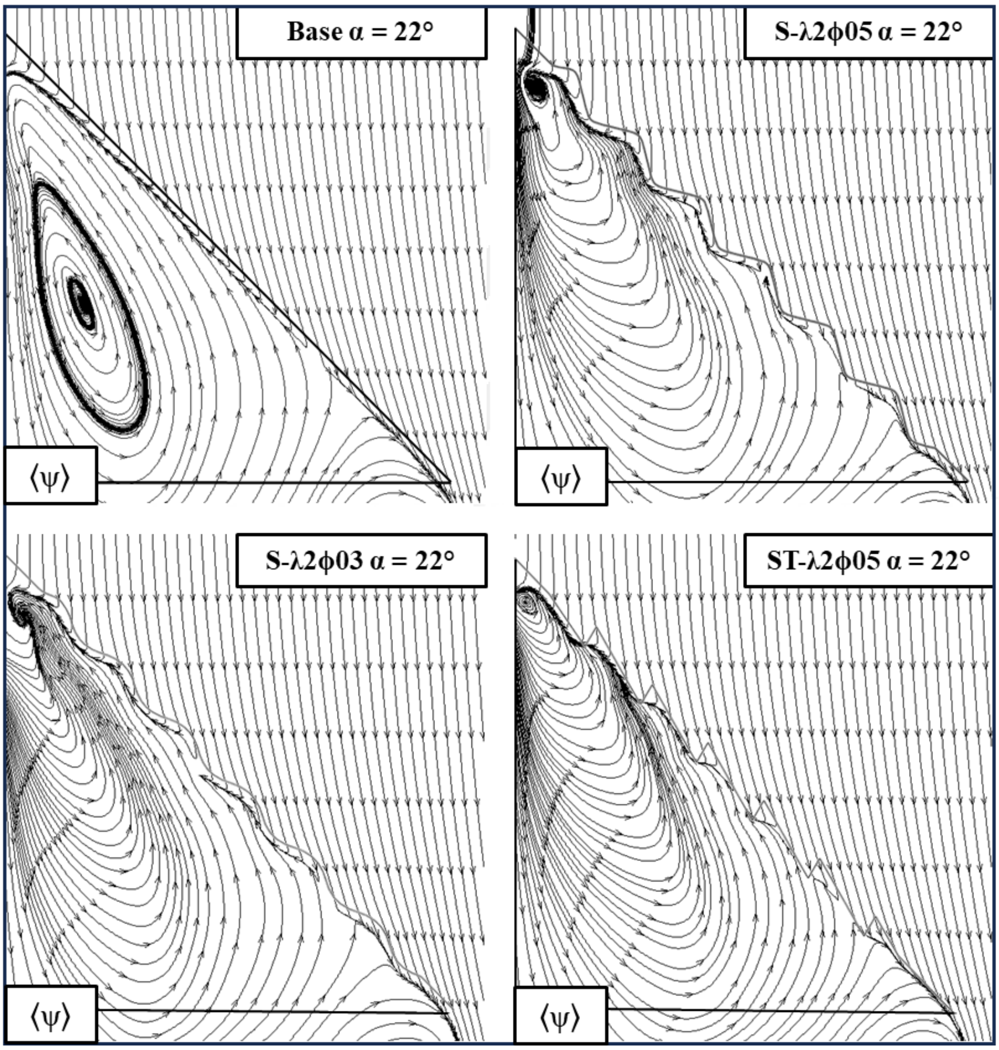

Figure 4.12 Time-averaged streamline patterns ⟨ψ⟩ of base, S-λ2ϕ03, S-λ2ϕ05, and ST-λ2ϕ05 wing models at $\alpha = 22°$.

Time-averaged vorticity contours ⟨ω⟩ for the base, S-λ2ϕ03, S-λ2ϕ05, and ST-λ2ϕ05 wing models are given in Figure 4.13, Figure 4.14, and Figure 4.15 at angles of attack of $\alpha = 10°$, $\alpha = 17°$, and $\alpha = 22°$, respectively.

At an angle of attack of $\alpha = 10°$, the base wing model exhibits elongated vorticity regions along the leading-edge, indicating a leading-edge vortex (LEV) structure, as shown in Figure 4.13. The positive bifurcation line observed in the streamline pattern of the base wing model at this angle of attack supports this finding. Strong negative vorticity regions are observed along the leading edge of the base, S-λ2ϕ03, and S-λ2ϕ05 wing models at $\alpha = 10°$. These models show a more neutral vorticity region at the apex of the wing. However, the ST-λ2ϕ05 wing model exhibits a negative vorticity region at the apex. The ST-λ2ϕ05 wing model shows fragmental, elongated negative vorticity regions behind the crests, and positive regions behind the troughs. This structure may indicate multiple small-sized leading-edge vortices, which could explain the distinct streamline pattern and the increased lift coefficient at this angle of attack for this wing model compared to the base wing model. The LEV structure of the base wing model weakens towards the trailing edge, while the multiple LEV structures provide high vorticity regions near the trailing edge. Since leading-edge vortices create suction forces contributing to the lift, the ST-λ2ϕ05 wing model creates higher lift coefficients near $\alpha = 10°$. The S-λ2ϕ05 wing model shows positive vorticity regions behind the troughs in contrast to the ST-λ2ϕ05 wing model. The primary vortex is pronounced for the base wing model, while the modified wing models do not exhibit such a clear primary vortex structure. A second negative vorticity region more inboard of the base wing model is observed at $\alpha = 10°$. This may indicate a dual-vortex structure; however, further investigation is needed to confirm this finding. This structure is not clearly observed for the modified wing models.

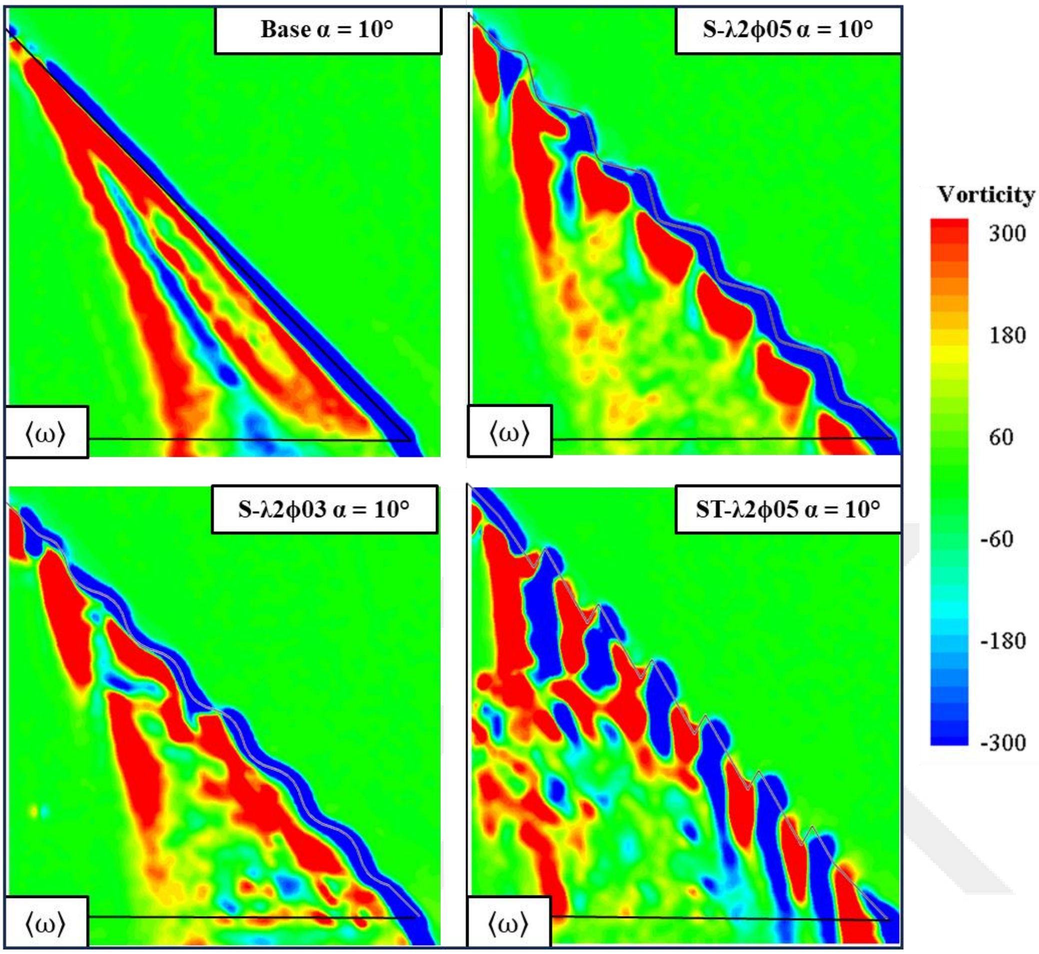

Figure 4.13 Time-averaged vorticity contours ⟨ω⟩ of base, S-λ2ϕ03, S-λ2ϕ05, and ST-λ2ϕ05 wing models at $\alpha = 10°$.

The primary vortex is still clearly observed for the base wing model and more pronounced for the modified wing models at $\alpha = 17°$ compared to $\alpha = 10°$, as shown in Figure 4.14. The elongated positive vorticity regions for the base and sinusoidal wing models are closer to their centerline at this angle of attack compared to $\alpha = 10°$. Moreover, at $\alpha = 17°$ the base wing's inboard negative vorticity region, indicating vortex breakdown, is observed closer to the apex compared to at $\alpha = 10°$. At $\alpha = 17°$, the vorticity contours of sinusoidal wing models are more similar to those of the base wing model at $\alpha = 10°$, compared to the saw-tooth wing model. The fragmental positive vorticity regions behind the S-λ2ϕ05 at $\alpha = 10°$ are no longer observed at $\alpha = 17°$. In contrast, the fragmental negative and positive vorticity regions are still exhibited at $\alpha = 17°$ for the ST-λ2ϕ05 wing model, although these regions are significantly reduced in size. The vorticity contours and streamline patterns of the ST-λ2ϕ05 wing model indicate that this leading-edge modification energizes the flow and works effectively as a vortex generator.

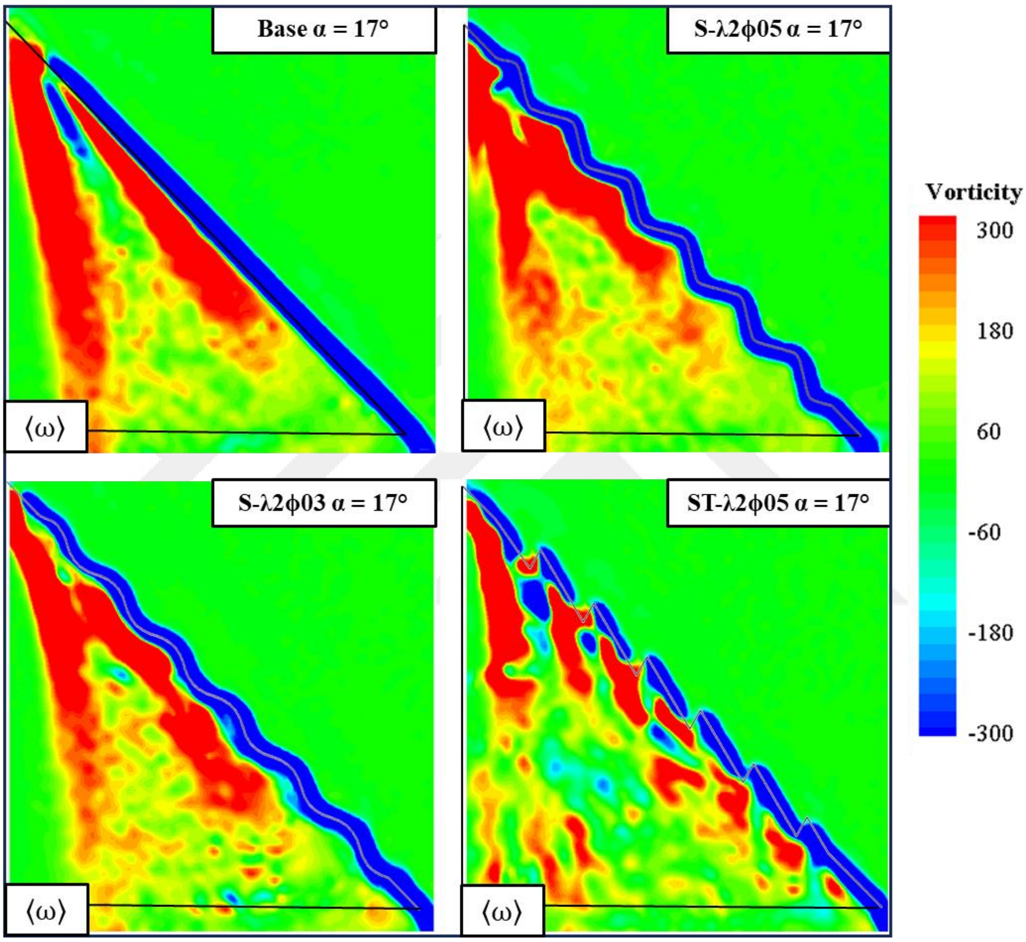

Figure 4.14 Time-averaged vorticity contours ⟨ω⟩ of base, S-λ2ϕ03, S-λ2ϕ05, and ST-λ2ϕ05 wing models at $\alpha = 17°$.

A negative vorticity region at the leading edge of all the wing models is observed, as shown in Figure 4.15. The vorticity contours observed at $\alpha = 22°$ for the base wing model indicate a large-scale three-dimensional flow separation. However, magnitudes of the positive vorticity regions for the S-λ2ϕ05 and ST-λ2ϕ05 wing models are higher compared to other wing models at $\alpha = 22°$, suggesting that the three-dimensional flow separation is delayed.

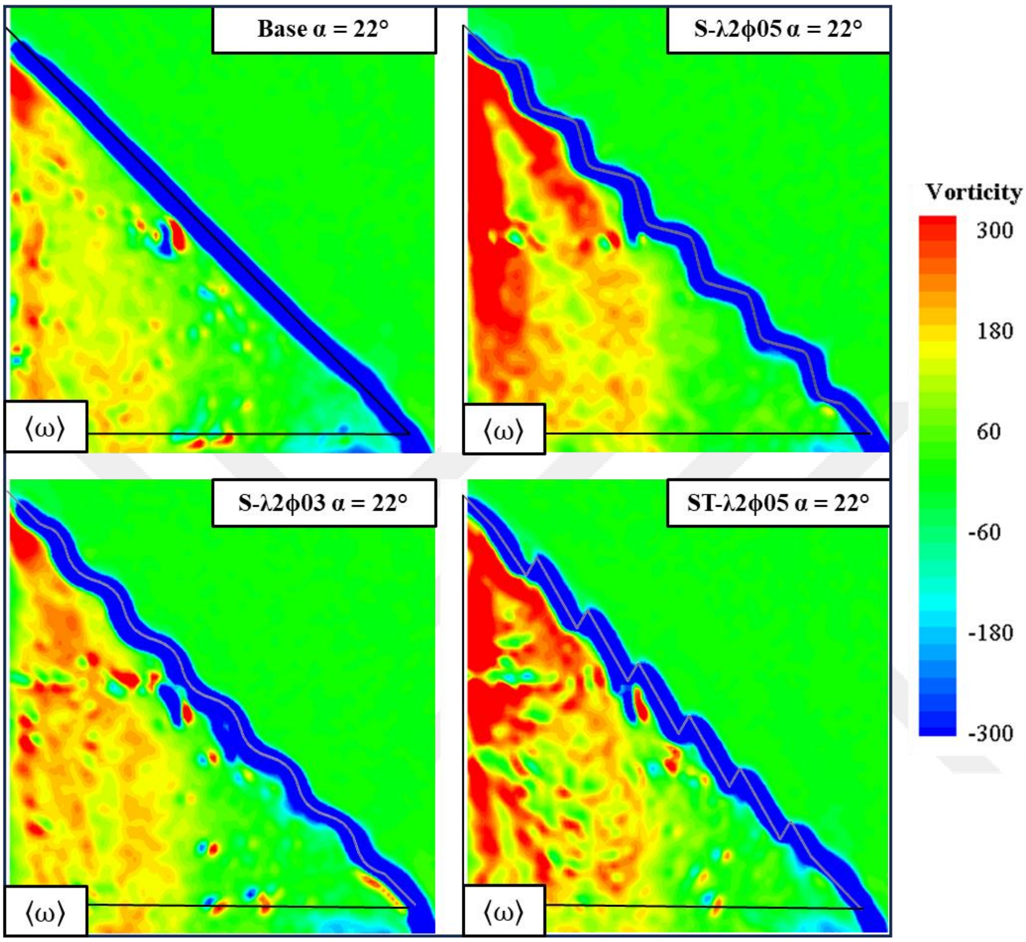

Figure 4.15 Time-averaged vorticity contours ⟨ω⟩ of base, S-λ2ϕ03, S-λ2ϕ05, and ST-λ2ϕ05 wing models at $\alpha = 22°$.

CHAPTER 5

CONCLUSION

The effect of bio-inspired leading-edge modifications on the aerodynamic performance of a non-slender delta wing with a sweep angle of $\Lambda = 45°$ was presented in the current study. Four sinusoidal and two saw-tooth leading-edge wing models with different wavelength and amplitude ratios were compared with a base wing model. Force and surface pressure measurements were performed at a Reynolds number of $Re = 1 \times 10^5$ over a wide angle of attack range, and near-surface PIV measurements were performed at a Reynolds number of $Re = 7.5 \times 10^4$ over three different angles of attack in a low-speed wind tunnel. The conclusions of the study, along with the recommendations for future work, are summarized below.

5.1 Out-of-Ground Effect

The main findings of this study regarding the out-of-ground effect force, surface pressure, and near-surface PIV measurements are:

1. Force measurement results revealed that utilizing bio-inspired leading-edge modifications delayed stall and increased maximum lift coefficient ($C_{L\,max}$) value. Moreover, the bio-inspired wing models showed an increased lift coefficient compared to the base wing model over the angle of attack of $\alpha = 17°$, providing smoother stall characteristics. The S-λ2ϕ05 and ST-λ2ϕ05 models delay stall up to 4 degrees, both stalling around $\alpha = 21°$. Pressure measurement results showed delayed stall onset for the modified wings, supporting the results of aerodynamic coefficients. The ST-λ2ϕ05 wing model demonstrated smaller suction regions, hence lower lift generation capability at $\alpha = 11°$, while having the highest lift coefficient among all the

wing models at this angle of attack. This indicates a high promotion of leading-edge vortices at lower angles of attack.

2. There is no significant difference in the drag, lift, and moment coefficient among the wing models below $\alpha = 10°$. However, the lift-to-drag coefficient significantly differs among the wing models as the angle of attack exceeds $\alpha = 5°$. As the angle of attack increases over $\alpha = 17°$, an increase in the drag, lift, and moment coefficient for the modified wing models compared to the base wing model is apparent. When the lift-to-drag ratio is considered, the ST-λ2ϕ05 and S-λ2ϕ03 models show better aerodynamic performance between $\alpha = 6°$ and $\alpha = 9°$. The base wing model shows better aerodynamic performance than the modified wings as the angle of attack increases further, yet the difference is minor.
3. The moment coefficient results demonstrated similar slopes for all the wing models at the lower angles of attack. However, as the angle of attack increases further, S-λ2ϕ05 and ST-λ2ϕ05 wing models show distinct behaviors. The S-λ2ϕ05 wing model indicates lower stability between the angles of attack of $5°$ to $11°$ and the ST-λ2ϕ05 wing model shows higher stability between the angles of attack of $11°$ to $19°$, compared to other wing models. The bio-inspired wing models generally showed a lower longitudinal static stability as the angle of attack surpassed $\alpha = 17°$. Bio-inspired leading-edge modifications can improve the maneuverability of an aircraft and can be utilized in various applications, since these modifications provide higher lift, smoother stall characteristics, and lower negative rate of change in moment coefficient. A reduction in longitudinal static stability at high angles of attack can enhance maneuverability, which is advantageous in air combat scenarios. However, for non-slender delta wings operating at low speeds, such reductions must be carefully balanced to preserve adequate control authority and ensure acceptable handling qualities.
4. Streamline patterns obtained from surface-PIV measurements showed that the ST-λ2ϕ05 wing model exhibited a distinct streamline pattern with

combinations of bifurcation lines, which did not show a distinct negative bifurcation line at $\alpha = 10°$. This pattern differed significantly from the sinusoidal wing models. Moreover, when the angle of attack increased from $\alpha = 10°$ to $\alpha = 17°$, indications of backflow were present for every wing model except the saw-tooth model. At $\alpha = 22°$, the flow pattern of the base wing shows indications of three-dimensional flow separation. In contrast, the focal points of modified wing models are closer to the apex compared to the base wing, indicating delayed three-dimensional separation.

5. Vorticity calculations from surface-PIV measurements showed that the ST-λ2ϕ05 wing model exhibits fragmental, elongated negative vorticity regions behind the crests at $\alpha = 10°$, indicating multiple small-scaled leading-edge vortices. Moreover, the S-λ2ϕ05 and ST-λ2ϕ05 wing models show fragmental positive regions behind the troughs at $\alpha = 10°$. At an angle of attack of $\alpha = 17°$, these positive regions are no longer observed for the S-λ2ϕ05 wing model. In contrast, the ST-λ2ϕ05 wing model exhibits reduced negative and positive regions at this angle of attack. The PIV measurements revealed that the leading-edge modifications of the ST-λ2ϕ05 wing model effectively work as a vortex generator and energize the flow. Large-scale three-dimensional flow separation is observed for the base wing model at $\alpha = 22°$. In contrast, the S-λ2ϕ05 and ST-λ2ϕ05 wing models indicate a delay in the three-dimensional flow separation, exhibiting higher magnitudes of positive vorticity regions.

5.2 In-Ground Effect

The main findings of this study regarding the ground effect force and surface pressure measurements are:

1. Force measurement results in ground effect revealed that as the ground clearance decreased, the maximum lift coefficient ($C_{L\,max}$) increased for all the wing models. However, the increase rate was not the same for all the wing

models. S-λ1ϕ02 and ST-λ2ϕ03 wing models showed the highest increase rate, with a $\sim 16\%$ increase in the maximum lift coefficient as the ground clearance decreases from $\mathrm{h/C} = 116\%$ to $\mathrm{h/C} = 16\%$. The stall angle was observed to be independent of the ground effect.

2. Similar to the out-of-ground effect, the drag coefficient showed similar trend in all the wing models at lower angles of attack, and the rate of change in the drag coefficient decreased as the angle of attack surpassed $\alpha = 17°$ at $\mathrm{h/C} = 16\%$. The drag coefficient increased for all the wing models as the ground clearance decreased.
3. The aerodynamic performance of the S-λ3ϕ05 wing model was affected the most by the ground effect with an increase rate of $\sim 10\%$. Surface pressure values did not vary significantly by the effect of ground.

5.3 Recommendations for Future Work

This study has experimentally investigated the effect of sinusoidal leading-edge modifications on a non-slender delta wing and the ground effect on these wing models. The present study can be improved in the following ways:

- The force measurements can be conducted at higher Reynolds numbers to investigate the aerodynamic performance of bio-inspired wing models at different flight conditions.
- The force and pressure measurements can be conducted with a dynamic ground condition to investigate the aerodynamic performance of bio-inspired wing modifications under more realistic ground effect.
- Wings with different wavelength and amplitude ratios can be investigated to further discuss the effect of these ratios on the aerodynamic performance.
- The flow structure and pressure trend of the ST-λ2ϕ05 wing model show distinct behaviors, while showing one of the best aerodynamic performances. Therefore, the saw-tooth wing models with various amplitude and

wavelength ratios can be further investigated with force, pressure, and PIV measurements.

- The effect of the ground can be further investigated with crossflow PIV measurements.
- Different sinusoidal and saw-tooth configurations can be utilized in specialized locations in small sections, such as near the apex, to investigate these modifications' effect on the aerodynamic coefficients.

REFERENCES

[1] S. Gupta, S. Kumar, and R. Kumar, "Control of leading-edge vortices over delta wing using flow control methods: A review," *Mater Today Proc*, vol. 50, pp. 2189–2193, 2022.

[2] M. Ramakrishna, C. Senthil Kumar, and B. Venkatesh, "Influence of leading edge shapes on vortex behaviour of delta wing," in *Journal of Physics: Conference Series*, 2019.

[3] I. Gursul, D. J. Cleaver, and Z. Wang, "Control of low Reynolds number flows by means of fluid-structure interactions," *Progress in Aerospace Sciences*, vol. 64, pp. 17–55, 2014, doi: 10.1016/j.paerosci.2013.07.004.

[4] I. Gursul, Z. Wang, and E. Vardaki, "Review of flow control mechanisms of leading-edge vortices," Oct. 2007. doi: 10.1016/j.paerosci.2007.08.001.

[5] G. Koçak and M. M. Yavuz, "Effect of ground on aerodynamics and longitudinal static stability of a non-slender delta wing," *Aerosp Sci Technol*, vol. 130, Nov. 2022, doi: 10.1016/j.ast.2022.107929.

[6] S. Tumse, M. O. Tasci, I. Karasu, and B. Sahin, "Effect of ground on flow characteristics and aerodynamic performance of a non-slender delta wing," *Aerosp Sci Technol*, vol. 110, Mar. 2021, doi: 10.1016/j.ast.2020.106475.

[7] J. B. R. Rose, S. G. Natarajan, and V. T. Gopinathan, "Biomimetic flow control techniques for aerospace applications: a comprehensive review," 2021, *Springer*. doi: 10.1007/s11157-021-09583-z.

[8] H. K. Naeini, M. Nili-Ahmadabadi, Y. S. Park, and K. C. Kim, "Effect of nature-inspired needle-shaped vortex generators on the aerodynamic features of a double-delta wing," *Int J Mech Sci*, vol. 202–203, 2021, doi: 10.1016/j.ijmecsci.2021.106502.

[9] A. Shahsavari, M. Nili-Ahmadabadi, A. Aslani, and K. C. Kim, “Introduction of a biomimetic device designed to improve the flow over a slender delta wing: visualization study,” *J Vis (Tokyo)*, Feb. 2024, doi: 10.1007/s12650-024-00961-7.

[10] J. Anders, “Biomimetic Flow Control,” *AIAA Journal*, 2000, doi: 10.2514/6.2000-2543.

[11] S. I. Lee, J. Kim, H. Park, P. G. Jabłoński, and H. Choi, “The function of the alula in avian flight,” *Sci Rep*, vol. 5, May 2015, doi: 10.1038/srep09914.

[12] M. R. Ito, C. Duan, and A. A. Wissa, “The function of the alula on engineered wings: A detailed experimental investigation of a bioinspired leading-edge device,” *Bioinspir Biomim*, vol. 14, no. 5, Aug. 2019, doi: 10.1088/1748-3190/ab36ad.

[13] F. E. Fish, P. W. Weber, M. M. Murray, and L. E. Howle, “The tubercles on humpback whales’ flippers: Application of bio-inspired technology,” in *Integrative and Comparative Biology*, Jul. 2011, pp. 203–213. doi: 10.1093/icb/icr016.

[14] M. L. Post, R. Decker, A. R. Sapell, and J. S. Hart, “Effect of bio-inspired sinusoidal leading-edges on wings,” *Aerosp Sci Technol*, vol. 81, pp. 128–140, Oct. 2018, doi: 10.1016/J.AST.2018.07.043.

[15] D. S. Miklosovic, M. M. Murray, L. E. Howle, and F. E. Fish, “Leading-edge tubercles delay stall on humpback whale (Megaptera novaeangliae) flippers,” *Physics of Fluids*, vol. 16, no. 5, 2004, doi: 10.1063/1.1688341.

[16] H. S. Yoon, P. A. Hung, J. H. Jung, and M. C. Kim, “Effect of the wavy leading edge on hydrodynamic characteristics for flow around low aspect ratio wing,” *Comput Fluids*, vol. 49, no. 1, pp. 276–289, Oct. 2011, doi: 10.1016/j.compfluid.2011.06.010.

[17] G. Moscato, J. Mohamed, and G. P. Romano, “Improving performances of biomimetic wings with leading-edge tubercles,” *Exp Fluids*, vol. 63, no. 9, 2022, doi: 10.1007/s00348-022-03493-8.

[18] E. Cui and X. Zhang, “Ground Effect Aerodynamics,” in *Encyclopedia of Aerospace Engineering*, Wiley, 2010. doi: 10.1002/9780470686652.eae022.

[19] L. W. Traub, “Experimental and Analytic Investigation of Ground Effect,” *J Aircr*, vol. 52, pp. 235–243, 2015, doi: 10.2514/1.C032676.

[20] J. Gross and L. W. Traub, “Experimental and theoretical investigation of ground effect at low reynolds numbers,” *J Aircr*, vol. 49, no. 2, pp. 576–586, 2012, doi: 10.2514/1.C031595.

[21] L. C. Johansson, L. Jakobsen, and A. Hedenström, “Flight in Ground Effect Dramatically Reduces Aerodynamic Costs in Bats,” *Current Biology*, vol. 28, no. 21, pp. 3502-3507.e4, Nov. 2018, doi: 10.1016/J.CUB.2018.09.011.

[22] J. M. V Rayner, “On the Aerodynamics of Animal Flight in Ground Effect,” *Philosophical Transactions: Biological Sciences*, vol. 334, no. 1269, pp. 119–128, 1991.

[23] B. Earnshaw and J. A. Lawford, “Low-Speed Wind-Tunnel Series of Sharp-Edged Experiments on Delta Wings,” *Aeronautical Research Council, Reports and Memoranda,* vol. No. 3424, 1966.

[24] I. Gursul, R. Gordnier, and M. Visbal, “Unsteady aerodynamics of nonslender delta wings,” *Progress in Aerospace Sciences*, vol. 41, no. 7, pp. 515–557, 2005, doi: 10.1016/j.paerosci.2005.09.002.

[25] M. Gad-El-Hak and R. F. Blackwelder, “The discrete vortices from a delta wing,” *AIAA Journal*, vol. 23, no. 6, pp. 961–962, 1985, doi: 10.2514/3.9016.

[26] M. Lee and C.-M. Ho, “Lift force of delta wings,” *Appl Mech Rev*, vol. 43, no. 9, pp. 209–221, Sep. 1990.

[27] G. S. Taylor and I. Gursul, “Buffeting flows over a low-sweep delta wing,” *AIAA Journal*, vol. 42, no. 9, pp. 1737–1745, 2004, doi: 10.2514/1.5391.

[28] S. Leibovich, “The Structure of Vortex Breakdown,” *Annu Rev Fluid Mech*, vol. 10, pp. 221–267, 1978.

[29] T. Sarpkaya, “On stationary and travelling vortex breakdowns,” *J Fluid Mech*, vol. 45, pp. 545–559, 1971.

[30] O. Lucca-Negro and T. O’doherty, “Vortex breakdown: a review,” *Prog Energy Combust Sci*, vol. 27, pp. 431–481, 2001.

[31] F. M. Payne, T. T. Ng, R. C. Nelson, and L. B. Schiff, “Visualization and wake surveys of vortical flow over a delta wing,” *AIAA Journal*, vol. 26, no. 2, pp. 137–143, 1988, doi: 10.2514/3.9864.

[32] J. A. Ekaterinaris, R. L. Coutley, L. B. Schiff, and M. F. Platzer, “Numerical investigation of high incidence flow over a double-delta wing,” *J Aircr*, vol. 32, no. 3, pp. 457–463, 1995, doi: 10.2514/3.46742.

[33] J. L. Thomas, S. T. Krist, and W. K. Anderson, “Navier-Stokes computations of vortical flows over low-aspect-ratio wings,” *AIAA Journal*, vol. 28, no. 2, pp. 205–212, 1990, doi: 10.2514/3.10376.

[34] K. Fujii and L. B. Schiff, “Numerical simulation of vortical flows over a strake-delta wing,” *AIAA Journal*, vol. 27, no. 9, pp. 1153–1162, 1989, doi: 10.2514/3.10239.

[35] W. Jinjun and Z. Wang, “Experimental Investigations on Leading-Edge Vortex Structures for Flow over Non-Slender Delta Wings,” *Chinese Physics Letters*, vol. 25, pp. 2550–2553, 2008.

[36] W. J. McCroskey, “The Phenomenon of Dynamic Stall,” Mar. 1981.

[37] B. Gülsaçan, G. Şencan, and M. M. Yavuz, “Effect of thickness-to-chord ratio on flow structure of a low swept delta wing,” *AIAA Journal*, vol. 56, no. 12, pp. 4657–4668, Dec. 2018, doi: 10.2514/1.J057083.

[38] A. Celik and M. M. Yavuz, “Effect of edge modifications on flow structure of low swept delta wing,” *AIAA Journal*, vol. 54, no. 5, pp. 1789–1797, 2016, doi: 10.2514/1.J054587.

[39] M. Jahanmiri, “Active Flow Control: A Review,” Göteborg, 2010.

[40] Gad-el-Hak, “Introduction to Flow Control,” in *Flow Control: Fundamentals and Practices*, Berlin: Springer, 1998, ch. 1, pp. 1–108.

[41] Y. Yin, “Current study on active flow control and passive flow control,” *Theoretical and Natural Science*, vol. 26, no. 1, pp. 227–234, Dec. 2023, doi: 10.54254/2753-8818/26/20241094.

[42] T. Moghaddam and N. B. Neishabouri, “On the Active and Passive Flow Separation Control Techniques over Airfoils,” in *IOP Conference Series: Materials Science and Engineering*, Institute of Physics Publishing, Oct. 2017. doi: 10.1088/1757-899X/248/1/012009.

[43] I. Gursul, S. Srinivas, and G. Batta, “Active control of vortex breakdown over a delta wing,” *AIAA Journal*, vol. 33, no. 9, pp. 1743–1745, 1995, doi: 10.2514/3.12721.

[44] N. J. Wood and L. Roberts, “The Control of Vortical Lift on Delta Wings by Tangential Leading Edge Blowing.”

[45] N. M. Williams, Z. Wang, and I. Gursul, “Active Flow Control on a Nonslender Delta Wing,” 2008.

[46] A. A. Sidorenko *et al.*, “Plasma control of vortex flow on a delta wing at high angles of attack,” *Exp Fluids*, vol. 54, no. 8, Aug. 2013, doi: 10.1007/s00348-013-1585-4.

[47] C. Çetin, A. Çelik, and M. M. Yavuz, “Control of flow structure over a nonslender delta wing using periodic blowing,” *AIAA Journal*, vol. 56, no. 1, pp. 90–99, 2018, doi: 10.2514/1.J056099.

[48] S. M. Klute, O. K. Rediniotis, and D. P. Telionis, “Flow control over a maneuvering delta wing at high angles of attack,” *AIAA Journal*, vol. 34, no. 4, pp. 662–668, 1996, doi: 10.2514/3.13125.

[49] K. Kestel, B. Ramazanlı, and M. M. Yavuz, “Control of flow structure over a non-slender delta wing using passive bleeding,” *Aerosp Sci Technol*, vol. 106, Nov. 2020, doi: 10.1016/j.ast.2020.106136.

[50] H. Johari, C. Henoch, D. Custodio, and A. Levshin, “Effects of leading-edge protuberances on airfoil performance,” *AIAA Journal*, vol. 45, no. 11, pp. 2634–2642, 2007, doi: 10.2514/1.28497.

[51] O. Lilienthal, *Birdflight as the Basis of Aviation*. New York, Bombay, and Calcutta: Longmans, Green, and Co., 1911.

[52] C. Rao and H. Liu, “Effects of Reynolds Number and Distribution on Passive Flow Control in Owl-Inspired Leading-Edge Serrations,” in *Integrative and Comparative Biology*, Oxford University Press, 2020, pp. 1135–1146. doi: 10.1093/ICB/ICAA119.

[53] W. Akpan and E. J. Oduobuk, “Aerodynamics of Birds’ Flight: Analysis and Applications,” *Article in International Journal of Applied Science-Research and Review*, 2023, doi: 10.56293/IJASR.2022.5549.

[54] A. G. Domel, M. Saadat, J. C. Weaver, H. Haj-Hariri, K. Bertoldi, and G. V. Lauder, “Shark skin-inspired designs that improve aerodynamic performance,” *J R Soc Interface*, vol. 15, no. 139, 2018, doi: 10.1098/rsif.2017.0828.

[55] M. Muthuramalingam, L. S. Villemin, and C. Bruecker, “Streak formation in flow over biomimetic fish scale arrays,” *Journal of Experimental Biology*, vol. 222, no. 16, 2019, doi: 10.1242/jeb.205963.

[56] T. Goruney and D. Rockwell, “Flow past a delta wing with a sinusoidal leading edge: Near-surface topology and flow structure,” *Exp Fluids*, vol. 47, no. 2, pp. 321–331, Aug. 2009, doi: 10.1007/s00348-009-0666-x.

[57] H. Chen and J. J. Wang, “Vortex structures for flow over a delta wing with sinusoidal leading edge,” *Exp Fluids*, vol. 55, no. 6, 2014, doi: 10.1007/s00348-014-1761-1.

[58] H. Chen, C. Pan, and J. Wang, “Effects of sinusoidal leading edge on delta wing performance and mechanism,” *Sci China Technol Sci*, vol. 56, no. 3, pp. 772–779, 2013, doi: 10.1007/s11431-013-5143-3.

[59] I. Zverkov, B. Zanin, and V. Kozlov, “Disturbances growth in boundary layers on classical and wavy surface wings,” *AIAA Journal*, vol. 46, no. 12, pp. 3149–3158, Dec. 2008, doi: 10.2514/1.37562.

[60] J. L. E. Guerreiro and J. M. M. Sousa, “Low-Reynolds-Number Effects in Passive Stall Control Using Sinusoidal Leading Edges,” *AIAA Journal*, vol. 50, no. 2, pp. 461–469, 2012, doi: 10.2514/1.J051235.

[61] K. Hansen, R. M. Kelso, and B. Dally, “An Investigation of Three-Dimensional Effects on the Performance of Tubercles at Low Reynolds Numbers,” in *17th Australasian Fluid Mechanics Conference*, 2010. [Online]. Available: https://www.researchgate.net/publication/267700453

[62] E. A. van Nierop, S. Alben, and M. P. Brenner, “How bumps on whale flippers delay stall: An aerodynamic model,” *Phys Rev Lett*, vol. 100, no. 5, 2008, doi: 10.1103/PhysRevLett.100.054502.

[63] M. J. Kim, H. S. Yoon, J. H. Jung, H. H. Chun, and D. W. Park, “Hydrodynamic characteristics for flow around wavy wings with different

wave lengths," *International Journal of Naval Architecture and Ocean Engineering*, vol. 4, no. 4, pp. 447–459, 2012, doi: 10.2478/ijnaoe-2013-0110.

[64] M. Zhao, T. Wei, Y. Zhao, and Z. Liu, "Influences of Leading-Edge Tubercle Amplitude on Airfoil Flow Field," *Journal of Thermal Science*, vol. 32, no. 4, pp. 1335–1344, 2023, doi: 10.1007/s11630-023-1465-z.

[65] E. L. Ntantis *et al.*, "Study of Sinusoidal Perturbations on the Leading Edge of an Aircraft Wing," *Journal of Aeronautics, Astronautics and Aviation*, vol. 53, no. 3, pp. 375–386, 2021.

[66] M. D. P. Bolzon, R. M. Kelso, and M. Arjomandi, "Formation of vortices on a tubercled wing, and their effects on drag," *Aerosp Sci Technol*, vol. 56, pp. 46–55, Sep. 2016, doi: 10.1016/j.ast.2016.06.025.

[67] L. Yun, A. Bliault, and J. Doo, *WIG craft and ekranoplan: Ground effect craft technology*. Springer US, 2010. doi: 10.1007/978-1-4419-0042-5.

[68] G. Koçak and M. M. Yavuz, "Effect of ground on aerodynamics and longitudinal static stability of a non-slender delta wing," *Aerosp Sci Technol*, vol. 130, Nov. 2022, doi: 10.1016/j.ast.2022.107929.

[69] G. Koçak and M. M. Yavuz, "Experimental investigation of dynamic ground boundary condition for a non-slender delta wing," *CEAS Aeronaut J*, 2024, doi: 10.1007/s13272-024-00744-8.

[70] M. Oguz Tasci, S. Tumse, and B. Sahin, "Vortical flow characteristics of a slender delta wing in ground effect," *Ocean Engineering*, vol. 261, Oct. 2022, doi: 10.1016/j.oceaneng.2022.112120.

[71] Q. Qu, Z. Lu, H. Guo, P. Liu, and R. K. Agarwal, "Numerical investigation of the aerodynamics of a delta wing in ground effect," in *Journal of Aircraft*, American Institute of Aeronautics and Astronautics Inc., Jan. 2015, pp. 329–340. doi: 10.2514/1.C032735.

[72] M. R. Ahmed and S. D. Sharma, “An investigation on the aerodynamics of a symmetrical airfoil in ground effect,” *Exp Therm Fluid Sci*, vol. 29, no. 6, pp. 633–647, Jul. 2005, doi: 10.1016/j.expthermflusci.2004.09.001.

[73] X. Zhang and J. Zerihan, “Off-surface aerodynamic measurements of a wing in ground effect,” *J Aircr*, vol. 40, no. 4, pp. 716–725, 2003, doi: 10.2514/2.3150.

[74] John H. Lienhard, “The Ground Effect,” The Engines of Our Ingenuity. [Online]. Available: https://engines.egr.uh.edu/episode/2874

[75] Rod Wyndham, “Capturing An African Fish Eagle…Fishing!” [Online]. Available: https://www.sabisabi.com/discover/photography-guide/african-fish-eagle

[76] A. A. Mehraban and M. H. Djavareshkian, “Experimental investigation of ground effects on aerodynamics of sinusoidal leading-edge wings,” *Proc Inst Mech Eng C J Mech Eng Sci*, vol. 235, no. 19, pp. 3988–4001, Oct. 2021, doi: 10.1177/0954406220975422.

[77] H. Lu, K. B. Lua, Y. J. Lee, T. T. Lim, and K. S. Yeo, “Ground effect on the aerodynamics of three-dimensional hovering wings,” *Bioinspir Biomim*, vol. 11, no. 6, Oct. 2016, doi: 10.1088/1748-3190/11/5/066003.

[78] G. R. Abdizadeh, M. Farokhinejad, and S. Ghasemloo, “Numerical investigation on the aerodynamic efficiency of bio-inspired corrugated and cambered airfoils in ground effect,” *Sci Rep*, vol. 12, no. 1, Dec. 2022, doi: 10.1038/s41598-022-23590-2.

[79] J. Wu, S. C. Yang, C. Shu, N. Zhao, and W. W. Yan, “Ground effect on the power extraction performance of a flapping wing biomimetic energy generator,” *J Fluids Struct*, vol. 54, pp. 247–262, Apr. 2015, doi: 10.1016/j.jfluidstructs.2014.10.018.

[80] J. F. D. Câmara and J. M. M. Sousa, “Numerical study on the use of a sinusoidal leading edge for passive stall control at low Reynolds number,” in *51st AIAA Aerospace Sciences Meeting*, 2013. doi: 10.2514/6.2013-62.

[81] K. Liu, B. Song, D. Xue, W. Yang, A. Chen, and Z. Wang, “Numerical study of the aerodynamic effects of bio-inspired leading-edge serrations on a heaving wing at a low Reynolds number,” *Aerosp Sci Technol*, vol. 124, 2022, doi: 10.1016/j.ast.2022.107529.

[82] D. S. Miklosovic, M. M. Murray, and L. E. Howle, “Experimental evaluation of sinusoidal leading edges,” in *Journal of Aircraft*, American Institute of Aeronautics and Astronautics Inc., 2007, pp. 1404–1408. doi: 10.2514/1.30303.

Appendix A

OUT-OF-GROUND EFFECT FORCE/MOMENT COEFFICIENTS CALCULATIONS SOURCE CODE

```
folder_name = 'C:\Users\CASPER\Desktop\Thesis';
cd(folder_name)
addpath(folder_name)

% Chord length of the model
c = 135/1000;   % (m)

fold_name = 'All Over\Result_Diren_ST2_GE';
wing_name = 'ST2';
%colors = [
'#000000','#FF4D00','#FF0000','#0000FF','#660066','#008000','#003333'];
%wing models old names [Base,SLE1,SLE2,SLE3,SLE4,ST1,ST2];
%wing models new names [Base,S-λ3φ05,S-λ2φ05,S-λ2φ03,S-λ1φ02,ST-λ2φ05,
ST-λ2φ03];
%markers = ['o','+','square','^','x','diamond','*'];
plot_color = '#000000';
plot_marker = 'o';
aoa = (-4:2:30)';

prompt1='What is the tunnel speed? (%): ';
prompt7='What is the AoA protractor? ';
A = 18225/10^6;  % (m^2)
fan_speed = 40; % Folder
fan_speed_Vcalc = input(prompt1); % Real Test % Base wing

% For lift curve slope calculation

aoa_protractor = input(prompt7);
aoa_shift = -aoa_protractor-2;
aoa_greater = 8 + aoa_shift;
aoa_lower   = 2 + aoa_shift;

addpath('C:\Users\CASPER\Desktop\Thesis\Post Process Codes')

% Tunnel speed map

load('tunnel_speed_map.mat')
    %% MODEL + TOOLING, INERTIA
    file_name = [fold_name '\Results\' num2str(0) 'per\DW_Results\'];

    cd(file_name)
    for i = 1:length(aoa)
        M = [];
        M = (dlmread(['aoa_' num2str(aoa(i)) '_h_101' ]));
```

```
        FX_system_inertia(i,1) = mean(M(:,1));
        FY_system_inertia(i,1) = mean(M(:,2));
        FZ_system_inertia(i,1) = mean(M(:,3));
        MX_system_inertia(i,1) = mean(M(:,4));
        MY_system_inertia(i,1) = mean(M(:,5));
        MZ_system_inertia(i,1) = mean(M(:,6));

        FX_system_inertia_rms(i,1) = std(M(:,1));
        FY_system_inertia_rms(i,1) = std(M(:,2));
        FZ_system_inertia_rms(i,1) = std(M(:,3));
        MX_system_inertia_rms(i,1) = std(M(:,4));
        MY_system_inertia_rms(i,1) = std(M(:,5));
        MZ_system_inertia_rms(i,1) = std(M(:,6));

    end
    fz_refinement_sw = 0;
    temp = mean(dlmread('temp.txt'));
    [Re, nu,mu, rho] = Re_calc(temp,c,0);
    eval(['temp_model_tooling_' num2str(0) 'per=temp;']);
    eval(['Re_tooling_' num2str(0) 'per=Re;']);
    cd('../../../../..')

    %% MODEL + TOOLING, AERO + INERTIA
    file_name = [fold_name '\Results\' num2str(fan_speed)
'per\DW_results\'];

    cd(file_name)
    for i = 1:length(aoa)
        M = [];
        if exist(['aoa_' num2str(aoa(i)) '_h_101' ]) ~= 0
            M = (dlmread(['aoa_' num2str(aoa(i)) '_h_101' ]));


            %SRS-----------------------
            if aoa(i)==22
            Msrs = [(0:1/10000:(length(M)-1)*1/10000)' M(:,3)-
mean(M(:,3))*0]; % Plot Fz in SRS
            end
            %SRS----------------------

            FX_system_inertia_aero(i,1) = mean(M(:,1));
            FY_system_inertia_aero(i,1) = mean(M(:,2));
            FZ_system_inertia_aero(i,1) = mean(M(:,3));
            MX_system_inertia_aero(i,1) = mean(M(:,4));
            MY_system_inertia_aero(i,1) = mean(M(:,5));
            MZ_system_inertia_aero(i,1) = mean(M(:,6));

            FX_system_inertia_aero_rms(i,1) = std(M(:,1));
            FY_system_inertia_aero_rms(i,1) = std(M(:,2));
            FZ_system_inertia_aero_rms(i,1) = std(M(:,3));
            MX_system_inertia_aero_rms(i,1) = std(M(:,4));
            MY_system_inertia_aero_rms(i,1) = std(M(:,5));
```

```
            MZ_system_inertia_aero_rms(i,1) = std(M(:,6));

                        if fz_refinement_sw == 1
                            if i == 1   % -10 degree aoa is selected as
the correct one
                                M_refine = (dlmread(['aoa_' num2str(
fz_refine_aoa )]));
                                fx1 = mean(M_refine(:,1));
                                clear M_refine
                            end
                            if aoa(i)~= fz_refine_aoa
                                aoa_var = aoa(i) - fz_refine_aoa;
                                fx2 = mean(M(:,1));
                                FZ_system_inertia_aero(i,1) =
FZ_refinement(aoa_var,fx1,fx2);
                            end
                        end
        else
            FX_system_inertia_aero(i,1) = NaN;
            FY_system_inertia_aero(i,1) = NaN;
            FZ_system_inertia_aero(i,1) = NaN;
            MX_system_inertia_aero(i,1) = NaN;
            MY_system_inertia_aero(i,1) = NaN;
            MZ_system_inertia_aero(i,1) = NaN;

            FX_system_inertia_aero_rms(i,1) = NaN;
            FY_system_inertia_aero_rms(i,1) = NaN;
            FZ_system_inertia_aero_rms(i,1) = NaN;
            MX_system_inertia_aero_rms(i,1) = NaN;
            MY_system_inertia_aero_rms(i,1) = NaN;
            MZ_system_inertia_aero_rms(i,1) = NaN;
        end
    end
    temp = mean(dlmread('temp.txt'));
    [~, ~,mu, rho_global] = Re_calc(temp,c,fan_speed);
    eval(['temp_model_tooling_' num2str(fan_speed) 'per=temp;']);
    eval(['Re_model_tooling_' num2str(fan_speed) 'per=Re;']);

    cd('../../../../..')
    %% TOOLING, INERTIA
    file_name = [fold_name '\Results\' num2str(0)
'per\Tooling_results\'];


    cd(file_name)
    for i = 1:length(aoa)
        M = [];
        M = (dlmread(['aoa_' num2str(aoa(i)) '_h_101' ]));
        %SRS------------------------
        if aoa(i)==24
        Msrs = [[0:1/10000:(length(M)-1)*1/10000]' M(:,3)-mean(M(:,3))];
% Plot Fz in SRS
```

```
        end
        %SRS-----------------------
        FX_tooling_inertia(i,1) = mean(M(:,1));
        FY_tooling_inertia(i,1) = mean(M(:,2));
        FZ_tooling_inertia(i,1) = mean(M(:,3));
        MX_tooling_inertia(i,1) = mean(M(:,4));
        MY_tooling_inertia(i,1) = mean(M(:,5));
        MZ_tooling_inertia(i,1) = mean(M(:,6));

        FX_tooling_inertia_rms(i,1) = std(M(:,1));
        FY_tooling_inertia_rms(i,1) = std(M(:,2));
        FZ_tooling_inertia_rms(i,1) = std(M(:,3));
        MX_tooling_inertia_rms(i,1) = std(M(:,4));
        MY_tooling_inertia_rms(i,1) = std(M(:,5));
        MZ_tooling_inertia_rms(i,1) = std(M(:,6));
        if fz_refinement_sw == 1

            if i == 1   % -10 degree aoa is selected as the correct one
                M_refine = (dlmread(['aoa_' num2str( fz_refine_aoa )]));
                fx1 = mean(M_refine(:,1));
                clear M_refine
            end

            if aoa(i)~= fz_refine_aoa
                aoa_var = aoa(i) - fz_refine_aoa;
                fx2 = mean(M(:,1));
                FZ_tooling_inertia(i,1) = FZ_refinement(aoa_var,fx1,fx2);
            end
        end
    end
    temp = mean(dlmread('temp.txt'));
    [~, nu,mu, rho] = Re_calc(temp,c,0);
    eval(['temp_tooling_' num2str(0) 'per=temp;']);
    eval(['Re_tooling_' num2str(0) 'per=Re;']);
    cd('../../../../..')

    %% TOOLING, AERO + INERTIA
    file_name = [fold_name '\Results\' num2str(fan_speed)
'per\Tooling_results\'];

    cd(file_name)
    for i = 1:length(aoa)
        M = [];
        M = (dlmread(['aoa_' num2str(aoa(i)) '_h_101']));

        FX_tooling_inertia_aero(i,1) = mean(M(:,1));
        FY_tooling_inertia_aero(i,1) = mean(M(:,2));
        FZ_tooling_inertia_aero(i,1) = mean(M(:,3));
        MX_tooling_inertia_aero(i,1) = mean(M(:,4));
        MY_tooling_inertia_aero(i,1) = mean(M(:,5));
        MZ_tooling_inertia_aero(i,1) = mean(M(:,6));

        FX_tooling_inertia_aero_rms(i,1) = std(M(:,1));
```

```
        FY_tooling_inertia_aero_rms(i,1) = std(M(:,2));
        FZ_tooling_inertia_aero_rms(i,1) = std(M(:,3));
        MX_tooling_inertia_aero_rms(i,1) = std(M(:,4));
        MY_tooling_inertia_aero_rms(i,1) = std(M(:,5));
        MZ_tooling_inertia_aero_rms(i,1) = std(M(:,6));

        if fz_refinement_sw == 1

            if i == 1   % -10 degree aoa is selected as the correct one
                M_refine = (dlmread(['aoa_' num2str( fz_refine_aoa )]));
                fx1 = mean(M_refine(:,1));
                clear M_refine
            end

            if aoa(i)~= fz_refine_aoa
                aoa_var = aoa(i) - fz_refine_aoa;
                fx2 = mean(M(:,1));
                FZ_tooling_inertia_aero(i,1) =
FZ_refinement(aoa_var,fx1,fx2);
            end
        end
    end
    temp = mean(dlmread('temp.txt'));
    [Re, nu,mu, rho] = Re_calc(temp,0/1000,0);
    eval(['temp_tooling_' num2str(fan_speed) 'per=temp;']);
    eval(['Re_tooling_' num2str(fan_speed) 'per=Re;']);
    cd('../../../../..')

    % Summary Results
    eval(['temp_model_tooling_' num2str(0) 'per']);
    eval(['temp_model_tooling_' num2str(fan_speed) 'per']);
    eval(['temp_tooling_' num2str(0) 'per']);
    eval(['temp_tooling_' num2str(fan_speed) 'per']);
    eval(['Re_model_tooling_' num2str(fan_speed) 'per']);

    %% AERODYNAMIC LOAD
%%%%%%%%%%%%%%%%%%%%%%%%%%%%%%%%%%%%%%%%%%%%%%%%%%%%%%%%%%%%%%%%%%%%%%%%%%
%%
    % Distances from sensor to bracket trailing edge
    dx = 0; % (m) dx is positive if the point is apart from the sensor in
the drag direction
    dy = -(470)/1000;  % (m) dy is positive if the point is on the
starboard side of the sensor when viewed from the wind tunnel fan
location (-471 mm is the default value)
    dz = -44/1000; % (m)  dz is positive if the point is above the sensor
when viewed from the sidewalls of the tunnel (-29 mm is the default
value)
    dx_strut = 15/1000*0; % (m) dx is positive if the point is apart from
the trailing edge in drag direction (15 is the default value)


    % First Method -----------------------------------------------------
------
```

```
    FX_system_aero = FX_system_inertia_aero - FX_system_inertia;
    FY_system_aero = FY_system_inertia_aero - FY_system_inertia;
    FZ_system_aero = FZ_system_inertia_aero - FZ_system_inertia;
    MX_system_aero = MX_system_inertia_aero - MX_system_inertia;
    MY_system_aero = MY_system_inertia_aero - MY_system_inertia;
    MZ_system_aero = MZ_system_inertia_aero - MZ_system_inertia;

    FX_tooling_aero = FX_tooling_inertia_aero - FX_tooling_inertia;
    FY_tooling_aero = FY_tooling_inertia_aero - FY_tooling_inertia;
    FZ_tooling_aero = FZ_tooling_inertia_aero - FZ_tooling_inertia;
    MX_tooling_aero = MX_tooling_inertia_aero - MX_tooling_inertia;
    MY_tooling_aero = MY_tooling_inertia_aero - MY_tooling_inertia;
    MZ_tooling_aero = MZ_tooling_inertia_aero - MZ_tooling_inertia;

    FX = FX_system_aero - FX_tooling_aero;
    FY = FY_system_aero - FY_tooling_aero;
    FZ = FZ_system_aero - FZ_tooling_aero;
    MX = MX_system_aero - MX_tooling_aero;
    MY = MY_system_aero - MY_tooling_aero;
    MZ = MZ_system_aero - MZ_tooling_aero;
    mean_FY=mean(FY);
    mean_MX=mean(MX);
    mean_MY=mean(MY);
    mean_MZ=mean(MZ);
    fprintf('MX= %s \n',mean_MX);
    fprintf('MY= %s \n',mean_MY);
    fprintf('MZ= %s \n',mean_MZ);
    fprintf('FY= %s \n',mean_FY);
    % First Method ------------------------------------------------------
------


    % %%% AOA shift  %%% -------------------------------------------------
--------
    % % AOA arrangement
    aoa_plot_final=(aoa+aoa_shift);
    aoa_rad = aoa_plot_final*pi/180;
    % %%% AOA shift  %%% -------------------------------------------------
--------


    % Second Method -----------------------------------------------------
-------
    FX_model_aero_inertia = FX_system_inertia_aero -
FX_tooling_inertia_aero;
    FY_model_aero_inertia = FY_system_inertia_aero -
FY_tooling_inertia_aero;
    FZ_model_aero_inertia = FZ_system_inertia_aero -
FZ_tooling_inertia_aero;
    MX_model_aero_inertia = MX_system_inertia_aero -
MX_tooling_inertia_aero;
    MY_model_aero_inertia = MY_system_inertia_aero -
MY_tooling_inertia_aero;
```

```
    MZ_model_aero_inertia = MZ_system_inertia_aero -
MZ_tooling_inertia_aero;

    FX_model_inertia = FX_system_inertia - FX_tooling_inertia;
    FY_model_inertia = FY_system_inertia - FY_tooling_inertia;
    FZ_model_inertia = FZ_system_inertia - FZ_tooling_inertia;
    MX_model_inertia = MX_system_inertia - MX_tooling_inertia;
    MY_model_inertia = MY_system_inertia - MY_tooling_inertia;
    MZ_model_inertia = MZ_system_inertia - MZ_tooling_inertia;

    FX = FX_model_aero_inertia - FX_model_inertia;
    FY = FY_model_aero_inertia - FY_model_inertia;
    FZ = FZ_model_aero_inertia - FZ_model_inertia;
    MX = MX_model_aero_inertia - MX_model_inertia;
    MY = MY_model_aero_inertia - MY_model_inertia;
    MZ = MZ_model_aero_inertia - MZ_model_inertia;
    % Second Method ----------------------------------------------------
------

    % BODY TO WIND FRAME Forces and Moments

    [FX_w,FZ_w] = body2wind(FX,FZ,aoa_rad); % Drag and Lift Forces (N)
    FY_w =  - (FY); % Side force

    [MX_w_sensor,MZ_w_sensor] = body2wind(MX,MZ,aoa_rad); % Roll and Yaw
Moments (N)
    MY_w_sensor =  - ( MY); % Pitch Moment (Nm)

    MX_w = (+FY_w*dz - FZ_w*dy) + MX_w_sensor;
    MY_w = (-FX_w*dz + FZ_w*dx) + MY_w_sensor;
    MZ_w = (+FX_w*dy - FY_w*dx) + MZ_w_sensor;

    % Pressure Center
    x_p = ( - MY_w_sensor + FX_w*dz) ./ FZ_w; % (m) Pressure center in
pitch  x_p is positive if the point is apart from the sensor in drag
direction

    % WIND FRAME Coefficients
    rho = rho_global; % kg/m^3

    V = interp1(fan_per_map,power_per_map,fan_speed_Vcalc); %
Interpolation for tunnel map


    dyn_press = 1/2*rho*V^2;

    C_D = FX_w/(dyn_press*A);
    C_Y = FY_w/(dyn_press*A);
    C_L = FZ_w/(dyn_press*A);

    C_R = MX_w/(dyn_press*A*c);

    % Define the moment reference point
```

```
    x_ref =  c/1000;  % Moment reference point is at the trailing edge

    % Assuming the original moment is calculated at x_0 (initial
reference point)
    x_0 = 0;  % The original reference point at the apex

    % Adjust the pitching moment to the new reference point
    M_y = MY_w + FZ_w * (x_ref - x_0);

    % Calculate the pitching moment coefficient with the new reference
point
    C_M = M_y / (dyn_press * A * c);

    C_N = MZ_w/(dyn_press*A*c);

    CL_CD = C_L./C_D;

    high_ind = find(aoa_plot_final==aoa_greater);
    l_ind = find(aoa_plot_final==aoa_lower);

    % Original Loads and Aerodynamic Center in pitch  -------------------
-----------------
    CL_alpha = ( C_L(high_ind) - C_L(l_ind) ) / (
aoa_plot_final(high_ind) - aoa_plot_final(l_ind) );
    CM_alpha = ( C_M(high_ind) - C_M(l_ind) ) / (
aoa_plot_final(high_ind) - aoa_plot_final(l_ind) );
    X_a = (dx_strut + c)/c - CM_alpha/CL_alpha; % measured location is
normalized by the chord length. It is defined from the apex therefore c
distance is added.
    fprintf('X_a= %s \n',X_a);

%%%%%%%%%%%%%%%%%%%%%%%%%%%%%%%%%%%%%%%%%%%%%%%%%%%%%%%%%%%%%%%%%%%%%%%%%
%%
    %%%%%%%%%%%%%%%%%%%%%%%% Derived Loads Methodology
%%%%%%%%%%%%%%%%%%%%%%%%

%%%%%%%%%%%%%%%%%%%%%%%%%%%%%%%%%%%%%%%%%%%%%%%%%%%%%%%%%%%%%%%%%%%%%%%%%
%%

    % Derived Loads and Aerodynamic Center ------------------------------
------
    FX_derived   = MZ/ (+dy);
    FY_derived   = zeros(size(FX_derived));
    FZ_derived   = MX/ (-dy);

    [FX_w_derived,FZ_w_derived] =
body2wind(FX_derived,FZ_derived,aoa_rad); % Derived Drag and Lift Forces
(N)
    FY_w_derived =  - (FY_derived); % Derived Side force

    % % % % % FZ_w_derived = FZ_w_derived - (FZ_w_derived(aoa_rad==0)); %
This line has to be commented. It stands for equating the lift value to
zero at zero angle of attack
```

```
    MX_w_derived =  (+FY_w_derived*dz - FZ_w_derived*dy) + MX_w_sensor;
    MY_w_derived =  (-FX_w_derived*dz + FZ_w_derived*dx) + MY_w_sensor;
    MZ_w_derived =  (+FX_w_derived*dy - FY_w_derived*dx) + MZ_w_sensor;

    % Double Check
    expression_tobe_zero = MY + FX_derived * dz + MY_w_derived;  % This
expression should be zero, My_b_sensor = Fx_b * (-dz) + (My_b)_model

    C_D_derived = FX_w_derived/(dyn_press*A);
    C_Y_derived = FY_w_derived/(dyn_press*A);
    C_L_derived = FZ_w_derived/(dyn_press*A);
    C_R_derived = MX_w_derived/(dyn_press*A*c);

    M_y_derived = MY_w_derived + FZ_w_derived * (x_ref - x_0);

    % Calculate the pitching moment coefficient with the new reference
point
    C_M_derived = M_y_derived / (dyn_press * A * c);

    C_N_derived = MZ_w_derived/(dyn_press*A*c);

    CL_CD_derived = C_L_derived./C_D_derived;
    x_p_derived = ( - MY_w_sensor + FX_w_derived*dz ) ./ FZ_w_derived; %
(m) Pressure center in pitch  x_p is positive if the point is apart from
the sensor in drag direction

    % Derived Loads and Aerodynamic Center in pitch  --------------------
----------------
    CL_alpha_derived = ( C_L_derived(high_ind) - C_L_derived(l_ind) ) / (
aoa_plot_final(high_ind) - aoa_plot_final(l_ind) );
    CM_alpha_derived = ( C_M_derived(high_ind) - C_M_derived(l_ind) ) / (
aoa_plot_final(high_ind) - aoa_plot_final(l_ind) );
    X_a_derived = (dx_strut + c)/c - CM_alpha_derived/CL_alpha_derived; %
measured location is normalized by the chord length. It is defined from
the apex; therefore c distance is added.

%%%%%%%%%%%%%%%%%%%%%%%%%%%%%%%%%%%%%%%%%%%%%%%%%%%%%%%%%%%%%%%%%%%%%%%%%
%%
    %%%%%%%%%%%%%%%%%%%% ------------------------------
%%%%%%%%%%%%%%%%%%%%%%%

%%%%%%%%%%%%%%%%%%%%%%%%%%%%%%%%%%%%%%%%%%%%%%%%%%%%%%%%%%%%%%%%%%%%%%%%%
%%


    % Auxillary plots ---------------------------------------------------
------
    % The mass of the tooling
    FX_b_1 = FX_tooling_inertia;
    FZ_b_1 = FZ_tooling_inertia;
    [FX_w_1,FZ_w_1] = body2wind(FX_b_1,FZ_b_1,aoa_rad);
```

```
    % The mass and aerodynamic of the tooling
    FX_b_234 = FX_tooling_inertia_aero;
    FZ_b_234 = FZ_tooling_inertia_aero;
    [FX_w_234,FZ_w_234] = body2wind(FX_b_234,FZ_b_234,aoa_rad);

    % The mass of the system
    FX_b_5 = FX_system_inertia;
    FZ_b_5 = FZ_system_inertia;
    [FX_w_5,FZ_w_5] = body2wind(FX_b_5,FZ_b_5,aoa_rad);

    % The mass and aerodynamic of the system
    FX_b_678 = FX_system_inertia_aero;
    FZ_b_678 = FZ_system_inertia_aero;
    [FX_w_678,FZ_w_678] = body2wind(FX_b_678,FZ_b_678,aoa_rad);

    % The aerodynamic of the wing
    [FX_w_91011,FZ_w_91011] = body2wind((FX_b_678-FX_b_234) - (FX_b_5-
FX_b_1), (FZ_b_678-FZ_b_234) - (FZ_b_5-FZ_b_1),aoa_rad);
    % %%%%%%%%%%%%%%%%%%%%%%%% NEW APPROACH FOR
UNCERTAINTY%%%%%%%%%%%%%%%%%%%%%%%%%%%%%%%%%%%%%%%%%%%%%%%
    % [FX_w_91011,FZ_w_91011] = body2wind((FX_b_678-FX_b_234) -
FX_model_inertia_v2, (FZ_b_678-FZ_b_234) - FZ_model_inertia_v2,aoa_rad);


    % The aerodynamic coefficients of the wing
    C_D_121314 = FX_w_91011/(dyn_press*A);
    C_L_121314 = FZ_w_91011/(dyn_press*A);
    CL_CD_121314 = C_L_121314./C_D_121314;



%%%%%%%%%%%%%%%%%%%%%%%%%%%%%%%%%%%%%%%%%%%%%%%%%%%%%%%%%%%%%%%%%%%%%%%%%
%%
    %%%%%%%%%%%%%%%%%%%% Derived plots for paper format
%%%%%%%%%%%%%%%%%%%%%%%

%%%%%%%%%%%%%%%%%%%%%%%%%%%%%%%%%%%%%%%%%%%%%%%%%%%%%%%%%%%%%%%%%%%%%%%%%
%%
    % The mass of the tooling
    FX_b_1_derived = MZ_tooling_inertia/ (+dy);
    FZ_b_1_derived = MX_tooling_inertia/ (-dy);
    [FX_w_1_derived,FZ_w_1_derived] =
body2wind(FX_b_1_derived,FZ_b_1_derived,aoa_rad);

    % The mass and aerodynamic of the tooling
    FX_b_234_derived = MZ_tooling_inertia_aero/ (+dy);
    FZ_b_234_derived = MX_tooling_inertia_aero/ (-dy);
    [FX_w_234_derived,FZ_w_234_derived] =
body2wind(FX_b_234_derived,FZ_b_234_derived,aoa_rad);

    % The mass of the system
    FX_b_5_derived = MZ_system_inertia/ (+dy);
    FZ_b_5_derived = MX_system_inertia/ (-dy);
```

```
    [FX_w_5_derived,FZ_w_5_derived] =
body2wind(FX_b_5_derived,FZ_b_5_derived,aoa_rad);

    % The mass and aerodynamic of the system
    FX_b_678_derived = MZ_system_inertia_aero/ (+dy);
    FZ_b_678_derived = MX_system_inertia_aero/ (-dy);
    [FX_w_678_derived,FZ_w_678_derived] =
body2wind(FX_b_678_derived,FZ_b_678_derived,aoa_rad);

    % The aerodynamic of the wing
    [FX_w_91011_derived,FZ_w_91011_derived] = ...
        body2wind((FX_b_678_derived-FX_b_234_derived) - ...
        (FX_b_5_derived-FX_b_1_derived), (FZ_b_678_derived-
FZ_b_234_derived)...
        - (FZ_b_5_derived-FZ_b_1_derived),aoa_rad);

    % The aerodynamic coefficients of the wing
    C_D_121314_derived = FX_w_91011_derived/(dyn_press*A);
    C_L_121314_derived = FZ_w_91011_derived/(dyn_press*A);
    CL_CD_121314_derived = C_L_121314_derived./C_D_121314_derived;

    % Auxillary plots calculation ends here -----------------------------
------

       %%
    % PLOTTING ----------------------------------------------------------
------
    % There is no calculation in this section.


    %%
    % -------------------- Auxillary Plots ------------------------------
------
    if fan_speed == 20
        plot_index = [2 6 9 12];
    elseif fan_speed == 25
        plot_index = [3 7 10 13];
    elseif fan_speed == 30
        plot_index = [4 8 11 14];
    elseif fan_speed == 40
        plot_index = [2 6 9 12];
    end



    CD_map     = C_D_121314;
    CL_map     = C_L_121314;
    CL2CD_map = CL_CD_121314;
    CM_map     = C_M;

    CD_derived_map     = C_D_121314_derived;
    CL_derived_map     = C_L_121314_derived;
```

```
    CL2CD_derived_map = CL_CD_121314_derived;
    CM_derived_map     = C_M_derived;

    X_a_map = X_a;
    X_a_derived_map = X_a_derived;
    X_p_map = x_p;
    X_p_derived_map = x_p_derived;

    FX_system_inertia_aero_rms_map = FX_system_inertia_aero_rms;
    FZ_system_inertia_aero_rms_map = FZ_system_inertia_aero_rms;
    MX_system_inertia_aero_rms_map = MX_system_inertia_aero_rms;
    MY_system_inertia_aero_rms_map = MY_system_inertia_aero_rms;
    MZ_system_inertia_aero_rms_map = MZ_system_inertia_aero_rms;



file_savename = [folder_name '\' fold_name '\Results\'];


cd(file_savename)
% Saving the RMS results1
figHandles = findobj('Type','figure');
for i = 1:length(figHandles)
    savefig(figure(i),[num2str(i) '.fig' ])
end
cd(folder_name)
%%
   close all


% %% h charts on the legend data vs AOA
%%%%%%%%%%%%%%%%%%%%%%%%%%%%%%%%%%
figure;
set(gcf, 'units', 'normalized', 'outerposition', [0.1 -0.1 0.75 0.75 *
1.8 * 0.68])
ha33 = tight_subplot(2, 2, [.08 .07], [.08 .01], [.2 .2]);


    % Plot C_D vs AOA
    axes(ha33(1));
    %plot(aoa_plot_final, CD_map, ['--' markers{marker_index}(2)],
'Color', color_map_h(color_index, :));
    plot(aoa_plot_final, CD_derived_map, 'Marker', plot_marker, 'Color',
plot_color ,'LineWidth',1.5); ylabel('C_D', 'Rotation', 0);
    hold on;
    grid on;
    set(gca, 'GridLineStyle', '-');
    set(gca, 'GridColor', [0.15,0.15,0.15]);
    set(gca, 'GridAlpha', 0.15);
    set(gca, 'GridLineWidth', 0.5);
    hold on;
    legend(wing_name, 'Location', 'northwest');
```

```
    % Plot C_L vs AOA
    axes(ha33(3));
    % plot(aoa_plot_final, CL_map, ['--' markers{marker_index}(2)],
'Color', color_map_h(color_index, :));
    plot(aoa_plot_final, CL_derived_map, 'Marker', plot_marker, 'Color',
plot_color ,'LineWidth',1.5); ylabel('C_L', 'Rotation', 0);
xlabel('\alpha (degree)');
    hold on;
    grid on;
    set(gca, 'GridLineStyle', '-');
    set(gca, 'GridColor', [0.15,0.15,0.15]);
    set(gca, 'GridAlpha', 0.15);
    set(gca, 'GridLineWidth', 0.5);
    hold on;

    % Plot C_M vs AOA
    axes(ha33(2));
    % plot(aoa_plot_final, CM_map, ['--' markers{marker_index}(2)],
'Color', color_map_h(color_index, :));
    plot(aoa_plot_final, CM_derived_map, 'Marker', plot_marker, 'Color',
plot_color ,'LineWidth',1.5); ylabel('C_M', 'Rotation', 0);
    hold on;
    grid on;
    set(gca, 'GridLineStyle', '-');
    set(gca, 'GridColor', [0.15,0.15,0.15]);
    set(gca, 'GridAlpha', 0.15);
    set(gca, 'GridLineWidth', 0.5);
    hold on;

    % Plot C_L / C_D vs AOA
    axes(ha33(4));
    % plot(aoa_plot_final, CL2CD_map, ['--' markers{marker_index}(2)],
'Color', color_map_h(color_index, :));
    plot(aoa_plot_final, CL2CD_derived_map, 'Marker', plot_marker,
'Color', plot_color ,'LineWidth',1.5); ylabel('C_L / C_D', 'Rotation',
0); xlabel('\alpha (degree)');
    hold on;
    grid on;
    set(gca, 'GridLineStyle', '-');
    set(gca, 'GridColor', [0.15,0.15,0.15]);
    set(gca, 'GridAlpha', 0.15);
    set(gca, 'GridLineWidth', 0.5);
    hold on;

hold on;

% Save aerodynamic data
save([wing_name '_aero_data.mat'], 'MX', 'MY', 'MZ', 'dy', 'dyn_press',
'aoa_plot_final', 'A', 'c');

% Subfunctions
```

```
function Fz_refined = FZ_refinement(aoa_var,fx1,fx2)
% X axis static balance refinement
% aoa_var = delta aoa from the initial fx value aoa
% if initial -10 aoa fx value is accepted as correct one, -8 aoa Fz value
% will be defined with aoa_var = 2 since -8 - (-10)



if aoa_var == 0   % Take precaution with respect to aoa == 0
    Fz_refined_upper = tand(90 - (+2)) * (fx2 - fx1);
    Fz_refined_lower = tand(90 - (-2)) * (fx2 - fx1);
    Fz_refined = mean([Fz_refined_upper,Fz_refined_lower ]);
else
    Fz_refined       = tand(90 - (aoa_var)) * (fx2 - fx1);
end
end


function [FX_wind_frame,FZ_wind_frame] =
body2wind(FX_body_frame,FZ_bodyframe,aoa_rad)
FX_wind_frame =  + ( FX_body_frame.* cos(aoa_rad) - FZ_bodyframe.*
sin(aoa_rad) ); % Drag (N)
FZ_wind_frame =  - ( FX_body_frame.* sin(aoa_rad) + FZ_bodyframe.*
cos(aoa_rad) ); % Lift (N)


end
```

Appendix B

OUT-OF-GROUND EFFECT PRESSURE COEFFICIENT CALCULATIONS SOURCE CODE

```
folder_name = 'C:\Users\CASPER\Desktop\Thesis';
cd(folder_name)
addpath(folder_name)

c = 135/1000; % Wing chord length in meters
fan_speed = 40; % Fan speed for file reading
aoa = -2:2:30; % Angle of attack range
csv_col = 11; % Number of columns in the CSV files of the experiments
(depends on the wing)

prompt7 = 'What is the AoA protractor?: ';
aoa_protractor = input(prompt7);
aoa_shift = -aoa_protractor - 2;
aoa_plot_final = (aoa + aoa_shift);

y_to_S = [0.207407407, 0.281481481, 0.355555556, 0.42962963, 0.503703704,
0.577777778, 0.651851852, 0.725925926, 0.8]; % Pressure port locations

% Pre-allocations for data storage
N = cell(length(aoa), 1);
M = cell(length(aoa), 1);
C = cell(length(aoa), 1);
Cp_map = cell(length(aoa), 1);
P_dyn_map = cell(length(aoa), 1);

% Results folder name
fold_name = 'All Over\Pressure_Results_Base_LS_GE';
wing_name = 'Base';
%colors = [
'#000000','#FF4D00','#FF0000','#0000FF','#660066','#008000','#003333'];
%wing names [Base,S-λ3φ05,S-λ2φ05,S-λ2φ03,S-λ1φ02,ST-λ2φ05,ST-λ2φ03];
%markers = ['o','+','square','^','x','diamond','*'];
plot_color = '#000000';
plot_marker = 'o';

% Loop for noise data processing
for i = 1:length(aoa)
    file_name = [fold_name '\Results\' num2str(fan_speed) 'per\noise\'];
    cd(file_name)

    % Initialize matrix for noise data
    A = zeros(1, csv_col);

    % Check if file exists for the specified angle of attack
```

```
    if exist(['aoa_' num2str(aoa(i)) '_h_101_noise_1_Stream1.csv']) ~= 0
        % Average noise data from the single available file
        A = (mean(readmatrix(['aoa_' num2str(aoa(i))
'_h_101_noise_1_Stream1.csv'])) + ...
             mean(readmatrix(['aoa_' num2str(aoa(i))
'_h_101_noise_2_Stream1.csv'])) + ...
             mean(readmatrix(['aoa_' num2str(aoa(i))
'_h_101_noise_3_Stream1.csv'])))/3;
    end

    N{i} = A;
    cd('../../../../..')
end

% Loop for measured data processing
for i = 1:length(aoa)
    file_name = [fold_name '\Results\' num2str(fan_speed)
'per\measured_data\'];
    cd(file_name)

    % Initialize matrix for measured data
    B = zeros(1, csv_col);

    % Check if file exists for the specified angle of attack
    if exist(['aoa_' num2str(aoa(i)) '_h_101_1_Stream1.csv']) ~= 0
        % Average measured data from the available file
        B = (mean(readmatrix(['aoa_' num2str(aoa(i))
'_h_101_1_Stream1.csv'])) + ...
             mean(readmatrix(['aoa_' num2str(aoa(i))
'_h_101_2_Stream1.csv'])) + ...
             mean(readmatrix(['aoa_' num2str(aoa(i))
'_h_101_3_Stream1.csv'])))/3;
    end

    M{i} = B;
    cd('../../../../..')
end

% Subtract noise from the measured data
for i = 1:length(aoa)
    C{i} = M{i} - N{i};
end

% Cp calculator and plotter
for i = 1:length(aoa)
    C_mat = C{i};

    % Extract Cp values
    P = C_mat(1:end-2);
    P_static = C_mat(end-1);
    P_total = C_mat(end);
    P_dyn = P_total - P_static;
    Cp = (P - P_static) / P_dyn;
```

```
    Cp_map{i} = Cp;
    P_dyn_map{i} = P_dyn;

    % Plot Cp values
    figure(i)
    plot(y_to_S, -Cp, '-', 'Marker', plot_marker, 'Color', plot_color,
'LineWidth', 1);
    hold on

    grid on
    title(['\alpha = ' num2str(aoa_plot_final(i)) '°'])
    xlabel('y/s');
    xlim([0 1]);
    ylim([-0.4, 1.4]);
    ylabel('-C_p');
    legend(wing_name);
end

% Save pressure data
save([wing_name '_cp_data.mat'], 'aoa_plot_final','P', 'P_dyn',
'P_static', 'P_total');
```

Appendix C

ABSOLUTE UNCERTAINTY LEVELS OF FORCE MEASUREMENTS

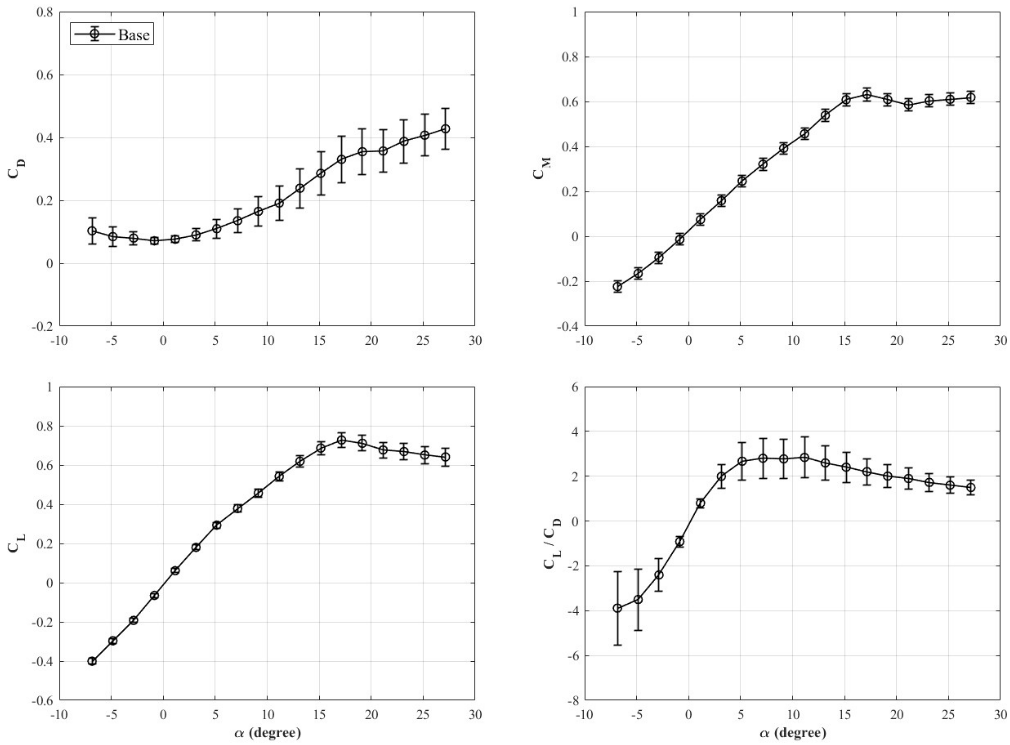

Figure C - 1 Absolute uncertainty levels of drag coefficient (C_D), lift coefficient (C_L), moment coefficient (C_M), and the lift-to-drag ratio (C_L/C_D) for the base wing model.

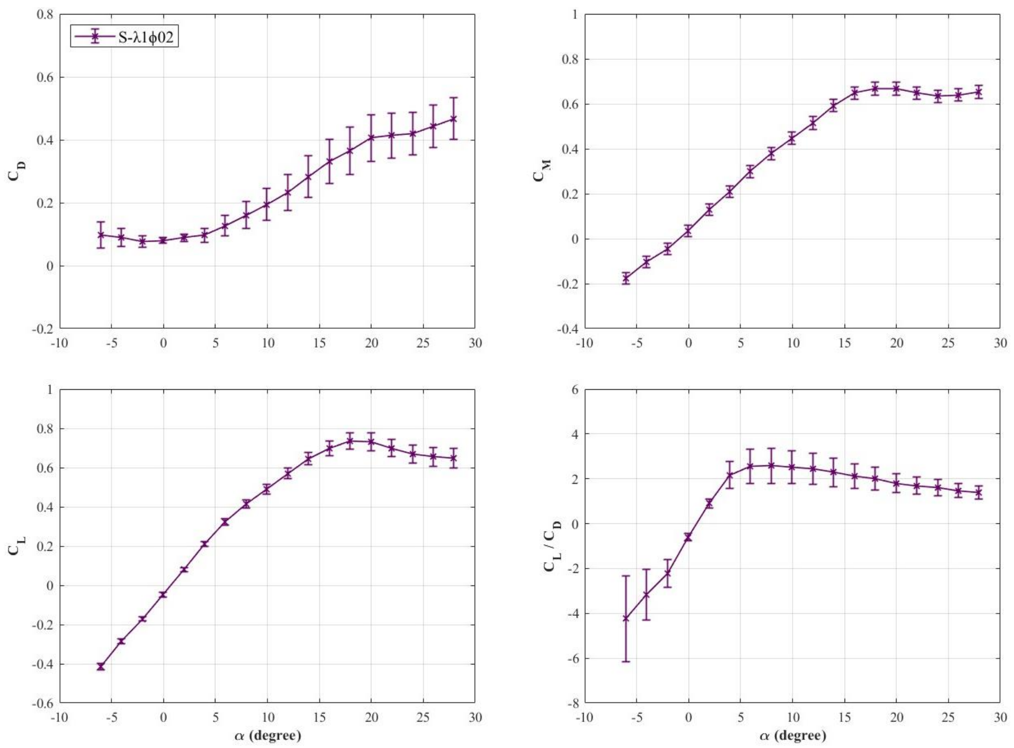

Figure C - 2 Absolute uncertainty levels of drag coefficient (C_D), lift coefficient (C_L), moment coefficient (C_M), and the lift-to-drag ratio (C_L/C_D) for the S-λ1ϕ02 wing model.

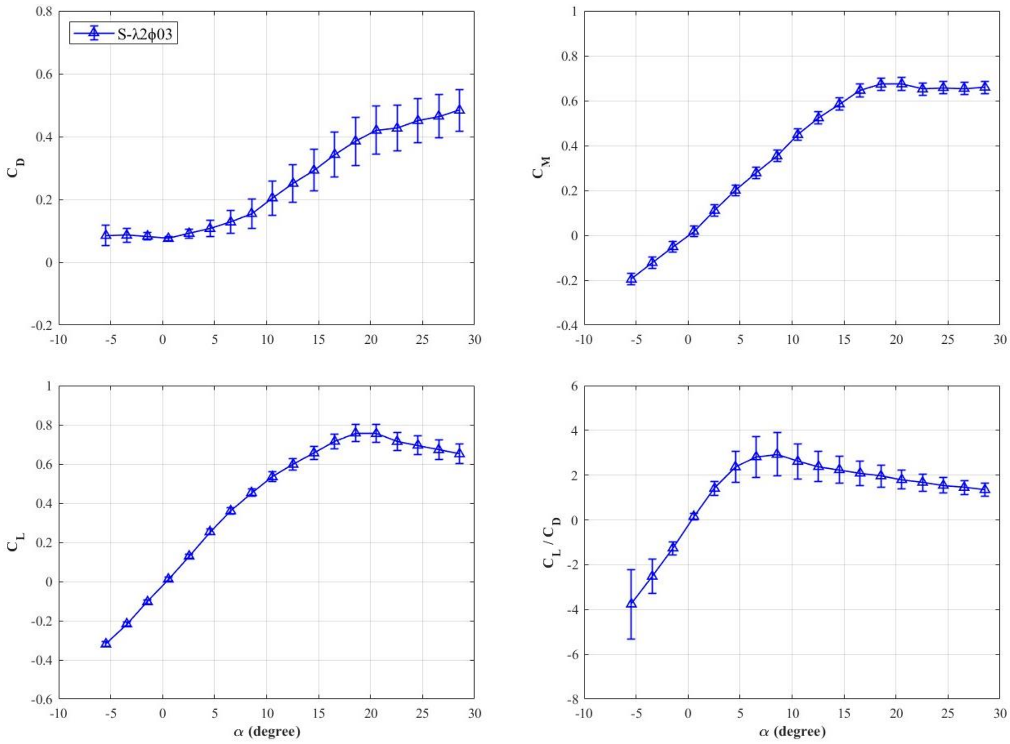

Figure C - 3 Absolute uncertainty levels of drag coefficient (C_D), lift coefficient (C_L), moment coefficient (C_M), and the lift-to-drag ratio (C_L/C_D) for the S-λ2ϕ03 wing model.

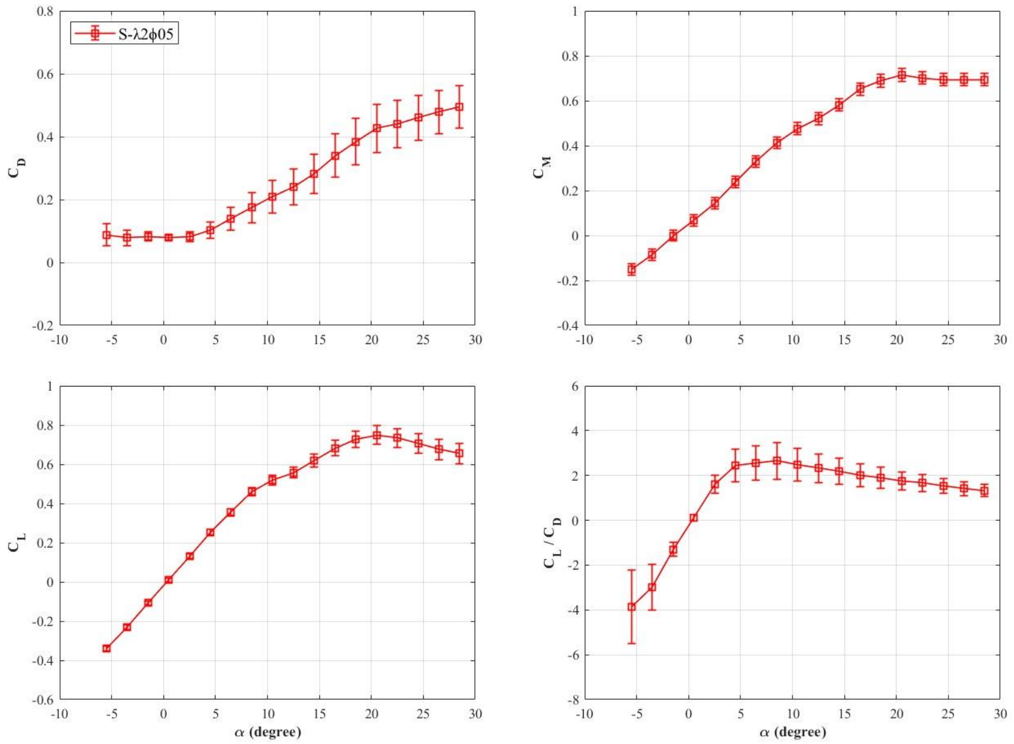

Figure C - 4 Absolute uncertainty levels of drag coefficient (C_D), lift coefficient (C_L), moment coefficient (C_M), and the lift-to-drag ratio (C_L/C_D) for the S-λ2ϕ05 wing model.

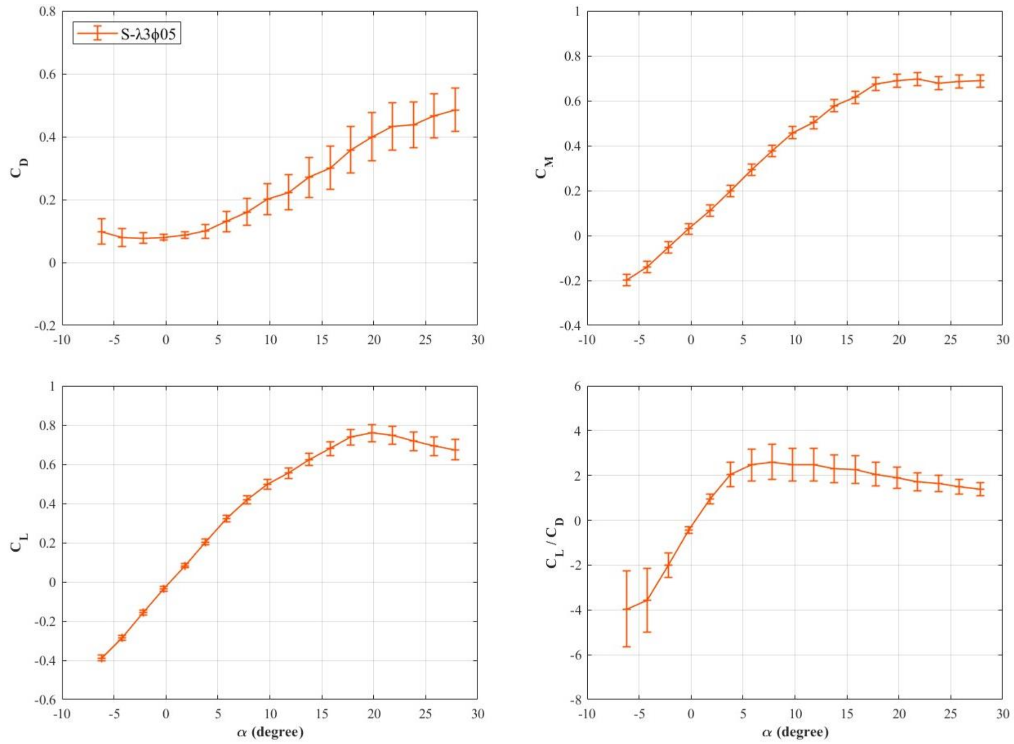

Figure C - 5 Absolute uncertainty levels of drag coefficient (C_D), lift coefficient (C_L), moment coefficient (C_M), and the lift-to-drag ratio (C_L/C_D) for the S-λ3ϕ05 wing model.

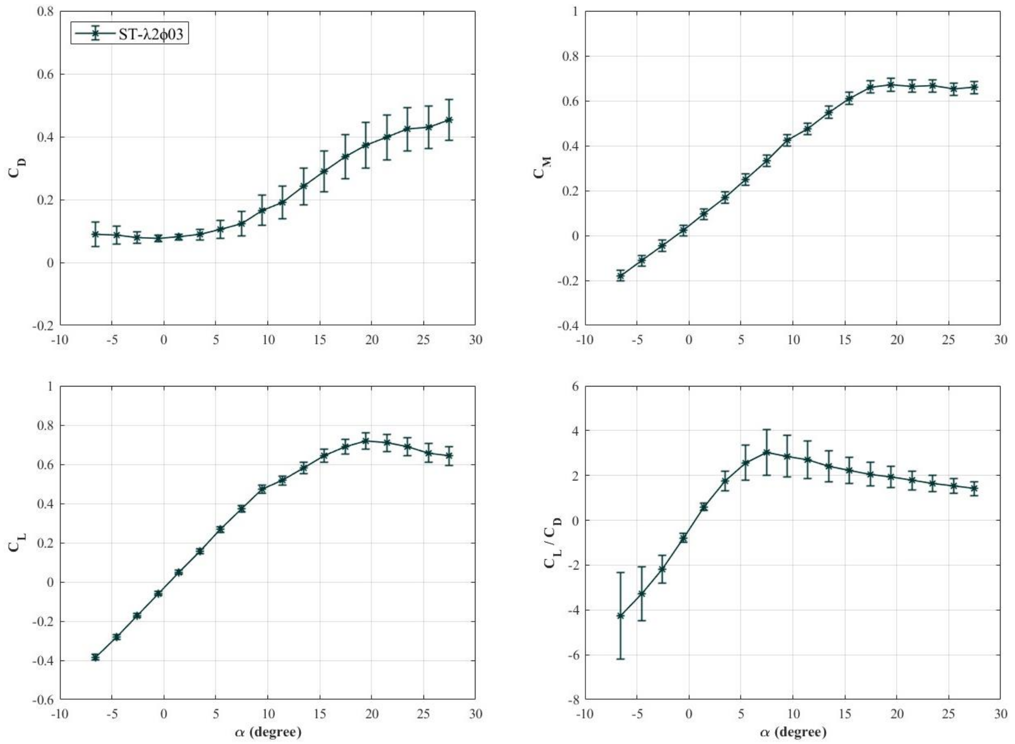

Figure C - 6 Absolute uncertainty levels of drag coefficient (C_D), lift coefficient (C_L), moment coefficient (C_M), and the lift-to-drag ratio (C_L/C_D) for the ST-λ2ϕ03 wing model.

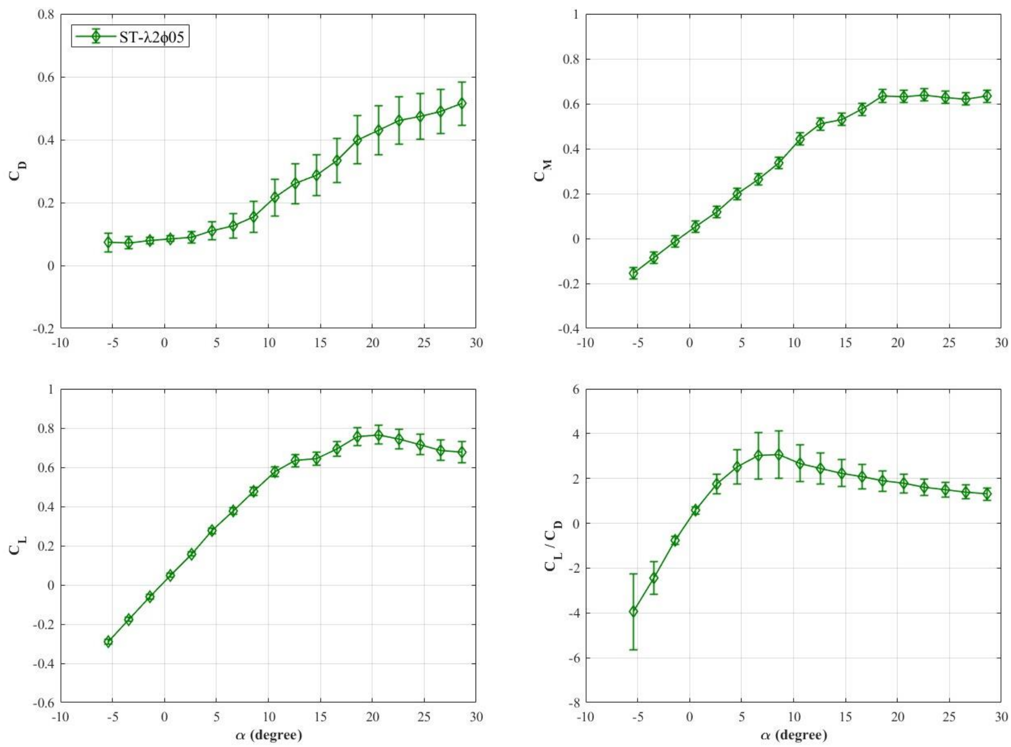

Figure C - 7 Absolute uncertainty levels of drag coefficient (C_D), lift coefficient (C_L), moment coefficient (C_M), and the lift-to-drag ratio (C_L/C_D) for the ST-λ2ϕ05 wing model.

Appendix D

STATIC GROUND EFFECT FORCE MEASUREMENT RESULTS

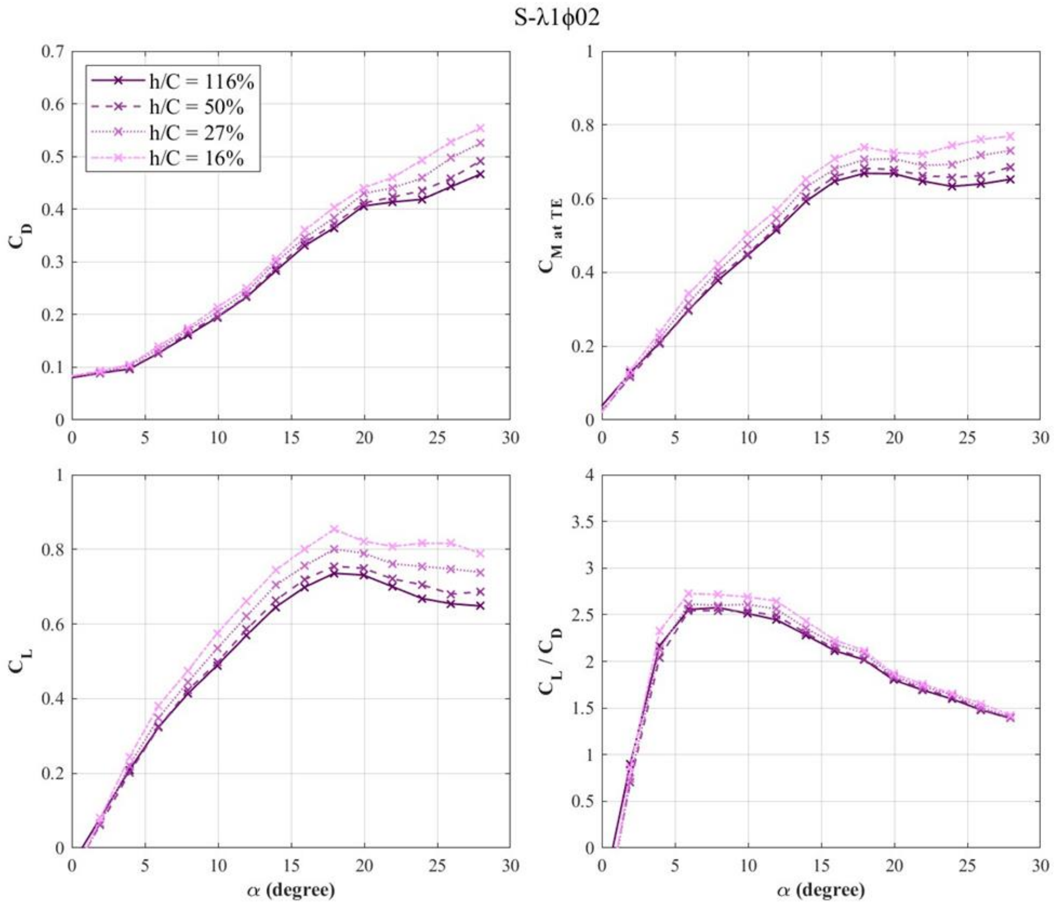

Figure D - 1 Drag coefficient (C_D), lift coefficient (C_L), moment coefficient (C_M), and the lift-to-drag ratio (C_L/C_D) at various ground clearances and angles of attack for S-λ1ϕ02 wing model.

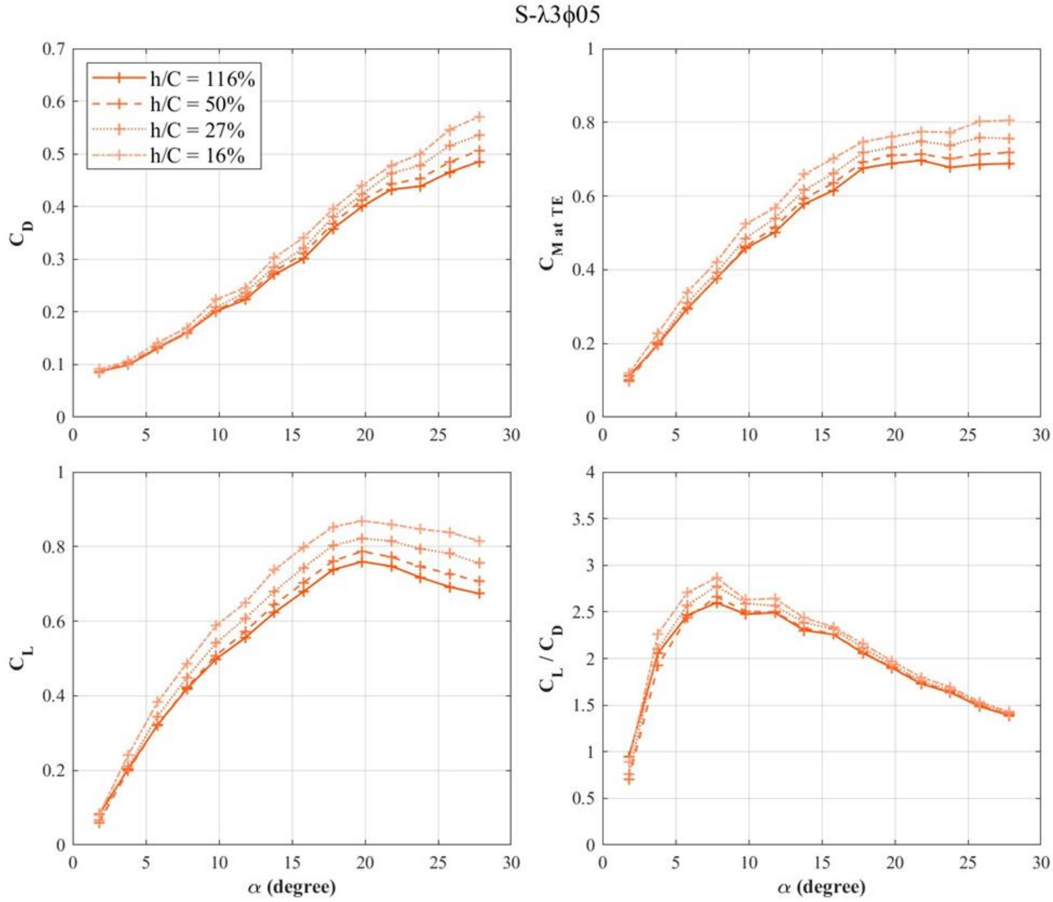

Figure D - 2 Drag coefficient (C_D), lift coefficient (C_L), moment coefficient (C_M), and the lift-to-drag ratio (C_L/C_D) at various ground clearances and angles of attack for S-λ3ϕ05 wing model.

ST-λ2ϕ03

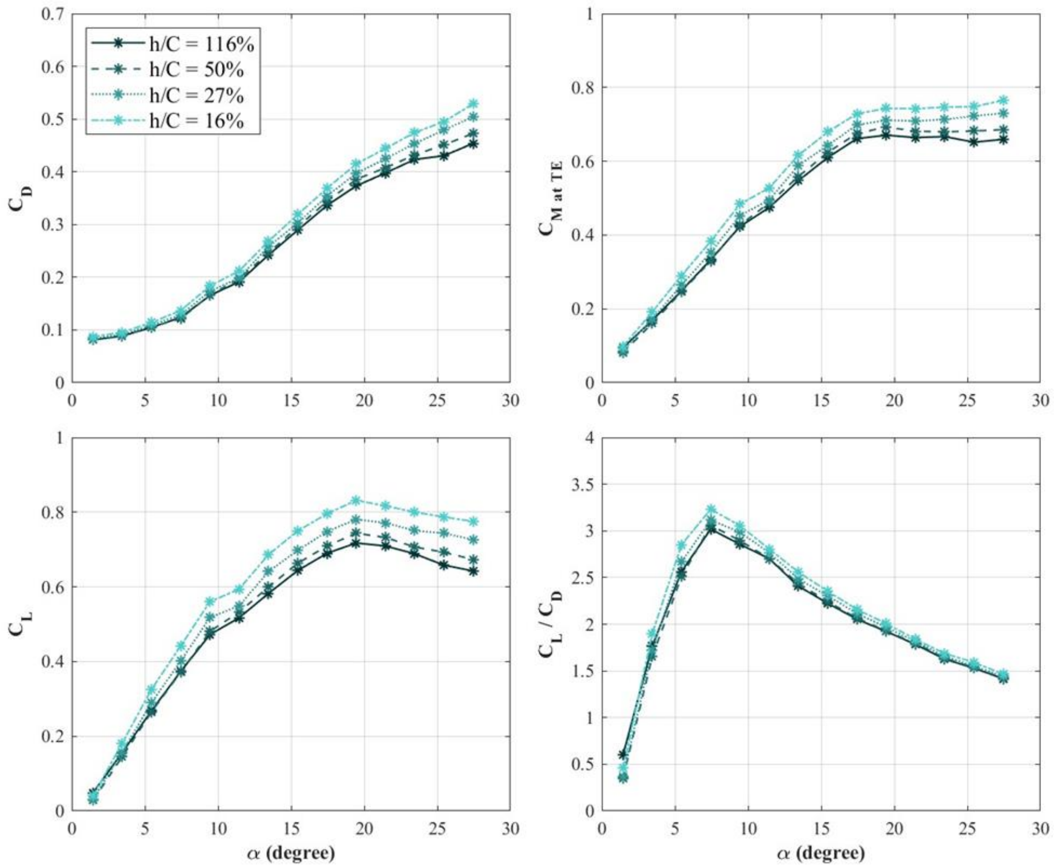

Figure D - 3 Drag coefficient (C_D), lift coefficient (C_L), moment coefficient (C_M), and the lift-to-drag ratio (C_L/C_D) at various ground clearances and angles of attack for ST-λ2ϕ03 wing model.

Appendix E

STATIC GROUND EFFECT PRESSURE MEASUREMENT RESULTS

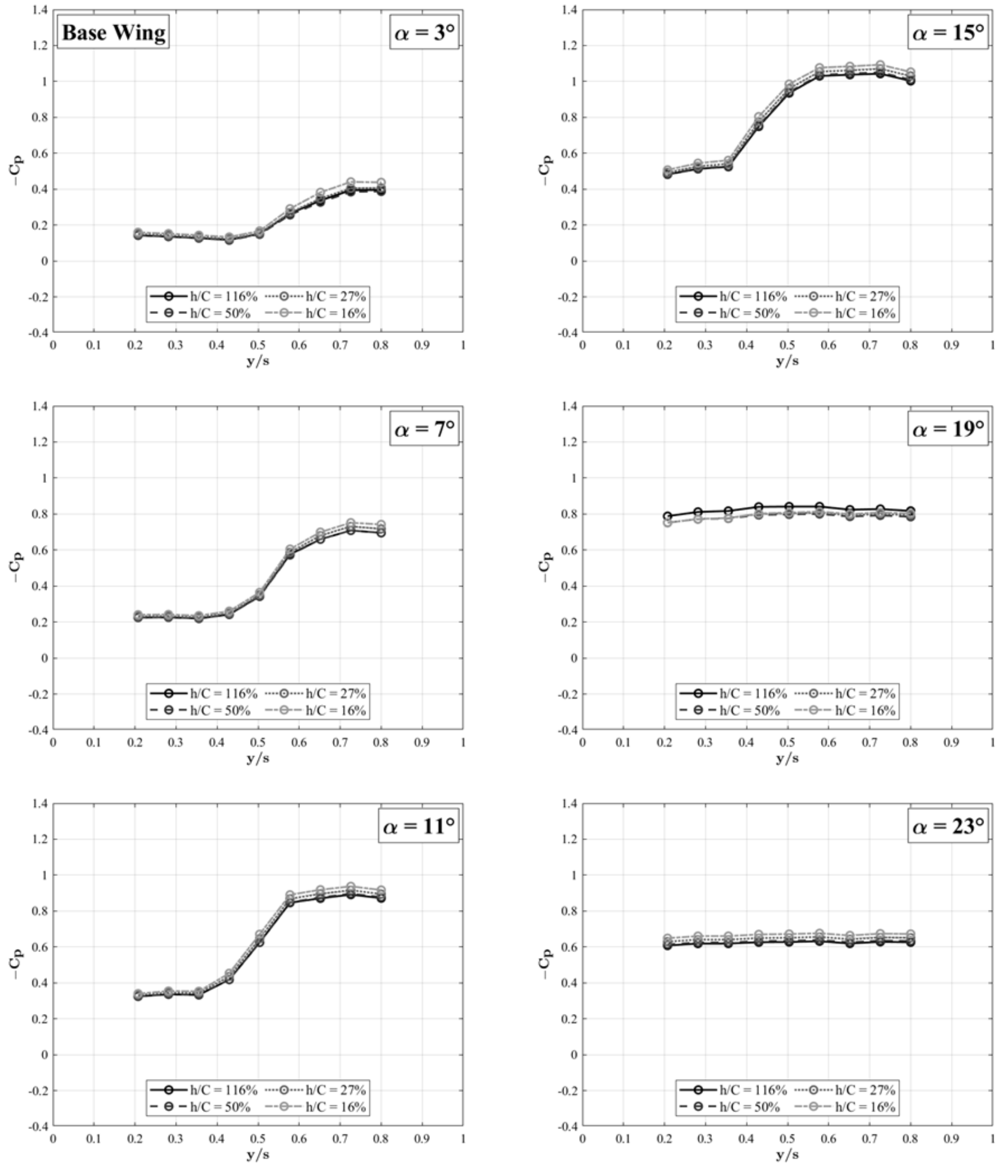

Figure E - 1 Distribution of pressure coefficient at various angles of attack and height-to-chord ratios for base wing model on half span at $x/C = 0.5$.

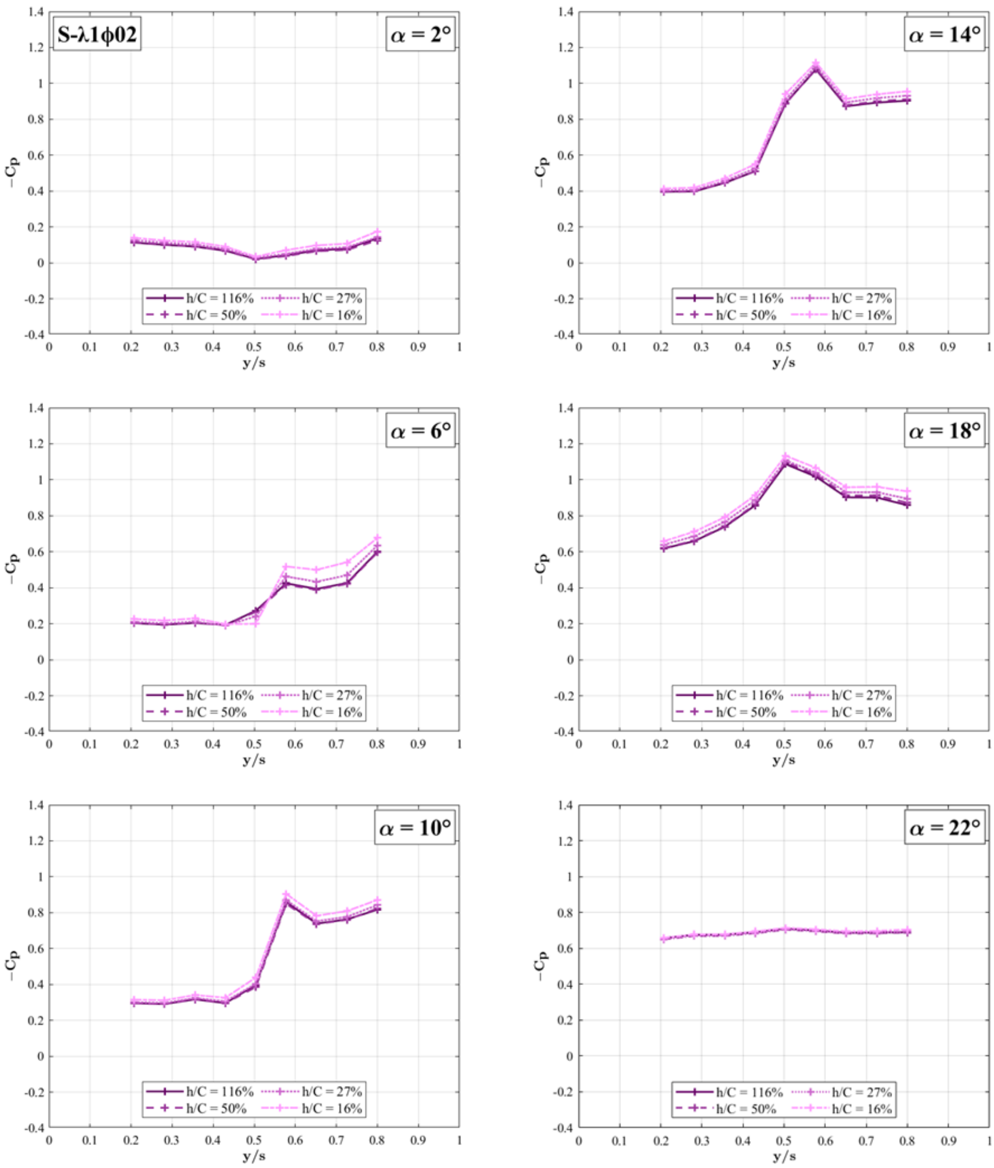

Figure E - 2 Distribution of pressure coefficient at various angles of attack and height-to-chord ratios for S-λ1ϕ02 wing model on half span at $x/C = 0.5$.

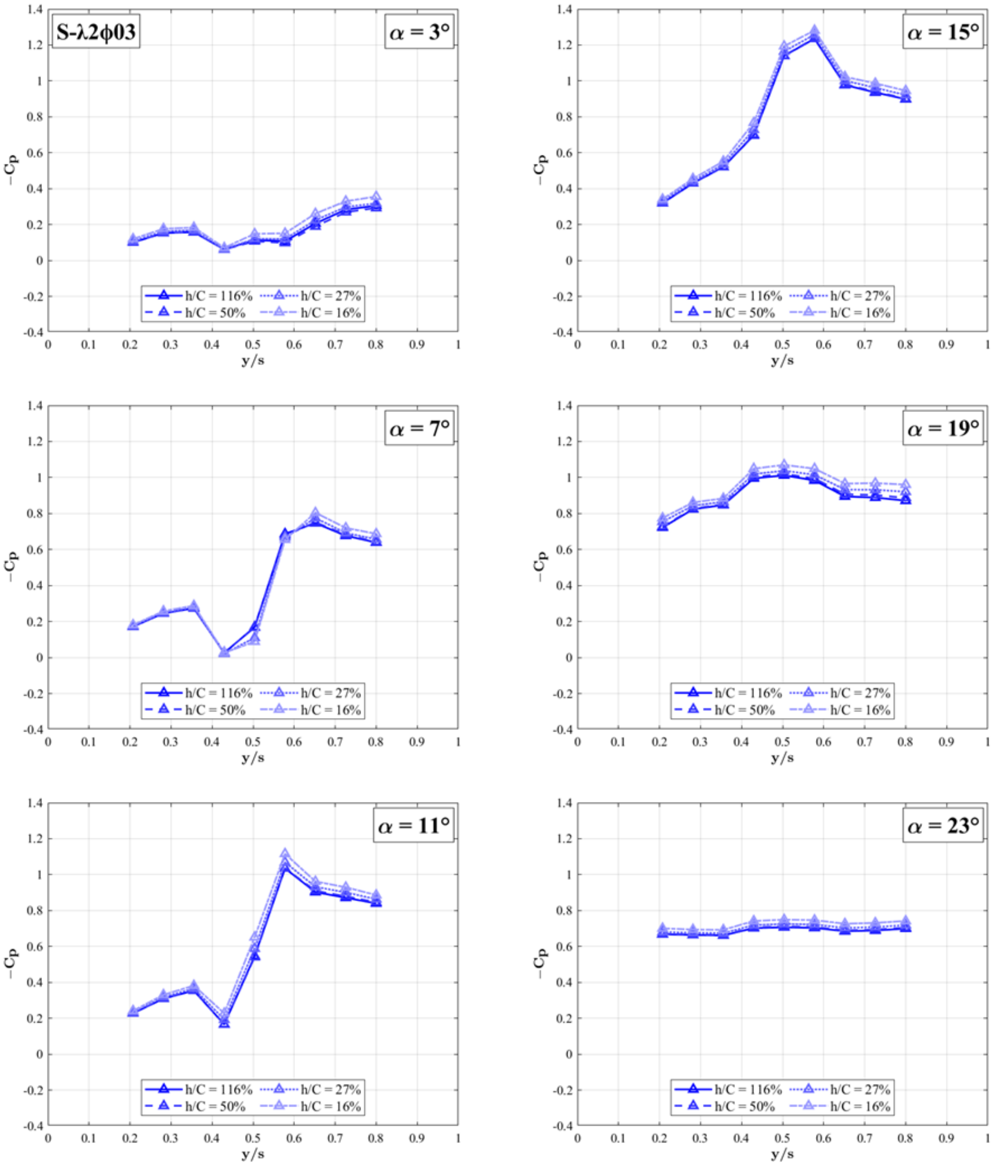

Figure E - 3 Distribution of pressure coefficient at various angles of attack and height-to-chord ratios for S-λ2ϕ03 wing model on half span at $x/C = 0.5$.

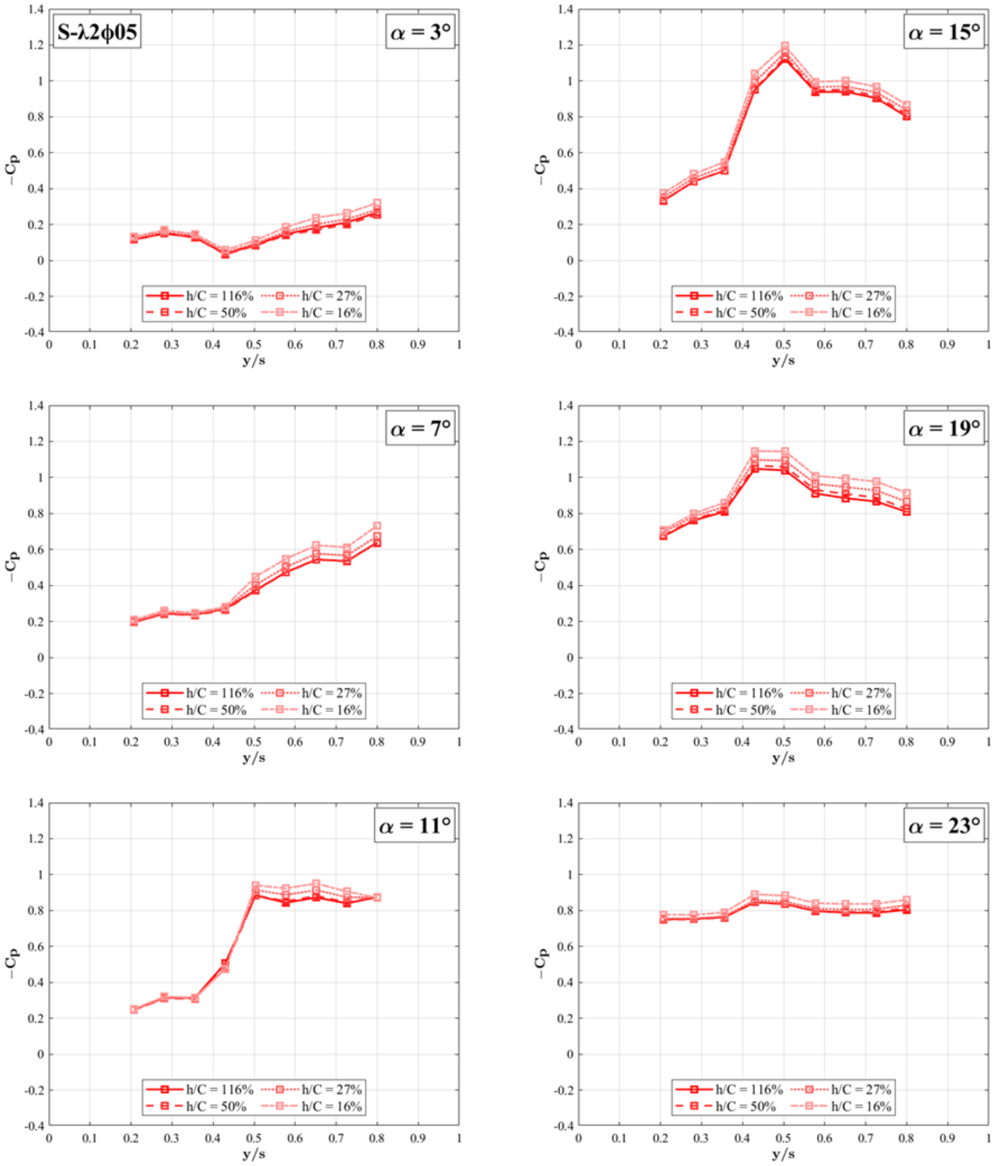

Figure E - 4 Distribution of pressure coefficient at various angles of attack and height-to-chord ratios for S-λ2ϕ05 wing model on half span at $x/C = 0.5$.

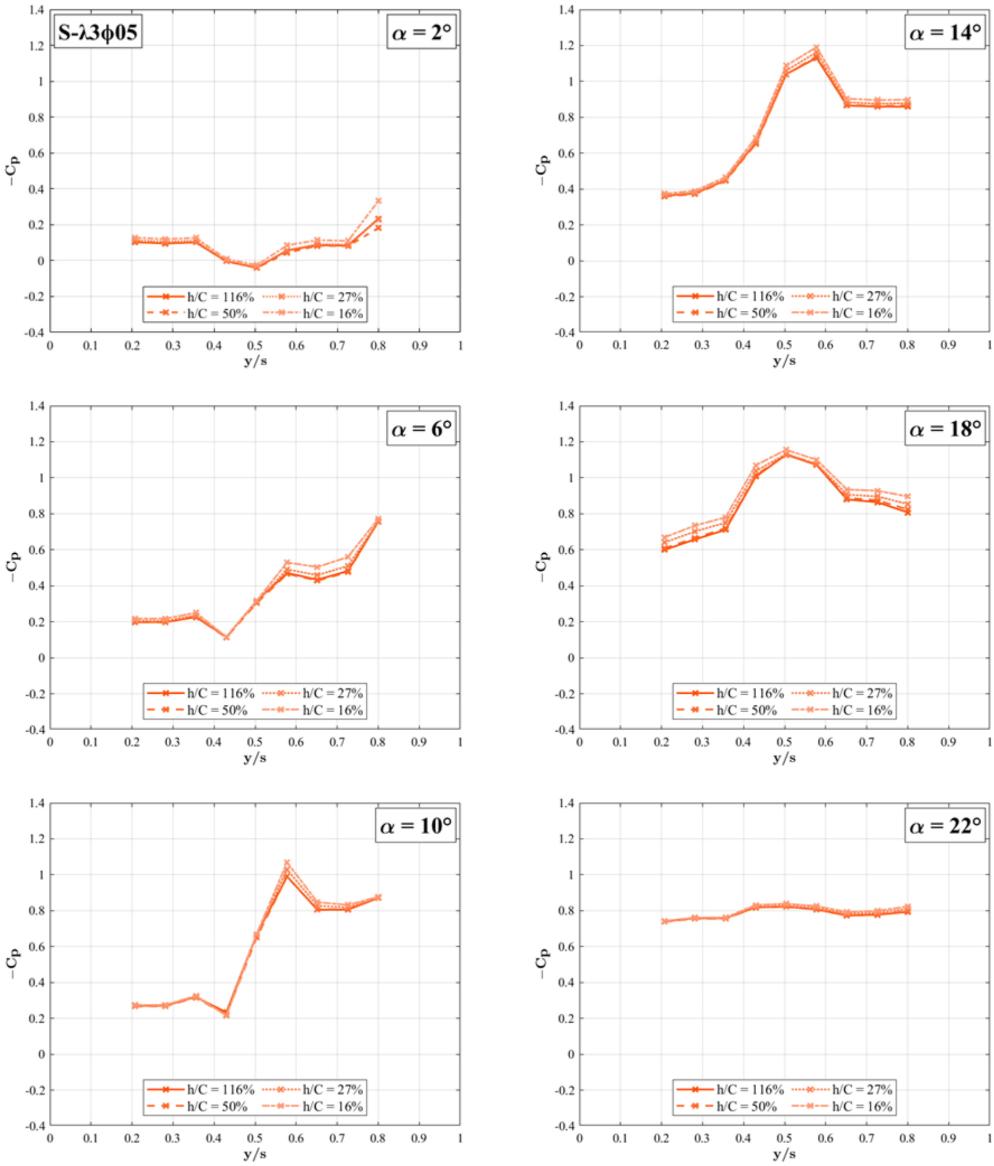

Figure E - 5 Distribution of pressure coefficient at various angles of attack and height-to-chord ratios for S-λ3ϕ05 wing model on half span at $x/C = 0.5$.

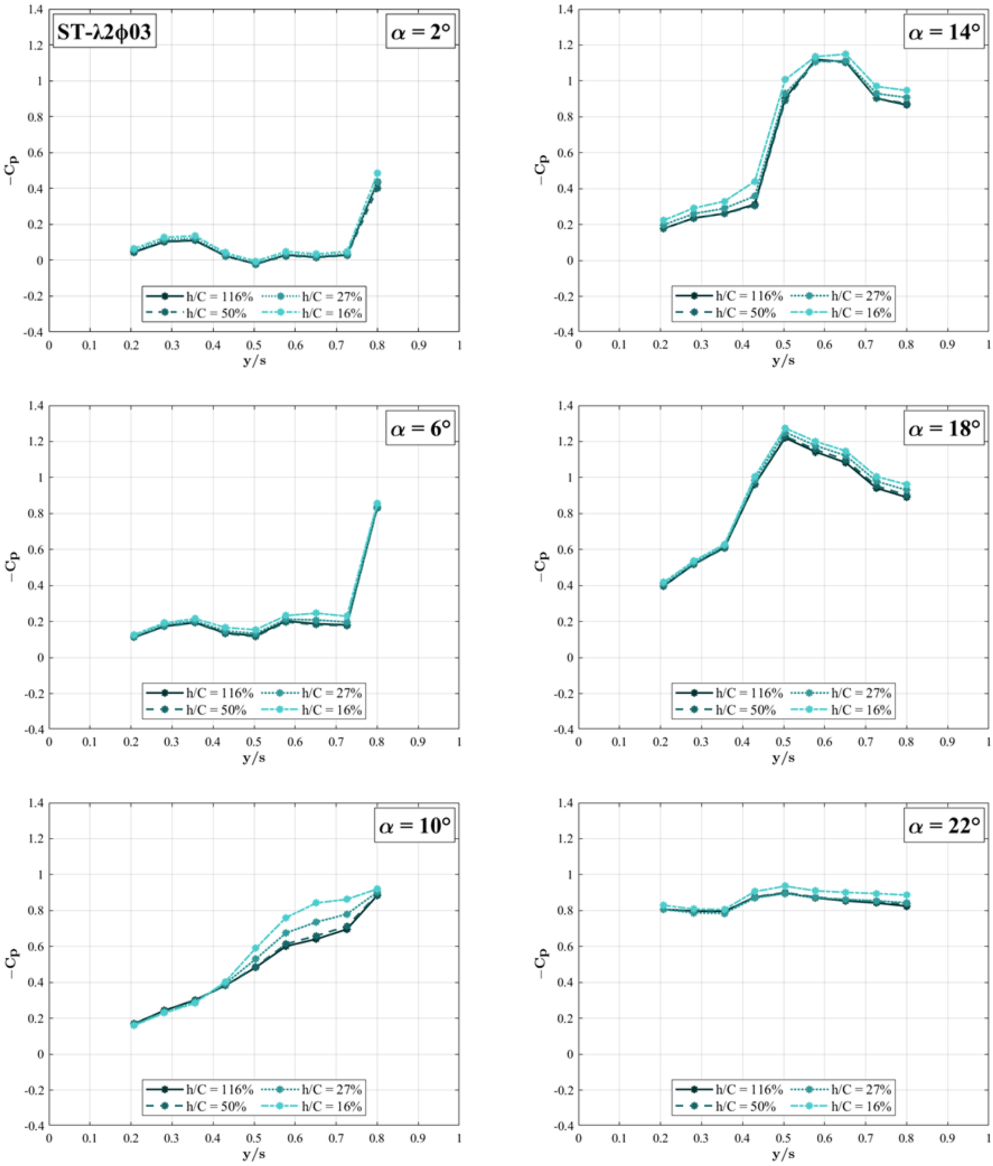

Figure E - 6 Distribution of pressure coefficient at various angles of attack and height-to-chord ratios for ST-λ2ϕ03 wing model on half span at $x/C = 0.5$.

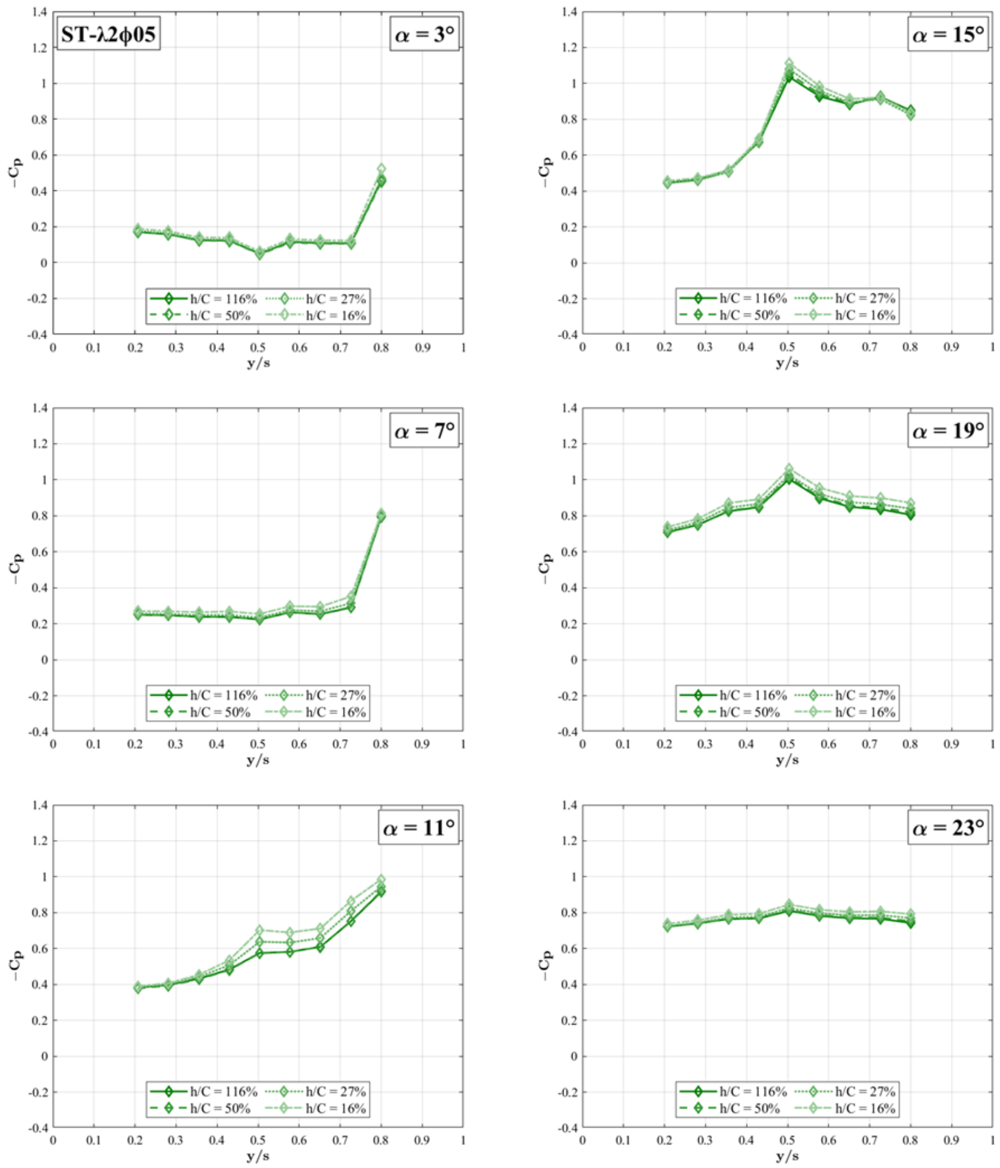

Figure E - 7 Distribution of pressure coefficient at various angles of attack and height-to-chord ratios for ST-λ2ϕ05 wing model on half span at $x/C = 0.5$.

Appendix F

VECTOR FIELDS AND VELOCITY CONTOURS OF PIV MEASUREMENTS

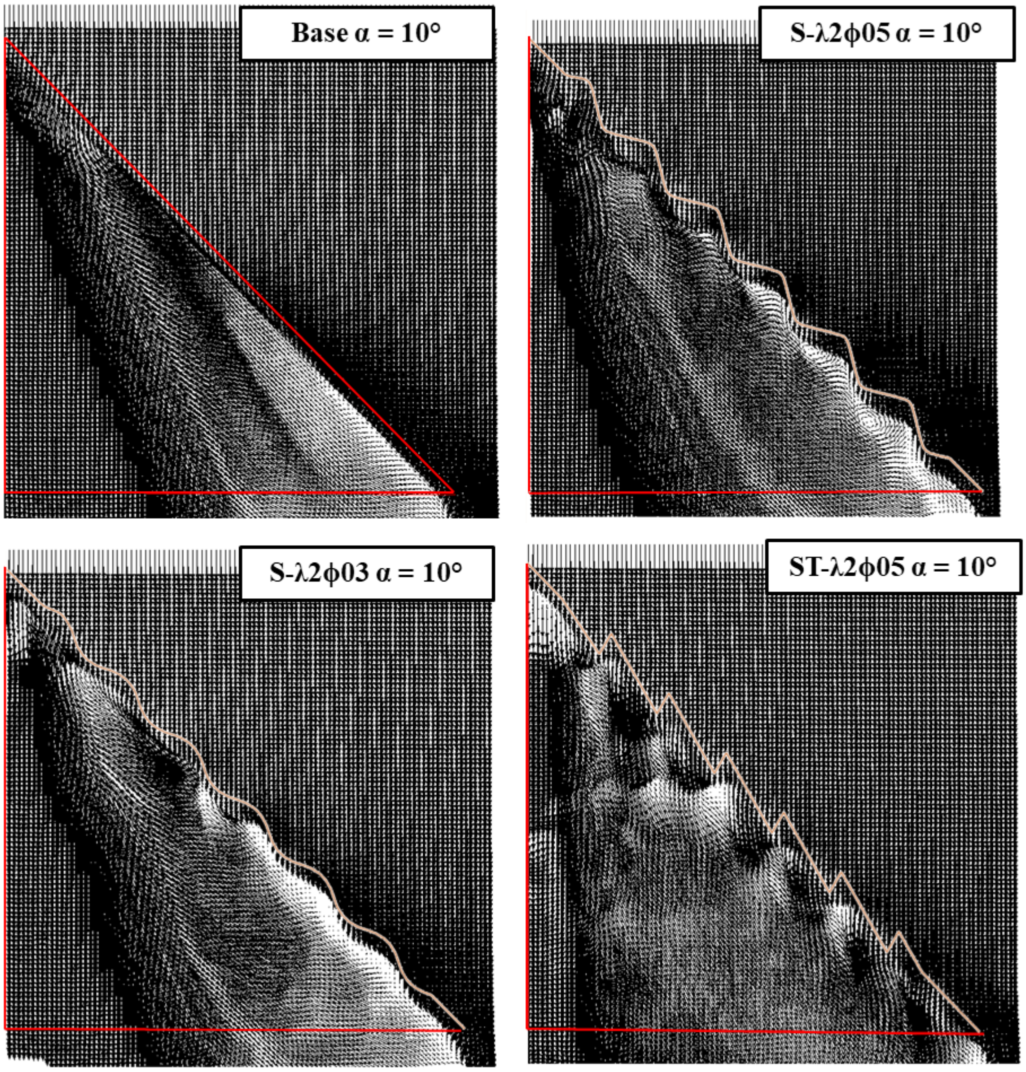

Figure F - 1 Vector fields of base, S-λ2ϕ03, S-λ2ϕ05, and ST-λ2ϕ05 wing models at $\alpha = 10°$.

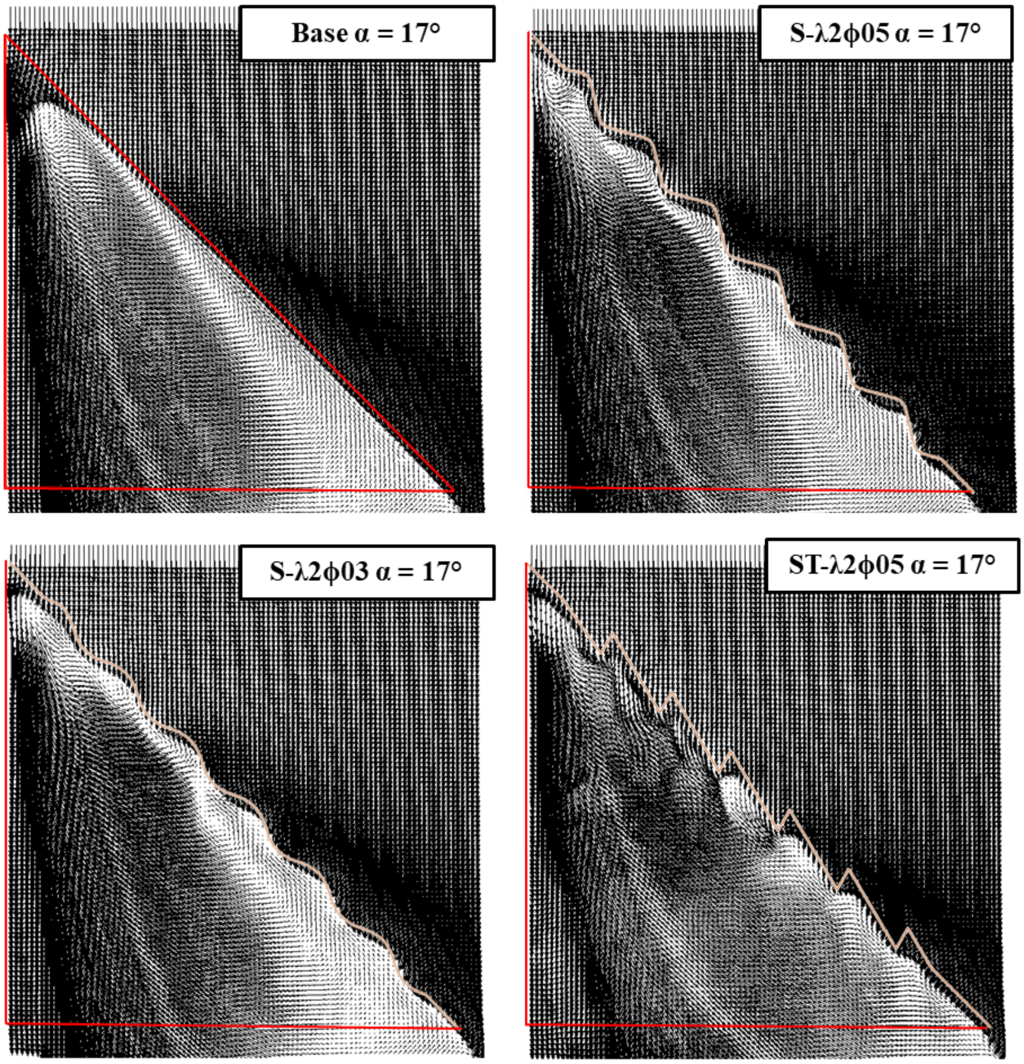

Figure F - 2 Vector fields of base, S-λ2ϕ03, S-λ2ϕ05, and ST-λ2ϕ05 wing models at $\alpha = 17°$.

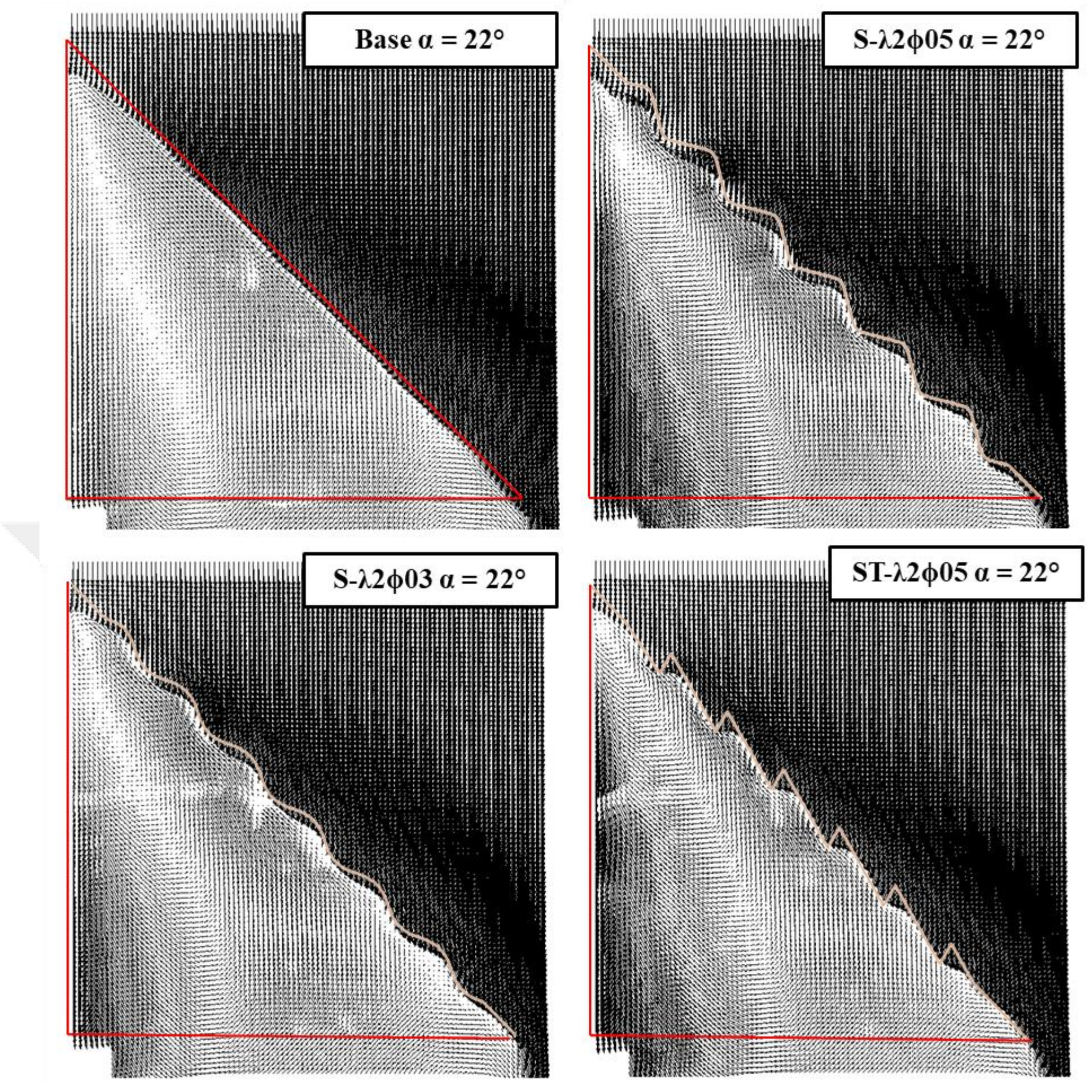

Figure F - 3 Vector fields of base, S-λ2ϕ03, S-λ2ϕ05, and ST-λ2ϕ05 wing models at $\alpha = 22°$.

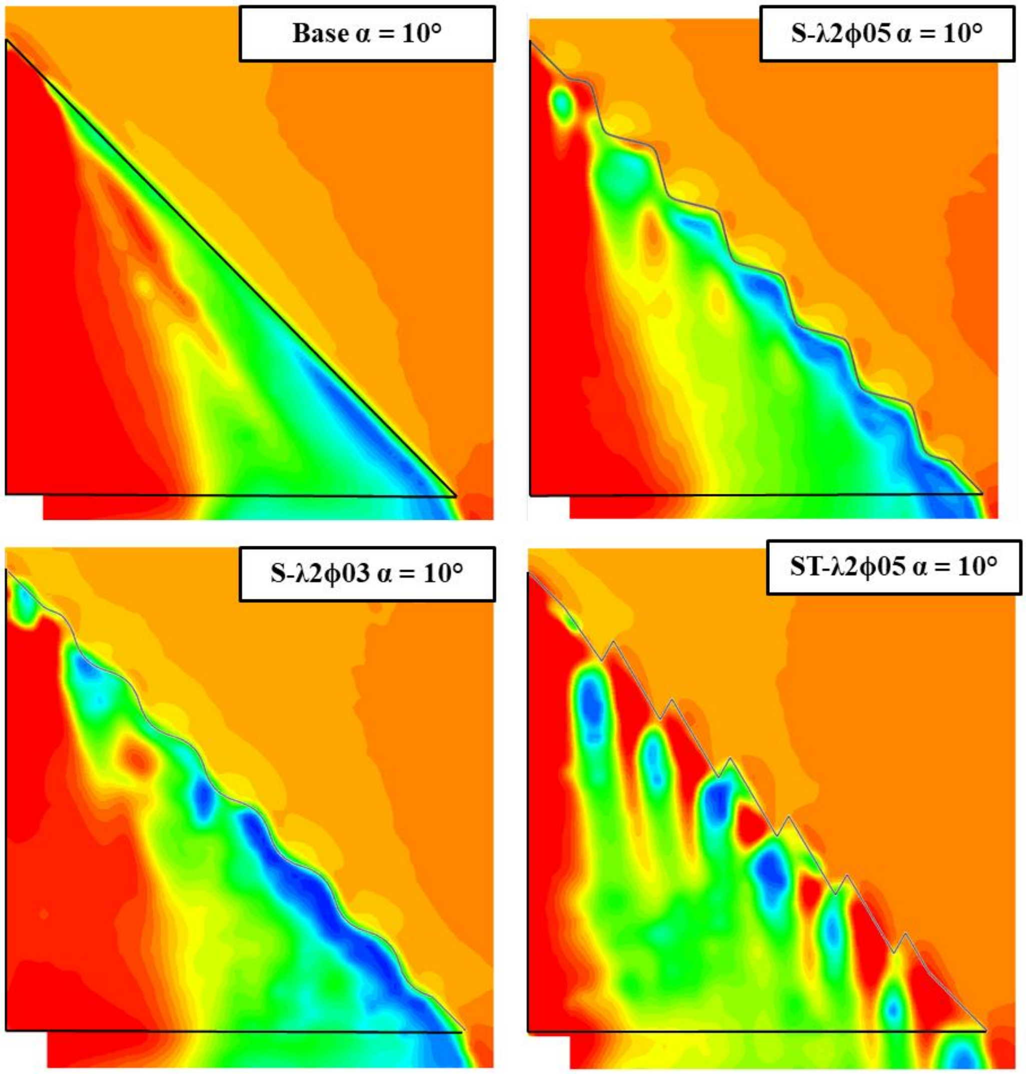

Figure F - 4 Velocity contours of base, S-λ2ϕ03, S-λ2ϕ05, and ST-λ2ϕ05 wing models at $\alpha = 10°$.

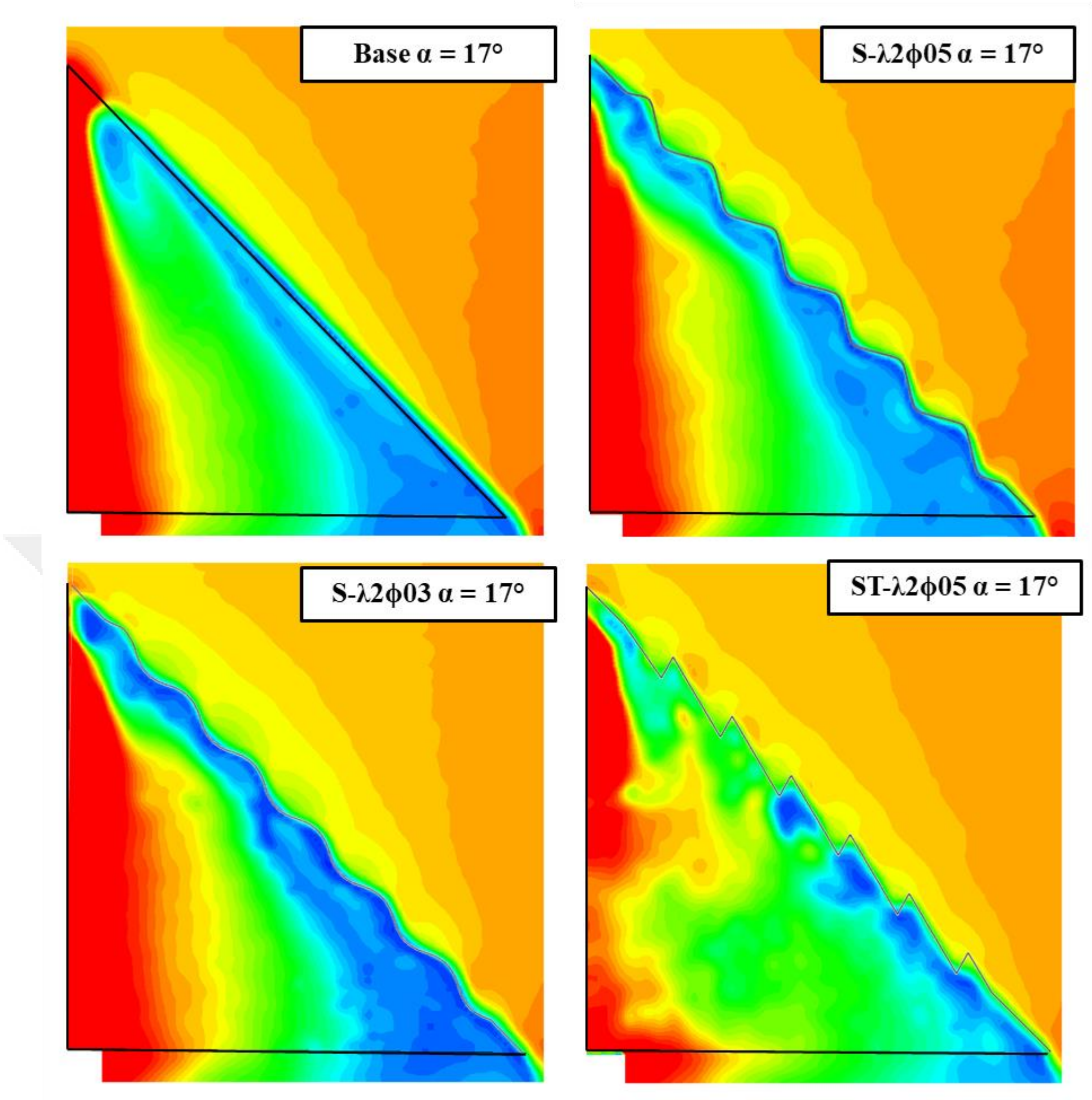

Figure F - 5 Velocity contours of base, S-λ2ϕ03, S-λ2ϕ05, and ST-λ2ϕ05 wing models at $\alpha = 17°$.

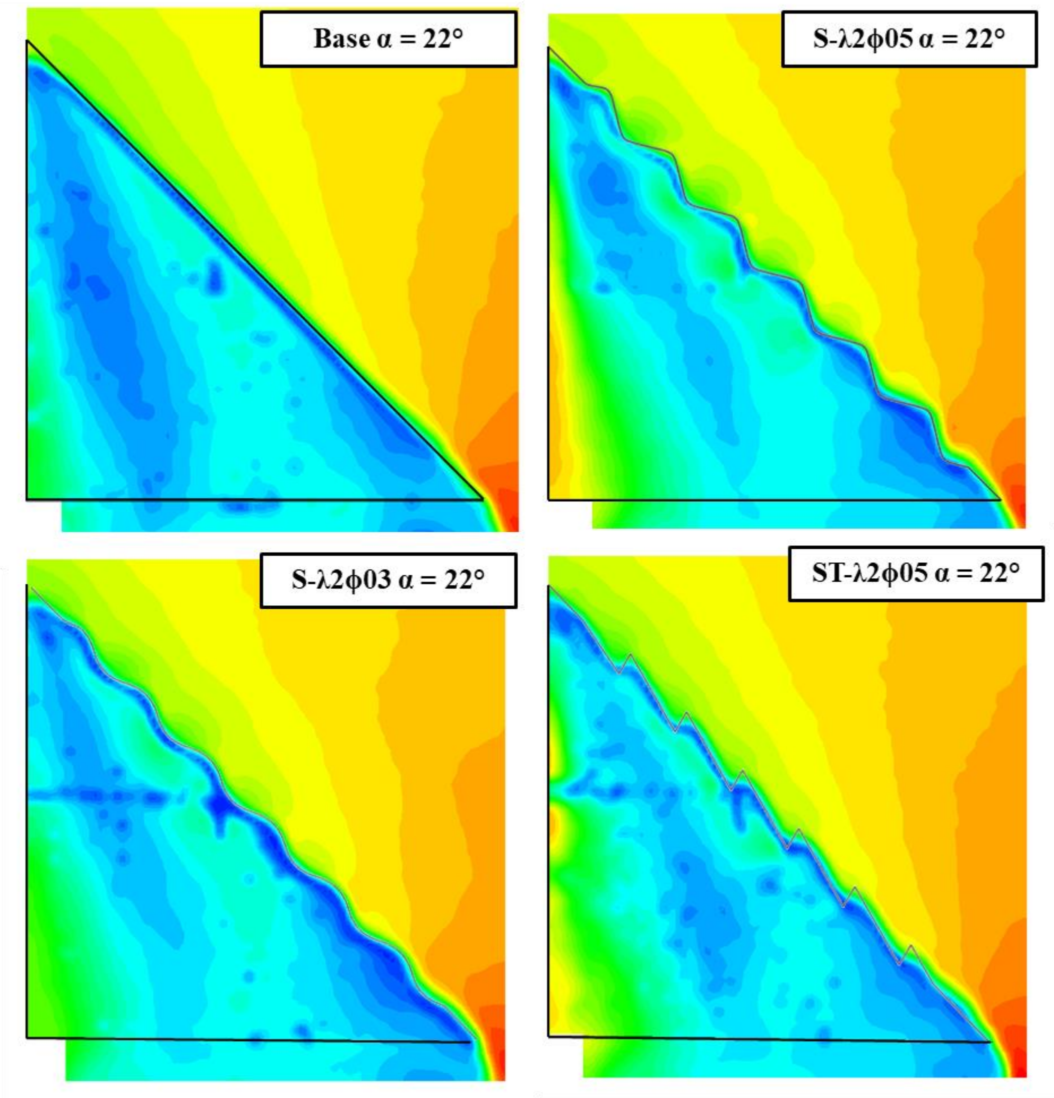

Figure F - 6 Velocity contours of base, S-λ2ϕ03, S-λ2ϕ05, and ST-λ2ϕ05 wing models at $\alpha = 22°$.